Understanding ice-sheet dynamics using geophysical observations and numerical ice-flow models

Laura Kehrl

A dissertation

submitted in partial fulfillment of the

requirements for the degree of

Doctor of Philosophy

University of Washington

2018

Reading Committee:

Ian R. Joughin, Chair

Knut Christianson

Benjamin E. Smith

Program Authorized to Offer Degree:

Earth and Space Sciences

University of Washington

Abstract

Understanding ice-sheet dynamics using geophysical observations and numerical ice-flow models

Laura Kehrl

Chair of the Supervisory Committee:
Dr. Ian R. Joughin
Applied Physics Laboratory

Mass loss from the world's ice sheets is one of the largest sources of uncertainty in sea-level rise projections for the 21st century. One way to improve sea-level rise projections is to better understand the processes driving past ice-sheet mass loss. This dissertation investigates past changes in ice flow for two regions: (1) Helheim and Kangerlussuaq Glaciers, two fast-flowing tidewater glaciers in Southeast Greenland, and (2) the Allan Hills Blue Ice Area, a slow-flowing blue ice area in East Antarctica. For both regions, I constrain changes in ice-sheet dynamics using geophysical observations and interpret those changes using numerical ice-flow models.

At Helheim and Kangerlussuaq, I examine seasonal and interannual variations in surface velocity, elevation, and terminus position from 2001 to 2016. I show that glacier dynamics depend on the extent of floating ice near the terminus. Helheim's grounded terminus calved small,

nontabular icebergs, while Kangerlussuaq's floating ice tongue calved large, tabular icebergs. Furthermore, terminus-driven, seasonal speedups and dynamic thinning were generally larger at Helheim than at Kangerlussuaq, likely due to its grounded rather than floating ice tongue. To interpret the observed changes at Helheim and Kangerlussuaq, I use inverse methods to investigate changes in basal conditions under the two glaciers. The basal shear stress under Helheim and Kangerlussuaq decreased or remained relatively constant during terminus-driven speedup events, suggesting that changes in the stress balance were generally supported outside of the region of fast flow. Finally, I use the inferred basal shear stresses to help constrain the form of the basal sliding law.

At the Allan Hills Blue Ice Area, I combine ice-penetrating radar data, an ice-flow model, and age constraints to determine a potential site to drill a million-year-old ice core. I also show that thickness anomalies in the englacial stratigraphy suggest that glacier velocity was 30% of present-day values during the last glaciation. While the dynamics of the Allan Hills Blue Ice Area are likely unimportant for sea-level rise projections, an ice core from the region could provide insight into the past stability of the Ross Sea Sector and West Antarctic Ice Sheet.

TABLE OF CONTENTS

LIST OF FIGURES

LIST OF TABLES

ACKNOWLEDGEMENTS

First and foremost, I want to thank my supervisor, Ian Joughin, for his stimulating discussions and unwavering support as I decided on a career path that is right for me. He has been an excellent role model, and I will miss our discussions about science and about life.

I also want to thank my committee members, Ben Smith, Knut Christianson, Michelle Koutnik, and Cecilia Bitz, for their support over the years. I appreciate that their doors have always been open and that they have always been willing to lend a hand when needed.

The glaciology community at the University of Washington has been like a family over the last five years. Twit Conway, while not on my committee, served as the mentor for my chapter on the Allan Hills Blue Ice Area. He pushed me to ask difficult questions and supported me when I didn't know the answers. Nick Holschuh and Daniel Shapero also provided inspiration for the ideas in this dissertation. My officemates, David Lilien, David Shean, Max Stevens, Taryn Black, and Kristin Poinar, always managed to put a smile on my face. Bob Hawley and Huw Horgan, while not at the University of Washington, helped me survive my undergraduate and master's degrees to reach this point. They have been wonderful mentors and friends over the years, and I appreciate their continued support and wittiness.

Lastly, I want to thank my family and friends for reminding me that there is life outside of my dissertation. My grandparents, Gagi and Grandpa Bud, have always supported me, no matter what I wanted to do. My brother, Ryan, has spent countless hours on the phone with me. Most importantly, I want to thank my husband, Mike, and cuddle monster, Zoey, for their unconditional love and support.

DEDICATION

To my grandparents,

Gagi and Grandpa Bud,

who supported me every step of the way.

Chapter 1. Introduction

1.1 Motivation

Over the next century, sea-level rise will likely displace people from their homes and increase the incidence of storm-related flooding [*IPCC*, 2014a]. To mitigate these effects, it is important that we accurately predict future sea-level rise. One of the greatest sources of uncertainty in sea-level rise projections is the contribution from the world's ice sheets. The ice sheets currently account for one-fifth of total sea-level rise, but their contributions are expected to rise over the coming century [*IPCC*, 2014b].

The ice sheets lose mass through changes in ice discharge, surface mass balance, and basal mass balance. Variations in ice discharge are driven by changes in ice-sheet dynamics. In Antarctica, satellite measurements, numerical models, and in situ measurements show increased ice discharge from the ice streams draining the continent, likely caused by a loss of ice shelf buttressing due to enhanced basal melt [*Pritchard et al.*, 2012]. In Greenland, many tidewater glaciers have retreated, sped up, and thinned in the last two decades, also likely as a result of changes in the ocean [*Rignot and Kanagaratnam*, 2006; *Moon and Joughin*, 2008; *Moon et al.*, 2012]. Yet, many of the processes driving these rapid changes remain poorly understood [*IPCC*, 2014b], making it difficult to predict ice-sheet mass loss over the next century.

One way to improve projections of ice-sheet mass loss is to better understand the processes driving recent changes in the ice sheets. Satellites started collecting measurements over the ice sheets in the 1970s, and the temporal and spatial resolution of these measurements has only improved since then. These measurements provide a window into the recent past and an opportunity to understand changes in ice-sheet dynamics on seasonal, interannual, and decadal timescales. These measurements provide the foundation for two of the chapters in this dissertation.

Another way to improve predictions is to better understand the link between the climate and ice-sheet dynamics in the distant past. By analyzing the behavior of the ice sheets in the past, we may develop a better understanding of what might happen in the future. For example, marine and geologic evidence suggests that the West Antarctic Ice Sheet may have collapsed during the previous interglacial (Marine Isotope Stage 5e) when the sea level was 6 to 9 m higher than it is today [*Alley et al.*, 2015; *Dutton et al.*, 2015]. No direct measurements of climate and ice flow exist for this period or other past periods, and so we instead turn to geophysical measurements and ice cores for these analyses. These ideas provide the foundation for my remaining chapter.

1.2 Research approach and tools

In this dissertation, I combine geophysical observations and numerical ice-flow models to understand recent and past changes in ice-sheet dynamics. The geophysical observations constrain the changes in ice flow and thickness, and the numerical models assist the interpretation of those changes in terms of physical processes. For changes in ice-sheet dynamics that occurred during the satellite era, I rely on satellite measurements. For changes in ice-sheet dynamics that occurred long before the satellite era, I turn to ice-penetrating radar to map the englacial stratigraphy and then interpret the stratigraphy in terms of the ice-flow dynamics that must have caused it.

1.3 Organization of the dissertation

This thesis is organized into five chapters, beginning with this introduction and ending with a summary and suggestions for future work. The middle three chapters are scientific papers.

Chapter 2 is a manuscript entitled "**Seasonal and interannual variabilities in terminus position, glacier velocity, and surface elevation at Helheim and Kangerlussuaq Glaciers from 2008 to 2016**," which was published in *Journal of Geophysical Research: Earth Surface* [*Kehrl et* *al.*, 2017]. This paper developed a detailed timeseries of terminus position, glacier surface velocity, surface elevation, and iceberg-calving behavior to investigate geometric and environmental controls on the seasonal and interannual evolution of Helheim and Kangerlussuaq Glaciers, two of Greenland's largest tidewater glaciers. The supplement for this paper can be found in Appendix A.

Chapter 3 is a manuscript entitled "**Basal conditions for Helheim and Kangerlussuaq Glaciers, Southeast Greenland, from 2001 to 2016**," which will be submitted to *The Cryosphere* in October 2018. This manuscript used the timeseries developed in Chapter 2, combined with measurements from other studies [*Howat et al.*, 2005, 2007; *Howat*, 2017], to run more than 20 basal inversions to characterize seasonal and interannual variations in basal conditions at Helheim and Kangerlussuaq. The supplement for this paper can be found in Appendix B.

Chapter 4 is a manuscript entitled "**Evaluating the duration and continuity of potential climate records from the Allan Hills Blue Ice Area, East Antarctica**," which was published in *Geophysical Research Letters* [*Kehrl et al.*, 2018]. This paper combined an ice-flow model, ice-penetrating radar data, and existing ages constraints to determine a potential site for a continuous, million-year-old ice core in the Allan Hills. The supplement for this paper can be found in Appendix C.

Chapter 2. Seasonal and interannual variabilities in terminus position, glacier velocity, and surface elevation at Helheim and Kangerlussuaq Glaciers from 2008 to 2016

Chapter 2, in full, is a reprint of "Seasonal and interannual variabilities in terminus position, glacier velocity, and surface elevation at Helheim and Kangerlussuaq Glaciers from 2008 to 2016" authored by L. M. Kehrl, I. Joughin, D. E. Shean, D. Floricioiu, and L. Krieger as it appears in *Journal of Geophysical Research: Earth Surface* 2017. The supplement for this paper can be found in Appendix A. The dissertation author was the primary investigator and author of this paper.

2.1 Abstract

The dynamic response of Greenland tidewater glaciers to oceanic and atmospheric change has varied both spatially and temporally. While some of this variability is likely related to regional climate signals, glacier geometry also appears to be important. In this study, we investigated the environmental and geometric controls on the seasonal and interannual evolution of Helheim and Kangerlussuaq Glaciers, Southeast Greenland, from 2008 to 2016, by combining year-round, satellite measurements of terminus position, glacier velocity, and surface elevation. While Helheim remained relatively stable with a lightly grounded terminus over this time period, Kangerlussuaq continued to lose mass as its grounding line retreated into deeper water. By summer 2011, Kangerlussuaq's grounding line had retreated into shallower water, and the glacier had a ~5-km-long floating ice tongue. We also observed seasonal variations in surface velocity and elevation at both glaciers. At Helheim, seasonal speedups and dynamic thinning occurred in the late summer when the terminus was most retreated. At Kangerlussuaq, we observed summer speedups due to surface-melt-induced basal lubrication and winter speedups due to ice-shelf retreat. We suggest that Helheim and Kangerlussuaq behaved differently on a seasonal timescale

due to differences in the spatial extent of floating ice near their termini, which affected iceberg-calving behavior. Given that seasonal speedups and dynamic thinning can alter this spatial extent, these variations may be important for understanding the long-term evolution of these and other Greenland tidewater glaciers.

2.2 Introduction

The contribution of the Greenland Ice Sheet to sea-level rise more than quadrupled from 1991–2001 to 2002–2011 [*Shepherd et al.*, 2012] as a result of enhanced surface melt and increased ice discharge from tidewater glaciers [*Enderlin et al.*, 2014; *Van Den Broeke et al.*, 2016]. While this widespread increase in ice discharge has been attributed, likely correctly, to ocean warming [*Holland et al.*, 2008; *Hanna et al.*, 2009; *Murray et al.*, 2010; *Straneo et al.*, 2010], there has been significant spatial variability in the dynamic response of individual glaciers [*Moon et al.*, 2012]. Tidewater glaciers in the same fjord, which are likely subject to similar oceanic and atmospheric conditions, have behaved differently [*Rignot et al.*, 2016; *Motyka et al.*, 2017], indicating that individual glacier characteristics, such as glacier geometry, likely play an important role in modulating a glacier's dynamic response [*Enderlin et al.*, 2013; *Amundson*, 2016; *Felikson et al.*, 2017].

The dynamics of tidewater glaciers are sensitive to changes near the terminus [*Nick et al.*, 2009]. Many Greenland tidewater glaciers have a grounded or nearly grounded terminus, and consequently the terminus position often closely corresponds with the grounding-line position (location where the ice transitions from grounded to floating). Several processes have been proposed to link terminus retreat to oceanic and atmospheric changes, including enhanced submarine melt [*Holland et al.*, 2008; *Motyka et al.*, 2011], ice-mélange weakening [*Joughin et al.*, 2008a; *Amundson et al.*, 2010], and increased hydrofracture of water-filled crevasses [*Benn et* *al.*, 2007]. Once retreat is initiated, the glacier's geometry will affect its dynamic response. Retreat into deeper water can promote speedup, thinning, and further retreat, whereas retreat into shallower water can cause the glacier to slow and to perhaps stabilize [*Meier and Post*, 1987; *Schoof*, 2007]. Furthermore, lateral constrictions in glacier width can help stabilize the terminus at a particular location [*Gudmundsson et al.*, 2012]. As a result of these dynamic feedbacks, it can be difficult to attribute a change in glacier dynamics to a specific oceanic or atmospheric forcing.

To address this difficulty, several studies have turned to seasonal records of terminus position [*Howat et al.*, 2010; *Seale et al.*, 2011; *Schild and Hamilton*, 2013] and glacier velocity [*Moon et al.*, 2014, 2015]. By comparing these records to different climatic variables over many years, these studies have attempted to correlate seasonal changes in terminus position and/or glacier velocity to oceanic and atmospheric changes. However, often there is no clear relationship between glacier dynamics and environmental change: the timing of the seasonal onset of retreat and speedup varies spatially from glacier to glacier and temporally from year to year at individual glaciers [*Schild and Hamilton*, 2013; *Moon et al.*, 2014]. Seasonal and multiyear variations in glacier geometry (ice thickness, surface slope, and grounding-line position) have been put forward as a possible mechanism to help explain this temporal variability at individual glaciers [e.g., *Schild and Hamilton*, 2013], but until recently we have lacked the necessary seasonal surface-elevation records to explore this hypothesis further.

In this study, we combined year-round records of terminus position, glacier velocity, and surface elevation from 2008 to 2016 to investigate seasonal and multiyear changes in glacier geometry at Helheim and Kangerlussuaq Glaciers (Figure 2.1 and Figure 2.2), the two largest tidewater glaciers in Southeast Greenland. Helheim and Kangerlussuaq collectively drain ~8% of the Greenland Ice Sheet area [*Nick et al.*, 2013]. Both glaciers rapidly retreated, accelerated, and thinned in the early 2000s [*Rignot et al.*, 2004; *Howat et al.*, 2005, 2007; *Stearns and Hamilton*, 2007]. The resulting dynamic mass loss from these two glaciers alone accounted for roughly 30% of the 2000-2012 dynamic mass loss from the entire Greenland Ice Sheet [*Enderlin et al.*, 2014]. After their retreats ended in 2006, both glaciers slowed, but Helheim stopped thinning while Kangerlussuaq continued thinning [*Howat et al.*, 2011; *Bevan et al.*, 2012]. The glaciers have also behaved differently on a seasonal timescale; terminus positions typically varied seasonally at Kangerlussuaq but showed little seasonality at Helheim [*Joughin et al.*, 2008b; *Schild and Hamilton*, 2013]. By comparing the varying evolution of Helheim and Kangerlussuaq over seasonal and multiyear timescales, we develop new insights into how differences in glacier geometry affect a glacier's dynamic response to oceanic and atmospheric changes. In particular, we focus our analysis on changes in the spatial extent of floating ice near the terminus, which can affect iceberg-calving behavior [*Benn et al.*, 2007].

2.3 Methods

We combined several different data sets to develop seasonal records of glacier velocity, terminus position, iceberg-calving behavior, surface elevation, and surface-elevation change rates at Helheim and Kangerlussuaq from 2008 to 2016. To interpret these observations, we also considered bed elevations, ice-mélange conditions, sea-ice fraction (SIF), and modeled glacier surface runoff in our analysis.

2.3.1 Glacier velocity

To measure glacier velocity, we applied speckle tracking techniques [*Joughin*, 2002; *Joughin et al.*, 2010] to pairs of synthetic aperture radar (SAR) images from the German Aerospace Center's (DLR) TerraSAR-X (TSX) mission [*Krieger et al.*, 2013]. This satellite started acquiring data over Helheim and Kangerlussuaq in September 2008. A second, virtually identical satellite, TDX, was launched in June 2010 to complete the tandem configuration of the TanDEM-X (TDM) mission. The repeat period of each satellite allows velocity estimates to be determined over intervals as short as 11 days. Due to missed acquisitions, some velocity estimates were computed using 22- or 33-day intervals. We did not attempt estimates for intervals longer than 33 days, leaving some gaps in our record. All velocity estimates were smoothed with a moving average filter to a spatial resolution of ~300 m. Conversion from the radar line-of-sight to the horizontal across-track direction under a surface-parallel flow assumption can yield slope-dependent errors of up to 3% [*Joughin et al.*, 2010a]. For observations collected along the same satellite track, this is a systematic error common to all estimates, so the error does not apply to changes in velocity. Of our 264 velocity products, 237 (90%) were collected along the same track for each glacier.

2.3.2 Terminus position

We measured terminus position by digitizing the location where the calving front intersects the longitudinal profiles shown in Figure 2.1a and Figure 2.2a. We chose this method over the box method [*Moon and Joughin*, 2008] because it allowed us to include satellite images with high cloud cover and Landsat 7 images with gaps due to the scan line corrector (SLC) failure, which improved the temporal resolution of our records. Terminus positions were digitized in all available TSX/TDX radar images and Worldview-1/2/3 (WV) and Landsat 7/8 panchromatic scenes. We report terminus position relative to the 2008-2016 average, with a negative (positive) value indicating a more retreated (advanced) terminus position than average.

To assess uncertainties in the measured terminus positions, we compared digitized terminus positions from satellite images that were acquired on the same day when no large calving events occurred between the acquisitions. Consequently, the uncertainty estimates account for errors due to manual digitization and errors introduced by including satellite images with different spatial resolution, acquisition geometry, and spectral characteristics. The 22 pairs of coincident, digitized terminus positions differed by 2-42 m, with a root-mean-squared (RMS) difference of 24 m.

2.3.3 *Iceberg-calving behavior*

We used the available satellite images to assess the calved iceberg type. Two types of icebergs have been observed previously at Helheim and Kangerlussuaq: tabular and non-tabular [*Joughin et al.*, 2008b]. Tabular icebergs have a large longitudinal width-to-height ratio and do not capsize when they calve. These icebergs can be distinguished in the satellite images by the presence of crevasses on their surfaces (Figure A.1a). Non-tabular icebergs capsize when they calve due to their smaller width-to-height ratio and greater buoyancy-driven torque (Figure A.1b) [*Amundson et al.*, 2010; *James et al.*, 2014]. We compared subsequent satellite images to determine the type of new icebergs in the fjord after each iceberg-calving episode. We refer to periods of iceberg calving as “episodes” rather than as “events” because we cannot determine if the icebergs calved during a single event or during a series of events that occurred over several days.

Iceberg-calving episodes were divided into three types: (1) tabular, (2) non-tabular, and (3) mixed (both tabular and non-tabular). We considered an episode to be “tabular” if new tabular icebergs appeared in the fjord that could account for the observed retreat between subsequent satellites images. If new tabular icebergs appeared but could not account for all of the observed retreat, then the episode was considered “mixed.” All other episodes were considered “non-tabular.” This approach may incorrectly characterize some tabular or mixed iceberg-calving episodes as non-tabular if the tabular icebergs broke up and overturned between subsequent satellite images. However, the observed tabular icebergs typically remained intact for several weeks, suggesting that we observed a substantial fraction of tabular icebergs before they broke up.

2.3.4 *Glacier surface elevation*

We combined point surface-elevation measurements from NASA's Airborne Topographic Mapper [ATM; *Krabill et al.*, 2014] with digital elevation models (DEM) from WV, GeoEye-1, SPIRIT [*Korona et al.*, 2009], and TanDEM-X (TDM). DEMs from WV and GeoEye-1 were created following the stereo-photogrammetry techniques outlined in *Shean et al.* [2016]. TDM DEMs were processed from bistatic SAR acquisitions using the Integrated TanDEM-X Processor [ITP; *Rossi et al.*, 2012]. Large absolute elevation offsets in the resulting TDM DEMs are caused by baseline-dependent interferometric SAR (InSAR) height ambiguities and were corrected by adjusting the absolute phase offset during InSAR processing.

To reduce georeferencing errors, all DEMs were co-registered to ground control points (GCPs) over exposed rock. We adjusted the DEMs using a rigid-body translation that minimized the elevation difference between the DEMs and the GCPs [*Shean et al.*, 2016]. All available ICESat-1 data [*Zwally et al.*, 2003], LVIS data [*Blair and Hofton*, 2010], and ATM data over exposed bedrock surfaces were included as GCPs. After co-registration, the uncertainty of each DEM was estimated using the normalized median absolute deviation [NMAD; *Höhle and Höhle*, 2009] of all GCP-DEM differences [*Shean et al.*, 2016]. The average NMAD for the WV and TDM DEMs was 1.18 m and 1.77 m, respectively.

2.3.5 Bed elevation and flotation condition

While several gridded bed-elevation products exist for Helheim and Kangerlussuaq [e.g., *Bamber and Griggs*, 2013; *Morlighem et al.*, 2014], there are large discrepancies among these products due to different interpolation methods. Consequently, to avoid errors introduced by interpolation, we used bed-elevation point measurements from the Helheim and Kangerlussuaq 2006-2014 Composite V3 products from the Center for Remote Sensing of Ice Sheets (CReSIS). We also included the CReSIS radar transect from 21 May 2001 in our analysis for Helheim.

Some of the radar thicknesses in the Composite V3 products were collected over floating ice. To determine if a radar thickness was collected over floating ice, we used the ATM surface-elevation measurements that were collected concurrently with the radar-thickness measurements. If the measured surface elevation was less than or equal to the flotation height for a given radar thickness (assuming an ice density of 917 kg m^{-3} and seawater density of 1025 kg m^{-3}), then we considered the ice at that location to be floating and removed that measurement from our analysis of bed elevations. Almost all radar thicknesses acquired over the lower 5 km of Kangerlussuaq were collected over floating ice (Figure 2.2c). After removing these points, the RMS for the bed-elevation crossover differences in regions below sea level improved from 113 m to 45 m for Helheim and from 90 m to 44 m for Kangerlussuaq. Given that crossover differences were <50 m for 80% of the crossovers, we assumed a bed-elevation uncertainty of 50 m.

We used the bed-elevation measurements, along with the available surface-elevation measurements, to calculate the spatial extent of floating and grounded ice for each glacier. In particular, we focused our analysis on determining regions where the ice remained "grounded" or "floating" or switched between grounded and floating ("changing") from 2011 to 2015. We characterized a point as "grounded" ("floating") if its surface elevation remained more than 5 m above (below) the flotation threshold from 2011 to 2015. The 5-m cutoff accounts for bed-elevation uncertainties of 50 m and surface-elevation variations due to tides [*Voytenko et al.*, 2015]. All other points are characterized as likely "changing" between grounded and floating.

(Note that the large-scale spatial patterns discussed in the text are unaffected by changing this 5-m cutoff within a reasonable range of 0-10 m.)

2.3.6 *Surface-elevation change rate*

To better understand the observed variations in glacier surface elevation, we calculated the average rate of elevation change for the hatched regions in Figure 2.1a and Figure 2.2a using two different methods: (1) we differenced all pairs of DEMs with time intervals of less than four months and (2) we used the surface velocity and elevation measurements to estimate the ice flux in and out of the region. We refer to these methods as the "DEM" and "flux-gate" methods, respectively. While the DEM method provides more accurate estimates of the surface-elevation change rate, the flux-gate method increases the temporal resolution of our records from every few months (when we have DEMs) to every few weeks (when we have surface velocities) and also provides insight into the causes of the observed elevation changes. In the flux-gate method, we assumed that the rate of surface-elevation change (*dh/dt)* averaged over the region equaled the rate of ice-thickness change (*dH/dt*), which we calculated as

$$\frac{dh}{dt} = \frac{dH}{dt} = \frac{1}{A}\left[\int_0^{W_i} u_i(x,t)H_i(x,t)dx - \int_0^{W_o} u_o(x,t)H_o(x,t)dx\right] + \dot{a}, \qquad (2.1)$$

where *A* is the area of the region, *t* is time, *x* is the coordinate parallel to the inflow or outflow boundary, *H(x,t)* is the ice thickness at the boundary, *u(x,t)* is the glacier velocity normal to the boundary, *W* is the glacier width at the boundary, and $\dot{a}$ is the elevation change rate due to surface mass balance (assuming basal melt is negligible). The subscripts signify values at the inflow (*i*) and outflow (*o)* boundaries. We calculated *dh/dt* for all time periods with surface-velocity measurements and linearly interpolated the surface-elevation measurements to match those time periods. To estimate $\dot{a}$, we used surface mass balance from the nearest grid cell in the 11-km resolution Regional Atmospheric Climate Model [RACMO2.3; *van Angelen et al.*, 2013; *Noël et* *al.*, 2015] and assumed a constant density (900 kg m^{-3}) to convert surface mass balance to an elevation change rate.

Several key assumptions and measurement errors contributed to uncertainties in the inferred *dh/dt* from the flux-gate method. First, we assumed that the depth-averaged velocity was equal to the measured surface velocity (Equation 2.1). Although this is only an approximation, basal sliding accounts for >90% of the surface velocity under the main trunk of Helheim and Kangerlussuaq [*Shapero et al.*, 2016], so the depth-averaged velocity should be within ~2% of the surface velocity [*Cuffey and Paterson*, 2010]. This approximation contributed to uncertainties in *dh/dt* of <1 cm d^{-1}. Second, we assumed that basal melt is negligible. While there are currently no direct measurements of basal melt beneath the grounded portions of these or other tidewater glaciers, the melt rate should be <3 cm d^{-1} based on theoretical calculations (Text A.1) [*Cuffey and Paterson*, 2010]. Third, bed-elevation errors of 50 m could introduce systematic errors in *dh/dt* of >30 cm d^{-1}. To mitigate this error, we positioned the boundaries of the hatched regions in Figure 2.1a and Figure 2.2a along CreSIS radar transects that had distinct bed returns and low bed-elevation crossover differences. Fourth, the RACMO surface mass balance product likely introduced additional uncertainties [*Noël et al.*, 2016]; however, these uncertainties are difficult to quantify given the limited surface-mass-balance measurements collected over Helheim and Kangerlussuaq [*Andersen et al.*, 2010]. Finally, errors in the surface elevation and velocity measurements introduced random errors in *dh/dt* of ~3 cm d^{-1}.

To determine an error estimate that incorporated all of the above sources of uncertainty, we compared the surface-elevation change rates from the flux-gate and DEM methods. Although the surface-elevation change rates calculated using the two methods are not directly comparable due to differences in temporal resolution, comparing the two methods does provide an upper bound on the uncertainty in the rates inferred from the flux-gate method. The RMS difference between *dh/dt* calculated using the two methods was 3 cm d^{-1} for Helheim and 5 cm d^{-1} for Kangerlussuaq (Text A.2 and Figures A.2-A.4).

2.3.7 Glacier surface runoff, ice-mélange rigidity, and sea-ice fraction

While many different oceanic and atmospheric changes can affect tidewater glacier dynamics, in this study we focused primarily on the effects of surface melt and ice-mélange rigidity. To quantify surface melt, we used daily, modeled surface runoff from RACMO2.3. We sampled surface runoff at the same grid cells that we used for our surface-elevation change rate calculations (Section 2.3.6). The magnitude of the surface runoff estimates are sensitive to RACMO's spatial resolution [*Noël et al.*, 2016], so we primarily used these estimates to define the surface melt season.

To assess ice-mélange rigidity, we used the TSX velocity estimates from speckle tracking. If speckle tracking can determine a velocity in the ice mélange, then the ice mélange is likely rigid or nearly rigid; if speckle tracking cannot determine a velocity, then the ice mélange is free to move around [*Joughin et al.*, 2008a]. We characterized the ice mélange as "rigid" or "free" based on these criteria. Since rigid mélange is often linked to sea-ice formation [*Amundson et al.*, 2010], we also reported sea-ice fraction (SIF) from the Operational Sea Surface Temperature and Sea Ice Analysis (OSTIA) system, which estimates daily SIF at 10 km resolution by combining in situ measurements with satellite data from the Group for High Resolution Sea Surface Temperature [*Donlon et al.*, 2012]. The SIF estimates have a threshold accuracy of ~20%. We sampled SIF at grid cells near the entrance to Sermilik (Helheim) and Kangerlussuaq Fjords.

2.4 Results

Using the methods outlined above, we produced a detailed record of terminus position, glacier velocity, surface elevation, and iceberg-calving behavior at Helheim and Kangerlussuaq from 2008 to 2016. Our observations indicate that Helheim and Kangerlussuaq behaved differently on a seasonal and interannal timescale.

2.4.1 Helheim Glacier

Figure 2.3 shows terminus position, iceberg-calving behavior, glacier velocity, surface elevation, surface-elevation change rate, ice-mélange rigidity, sea-ice fraction, and surface runoff at Helheim from 2008 to 2016. Helheim's mean terminus position from 2008 to 2016 was 4.5 km upstream of its May 2001 position (Figure 2.1b). The glacier retreated by 100 ± 20 m per year from 2008 to 2016 (p-value of 10^{-6} from the linear regression), with seasonal variations in terminus position superimposed on this long-term trend. The glacier reached its position of maximum seasonal retreat in late summer during seven out of the eight years and its position of maximum advance in late winter during at least five of those years. Non-tabular iceberg calving accounted for 105 (86%) of the 122 observed calving episodes at Helheim (Figure 2.3a). Glacier velocity varied seasonally during some years by up to 3 km yr^{-1}, with peak velocities occurring in late summer (Figure 2.3b). Surface elevations varied seasonally by ~10-20 m at H02 and H05 (Figure 2.3c), with glacier thickening rates peaking in January to March and glacier thinning rates peaking in August to September (Figure 2.3d).

The two largest seasonal changes in terminus position occurred in 2010/11 and 2013/14, when Helheim retreated and advanced over a range of >3 km. In 2010, Helheim retreated 2.3 km down a reverse bed slope from early July to mid-September. During the retreat, the glacier sped up by 1.6 km yr^{-1} (24%) at H05 and by 0.4 km yr^{-1} (8%) at H20, reaching a peak velocity in

September at H05 and in late November at H20. Helheim then slowed as its terminus readvanced 3.5 km to the crest of the reverse bed slope by mid-March 2011 (Figure 2.1c). Similarly, in 2013, Helheim retreated 2.8 km down the reverse bed slope from early March to mid-August, with a subsequent readvance of 3.6 km to the top of the reverse bed slope by mid-February 2014. During this 2013 retreat, the glacier sped up by 1.9 km yr^{-1} (32%) at H05 and by 0.3 km yr^{-1} (6%) at H20, again reaching a maximum velocity in September at H05 and in late November at H20. Helheim also thinned by ~20 m at H02 and H05 during this retreat. At H02, the glacier thinned to flotation and a floating ice tongue formed downstream. Although the available surface-elevation measurements do not cover winter 2010/11, surface elevations collected before and after the winter indicate that Helheim may have thinned to flotation at H02 during the 2010 retreat as well. Furthermore, glacier thinning rates exceeded 15 cm d^{-1} during summers 2010, 2013, and 2015, but were closer to 5 to 10 cm d^{-1} during summers 2011, 2012, and 2014. Modeled thinning rates from surface mass balance processes were <5 cm d^{-1} during all summers, indicating that the observed thinning occurred primarily due to a change in ice dynamics [*Bevan et al.*, 2015]. Helheim calved non-tabular icebergs during the 2010 and 2013 seasonal retreats. The seasonal advances ended when the terminus reached the top of the reverse bed slope from where it calved several large tabular icebergs. The ice mélange was generally less rigid during years when large seasonal retreats and advances occurred, as shown in Figure 2.4.

Figure 2.5 shows the range of observed glacier velocities and surface elevations at Helheim from 2011 to 2015. We removed all linear trends before calculating the range for each grid cell. The largest variations in glacier velocity and surface elevation occurred within ~10 km of the calving front. Figure 2.5d shows how the surface-elevation variations affected the flotation condition at each CReSIS bed-elevation measurement (Section 2.3.5). For a large region downstream of H05, the glacier changed between floating and grounded from 2011 to 2015. For regions upstream of H05, the glacier remained grounded. When the glacier advanced to the top of the reverse bed slope at +2 km (Figure 2.1c), its terminus was always floating.

2.4.2 Kangerlussuaq Glacier

Figure 2.6 shows terminus position, iceberg-calving behavior, glacier velocity, surface elevation, surface-elevation change rate, ice-mélange rigidity, sea-ice fraction, and surface runoff at Kangerlussuaq from 2008 to 2016. Kangerlussuaq's mean terminus position from 2008 to 2016 was 4.0 km upstream of its May 2001 position (Figure 2.2b). The glacier advanced by 200 ± 30 m yr^{-1} from 2008 to 2016 (p-value of 10^{-8} from the linear regression), with seasonal variations in terminus position of >3 km superimposed on this long-term trend during six out of the eight years. The two years without a pronounced seasonal cycle in terminus position were 2010 and 2011.

Typically, Kangerlussuaq advanced from December to late June or mid-July and then retreated until December (Figure 2.6a). Few icebergs calved during the seasonal advance. The late-summer retreat started with the calving of large tabular icebergs, which transitioned to mixed and non-tabular icebergs as the retreat continued. Non-tabular iceberg calving accounted for 36 (47%) of the 77 observed calving episodes at Kangerlussuaq. Figure 2.7 compares the timing of seasonal changes in terminus position to changes in ice-mélange rigidity and sea-ice fraction. The timing of the seasonal transition from retreat to advance corresponded well with the seasonal transition to more rigid mélange and denser sea-ice conditions.

Kangerlussuaq's velocity varied on both a seasonal and interannual timescale (Figure 2.6b). Glacier velocity typically increased from late summer to mid-winter and then decreased again until late summer at all sample points. This "winter speedup" was most pronounced during winter 2010/11, when the glacier sped up by 2.1 km yr^{-1} (25%) at K05 and by 0.5 km yr^{-1} (16%)

at K20. The winter speedup then decreased in magnitude from 2011 to 2015. The glacier also slowed over this time period, with glacier velocity decreasing by 400 m yr^{-2} at K05 and by 70 m yr^{-2} at K20, as shown in Figure 2.8a. By 2015, Kangerlussuaq's velocity was similar to its velocity before the 2010/11-winter speedup event. Kangerlussuaq also sped up by ~200-400 m yr^{-1} (~5-10%) at all sample points during the mid summer.

Kangerlussuaq continued to thin through 2015, with thinning rates generally decreasing from 2001 to 2015 (Figure 2.2b and Figure 2.6c) [*Howat et al.*, 2011]. By late summer 2011, the glacier had thinned to flotation at K05, with surface elevations remaining at or below the flotation threshold through 2015. The greatest thinning rates (6 ± 1 to 12 ± 1 m yr^{-1}) from 2011 to 2015 occurred near K20, as shown in Figure 2.8b. Seasonal variations in surface elevation of ~20 m at K05 and ~10 m at K10 were superimposed on the long-term thinning. Seasonal thinning generally started in May or June, reached a maximum rate of 10-15 cm d^{-1} in July or August, and ended by September to November (Figure 2.6d). Glacier thickening typically peaked in March. Thinning rates from surface mass balance processes were <5 cm d^{-1} during all summers, indicating that the observed thinning occurred primarily due to a change in ice dynamics.

Figure 2.9 shows the range of observed glacier velocities and surface elevations at Kangerlussuaq from 2011 to 2015. All linear trends (Figure 2.8) were removed before calculating the range for each grid cell. The largest variations in glacier velocity and surface elevation occurred near the terminus. Figure 2.9d shows how the surface-elevation variations affected the flotation condition at each CReSIS bed-elevation measurement. (Note that while we removed many of the bed-elevation measurements that were collected over Kangerlussuaq's floating ice tongue, that the remaining measurements might still have large uncertainties.) The region downstream of K05 changed between grounded and floating from 2011 to 2015, while the region upstream of K05 remained grounded.

2.5 Discussion

Despite extensive dynamic mass loss from many Greenland tidewater glaciers over the last two decades, there has also been significant spatial and temporal variability in the dynamic response of individual glaciers [*Moon and Joughin*, 2008; *Moon et al.*, 2012; *Enderlin et al.*, 2014]. Regional climatic and oceanographic differences likely account for some of this spatiotemporal variability [*Inall et al.*, 2014; *Jensen et al.*, 2016]. In addition, individual glacier characteristics, such as glacier geometry, have also likely contributed [*Enderlin et al.*, 2013; *Felikson et al.*, 2017]. In the next sections, we discuss the interplay between glacier geometry and environmental change in determining the multiyear evolution, seasonal dynamics, and terminus behavior of Helheim and Kangerlussuaq Glaciers from 2008 to 2016.

2.5.1 *Long-term behavior from 2008 to 2016*

Many Greenland tidewater glaciers, including Helheim and Kangerlussuaq, rapidly retreated and accelerated during a period of above-average oceanic and atmospheric temperatures in the early 2000s [*Joughin et al.*, 2004b; *Rignot et al.*, 2004; *Howat et al.*, 2007, 2008; *Hanna et al.*, 2009; *Murray et al.*, 2010]. While some glaciers, such as Greenland's largest glacier, Jakobshavn Isbrae, have continued to retreat and thin [*Joughin et al.*, 2004b, 2012], other glaciers have returned to more stable terminus positions. Helheim and Kangerlussuaq ended their terminus retreats by 2006 [*Joughin et al.*, 2008b; *Bevan et al.*, 2012], but Helheim stopped thinning shortly thereafter (Figure 2.3c) [*Howat et al.*, 2011] while Kangerlussuaq continued thinning through 2015 (Figure 2.6c). Helheim's terminus likely remained stable from 2008 to 2016 due to shallower water depths only a few kilometers farther upstream (Figure 2.1c), which may have limited its retreat over the last century [*Joughin et al.*, 2008b; *Andresen et al.*, 2012]. Based on the available bed-elevation measurements, no such shallower water depths or lateral constrictions in glacier width likely existed near Kangerlussuaq's grounding line to prevent further grounding-line retreat from 2008 to 2016 (Figure 2.2c). While there may be shallower water depths farther down fjord, if this is the case, the glacier does not appear to be reaching them. Instead, Kangerlussuaq's multiyear evolution from 2008 to 2016 appears to have been governed primarily by grounding-line retreat through a basal overdeepening.

As Kangerlussuaq thinned following its 2004/05 retreat [*Howat et al.*, 2011], its terminus changed from grounded to floating. By winter 2011/12, the glacier had a roughly 5-km-long floating ice tongue (Figure 2.2c), which may have increased the glacier's susceptibility to submarine melt [*Motyka et al.*, 2011; *Truffer and Motyka*, 2016]. During late winter 2010 through late summer 2011, a section of this floating ice tongue likely ungrounded (K05 in Figure 2.6c), primarily over an area with unknown bed geometry (Figure 2.2c). We suggest that there is a basal overdeepening in this region (red circle in Figure 2.2c), because surface-elevation measurements collected when the glacier was still grounded in this region from 2001 to 2008 indicate a flat or reverse surface slope (Figure 2.2b) [*Budd*, 1970]. Consequently, grounding-line retreat into this overdeepening caused speedup and thinning (Figure 2.6). This thinning diffused inland through a steepening of surface slopes (Figure A.4) [*Howat et al.*, 2007], and by 2015 the pattern of strongest thinning was centered ~20 km inland from the calving front (K20 in Figure 2.8b). While this ungrounding event occurred during a period of above-average sea-surface temperatures near the entrance to Kangerlussuaq Fjord [*Inall et al.*, 2014], it likely would have occurred even in the absence of this warming due to dynamic feedbacks associated with grounding-line retreat into deeper water [*Schoof*, 2007]. By winter 2011/12, Kangerlussuaq's grounding line had retreated into shallower water. Kangerlussuaq has since slowed and reduced its dynamic thinning rates (Figure 2.6c and Figure 2.8a), potentially signaling that its grounding line is in a more stable position now that it rests on a down-glacier bed slope [*Schoof*, 2007] in a region where the fjord narrows [K05 in Figure 2.2a; *Enderlin et al.*, 2013].

2.5.2 Seasonal variations in glacier velocity and surface elevation

Seasonal variations in glacier velocity are often linked to seasonal changes in terminus position or surface-melt-induced basal lubrication [*Howat et al.*, 2010; *Moon et al.*, 2014]. While less is known about seasonal dynamic thinning and thickening, they have also been connected to these processes [*Joughin et al.*, 2012; *Bevan et al.*, 2015]. For a lightly grounded glacier retreating into deeper water, terminus position serves as a proxy for water depth at the grounding line (e.g., Figure 2.3a), and consequently terminus position affects glacier velocity by modulating the force balance at the terminus [*Cuffey and Paterson*, 2010]. However, if a glacier has a large floating section, this relationship may not hold, particularly if there is little side drag where the floating section comes in contact with the fjord walls. At Jakobshavn, for example, glacier velocity and terminus position were highly correlated when the terminus was grounded but not when the terminus was floating [*Joughin et al.*, 2012]. Terminus variations can cause large seasonal speedups of >30 % [*Moon et al.*, 2014], while surface-melt-induced basal lubrication has been shown to cause more modest speedups of <10–15% [*Joughin et al.*, 2008c; *Moon et al.*, 2014].

Our results show that changes in terminus position and related dynamic feedbacks likely caused the observed seasonal variations in glacier velocity and surface elevation at Helheim (Figure 2.3). This hypothesis is contrary to the conclusions of *Bevan et al.* [2015], who suggested that seasonal dynamic thinning resulted from surface-melt-induced basal lubrication at Helheim.

Despite evidence that surface melt drains to the bed at Helheim [*Everett et al.*, 2016; *Poinar et al.*, 2017], surface-melt-induced basal lubrication has been shown to cause only small speedups of <5% on this glacier [*Andersen et al.*, 2010]. Iceberg-calving events, on the other hand, have been shown to coincide with much larger speedups at timescales of minutes to weeks [*Howat et al.*, 2005; *Nettles et al.*, 2008; *Murray et al.*, 2015]. Consistent with prior results, we observed the greatest seasonal speedups and dynamic thinning when Helheim's terminus was most retreated during the summers of 2010 and 2013 (Figure 2.3). This relationship is clearly illustrated in Figure 2.10a, which plots the dynamic surface-elevation change rate (first term in Equation 2.1) against the terminus position. When Helheim's terminus position was down fjord (up fjord) of its mean terminus position from 2008 to 2016, the glacier dynamically thickened (thinned), suggesting that the mean 2008–2016 terminus position closely corresponded with the location where the ice flux was equal to the balance flux. Consequently, Helheim's dynamic surface-elevation change rate primarily depended on the terminus position along the reverse bed slope, not on whether the glacier was presently advancing or retreating. These results confirm the findings of other studies, which have shown that Helheim is highly sensitive to changes at the terminus [*Howat et al.*, 2005; *Nick et al.*, 2009].

By contrast, seasonal variations in glacier velocity and surface elevation appeared to be more complex at Kangerlussuaq. We observed two distinct periods of seasonal speedup at Kangerlussuaq: one in the summer and one in the winter (Figure 2.6b). The summer speedup of 5–10% occurred around the time of peak surface melt. During summers 2011 and 2013, this speedup occurred while the terminus was still advancing, indicating that the speedup was not related to terminus retreat. Instead, surface-melt-induced basal lubrication likely caused this speedup [*Sundal et al.*, 2013], which was similar in magnitude to the magnitude of surface-melt-induced speedups observed at Helheim [*Andersen et al.*, 2010] and at other glaciers [*Moon et al.*, 2014]. Furthermore, all sample points showed an abrupt, synchronous velocity increase during this speedup, which may imply widespread basal lubrication across the lower glacier. The winter speedup, on the other hand, occurred when the terminus was most retreated, suggesting that the speedup resulted from reduced ice-shelf buttressing driven by terminus retreat.

In comparison to our findings at Helheim, there is no clear relationship between terminus position and the dynamic surface-elevation change rate at Kangerlussuaq (Figure 2.10b). Based on the similarity in timing between the summer speedup and seasonal dynamic thinning (Figure 2.6), it is possible that surface-melt-induced basal lubrication caused some dynamic thinning at Kangerlussuaq. However, even during summers with very small speedup events, such as summer 2009, we observed dynamic thinning of a similar magnitude to that observed during other summers (Figure 2.6). Consequently, other processes likely contributed to the observed dynamic thinning at Kangerlussuaq. While both changes in the ice-thickness and velocity gradients can affect the surface-elevation change rate (Equation 2.1), our results indicate that an increase in the velocity gradient typically accounted for ~75% of the observed seasonal dynamic thinning at Kangerlussuaq (~6 cm d^{-1} of ~8 cm d^{-1}; Text A.2). Changes in the velocity gradient could have resulted from several different processes, including thinning-induced changes in the effective pressure [*Howat et al.*, 2005] and changes in the terminus or grounding-line position [*Nick et al.*, 2009]. However, inopportune gaps in our record make it difficult to determine which of these processes contributed to seasonal dynamic thinning at Kangerlussuaq.

The different dynamic responses of Helheim and Kangerlussuaq to seasonal changes in terminus position are not surprising given differences in the spatial extent of floating ice near their termini (Figure 2.10). For a lightly grounded glacier, such as Helheim, terminus retreat into deeper water reduces basal and lateral resistance to flow and increases the ice thickness at the grounding line. Both of these processes require the glacier to speed up to restore force balance [*Howat et al.*, 2005]. For a glacier with a floating terminus confined within a narrow fjord, such as Kangerlussuaq, terminus retreat only reduces lateral resistance to flow, and consequently a smaller speedup is likely necessary to restore force balance. As a result, despite larger seasonal terminus variations at Kangerlussuaq than at Helheim, glacier velocities and surface elevations were more sensitive to terminus position at Helheim than at Kangerlussuaq (Figure 2.3 and Figure 2.6).

At both Helheim and Kangerlussuaq, variations in glacier velocity associated with seasonal terminus retreat and advance extended more than 25 km inland (Figure 2.5 and Figure 2.9). Velocity variations likely extended this far inland through some combination of diffusion due to a steepening of surface slopes [*Howat et al.*, 2005] and the initial perturbation in the force balance near the terminus [*Joughin et al.*, 2012]. In regions where we observed the greatest seasonal velocity variability, recent modeling studies indicate a weak bed (<40 kPa) [*Shapero et al.*, 2016], which should allow speedups associated with the initial perturbation in the force balance to extend farther inland [*Joughin et al.*, 2012]. While seasonal speedups associated with the initial perturbation in the force balance should be synchronous across the lower glacier, diffusion should cause a lag between speedup near the terminus and speedup farther inland. During summers 2010 and 2013, Helheim started speeding up at all sample points around the same time, indicating that this initial speedup likely resulted from terminus retreat into deeper water (Figure 2.3b). Glacier velocity 20 km inland (H20), however, peaked several months after glacier velocity peaked near the terminus (H02). This secondary, delayed response diffused inland through a steepening of surface slopes (Figure A.3). Consequently, both diffusion and bed strength likely contributed to the inland propagation of seasonal speedups at Helheim and Kangerlussuaq.

2.5.3 Seasonal variability in terminus position and iceberg-calving behavior

Seasonal variations in terminus position have been observed at many Greenland tidewater glaciers [*Howat et al.*, 2010; *Seale et al.*, 2011; *Schild and Hamilton*, 2013]. Typically, these variations are linked to oceanic or atmospheric changes that seasonally alter the iceberg-calving rate, such as changes in ice-mélange strength [*Amundson et al.*, 2010], submarine melt [*O'Leary and Christoffersen, 2013]*, and the availability of surface melt for hydrofracture [*Benn et al.*, 2007]. While some tidewater glaciers show a clear relationship between seasonal terminus variations and oceanic and atmospheric changes, other glaciers indicate a more complex relationship [*Schild and Hamilton, 2013]*. At Helheim, for example, *Schild and Hamilton* [2013] observed seasonal retreats that varied in magnitude by 2 km per year and in timing of onset by 60 days. We also observed significant variability in seasonal terminus variations at Helheim (Figure 2.3a). Our results suggest that this variability was partially related to seasonal dynamic thinning and thickening, which altered the spatial extent of floating ice near the terminus (Figure 2.3c). Furthermore, seasonal terminus variations were likely larger at Kangerlussuaq than at Helheim due to the presence of its year-round floating ice tongue.

When Helheim and Kangerlussuaq formed floating ice tongues, iceberg calving ceased during the winter and both glaciers seasonally advanced by >3 km. These large seasonal advances occurred every winter at Kangerlussuaq but only during winters 2010/11 and 2013/14 at Helheim (Figure 2.3a and Figure 2.6a). At Kangerlussuaq, seasonal advances occurred when more rigid ice mélange formed in the fjord (Figure 2.7), which likely suppressed iceberg calving [*Amundson et al.*, 2010; *Seale et al.*, 2011]. At Helheim, however, the ice mélange appeared to be similarly strong, if not slightly weaker, during winters when a floating ice tongue formed (Figure 2.4), likely indicating that large seasonal advances at Helheim did not result from changes in ice-mélange strength. Large seasonal retreats at Helheim, however, did occur during weaker mélange conditions (Figure 2.3e and Figure 2.4), suggesting that the ice mélange may still have affected iceberg-calving rates during other seasons. This result contradicts the conclusions of *Cook et al.*, [2014], who used a numerical model to show that changes in ice-mélange strength had little effect on Helheim's terminus position. While it is possible that another oceanic or atmospheric change, such as changes in submarine melt [*Straneo et al.*, 2011], can explain the varying magnitude of seasonal advances at Helheim, we suggest that these large seasonal advances followed summers with substantial dynamic thinning for a reason: this thinning caused the terminus to evolve from grounded to floating (Figure 2.3c), which affected iceberg-calving rates.

Iceberg calving is sensitive to the spatial extent of floating ice near the terminus *[Benn et al.*, 2007]. At the two extremes, grounded tidewater glaciers in Alaska and Greenland calve frequent, small non-tabular icebergs, and floating ice shelves in Antarctica calve infrequent, large tabular icebergs [*Walter et al.*, 2010; *Bassis and Jacobs*, 2013]. Similarly, Helheim and Kangerlussuaq typically calved non-tabular icebergs when their termini were grounded or nearly grounded and tabular icebergs when their termini were floating (Figure 2.3 and Figure 2.6) [*Joughin et al.*, 2008b]. Helheim calved non-tabular icebergs year-round but rarely calved tabular icebergs during the winter, which may indicate that different processes affect non-tabular and tabular iceberg calving [*Benn et al.*, 2007; *Amundson et al.*, 2010]. For example, near-terminus deviatoric stresses and strain rates tend to be smaller for a floating rather than grounded terminus, which likely causes slower rates of rift propagation and thereby promotes tabular iceberg calving [*Reeh*, 1968; *Alley et al.*, 2008]. When tabular icebergs do calve from the terminus, these icebergs typically remain upright; non-tabular icebergs, on the other hand, will likely overturn, which may promote further iceberg calving by flushing the ice mélange further away from the terminus

[Amundson et al., 2010]. Consequently, even if oceanic and atmospheric conditions were similar during different winters at Helheim, the glacier may only have been able to readvance by >3 km following summers with significant dynamic thinning, which affected iceberg-calving behavior.

Our results also suggest that non-tabular iceberg calving at Helheim occurred as a lightly grounded terminus is forced up a reverse bed slope [*Joughin et al.*, 2008b], contrary to the hypothesis of *James et al.* [2014]. If that is the case, then seasonal dynamic thinning may lessen this geometric effect, further enabling the terminus to readvance. As has been observed in other studies [*Joughin et al.*, 2008b; *James et al.*, 2014; *Murray et al.*, 2015], large rifts and depressions often formed within ~500 m of the calving front before non-tabular iceberg calving at Helheim. We did not observe any such rifts or depressions in the DEMs or satellite images before non-tabular iceberg calving at Kangerlussuaq. It is possible that rifts formed at Kangerlussuaq, but we did not observe them. However, this lack of observations may also imply that non-tabular iceberg calving occurred through a different mechanism there, perhaps because Kangerlussuaq typically had a floating, rather than lightly grounded, terminus.

The rifts and depressions that form before non-tabular iceberg calving at Helheim have been interpreted in two different ways. *Joughin et al.* [2008b] suggested that these depressions form as the terminus is pushed up a reverse bed slope faster than it can thin to flotation, while a region upstream remains at or near flotation. Deviatoric stresses in this depression should be sensitive to the basal topography and to the ice thickness near the terminus, since thicker ice will need to be forced farther up this reverse bed slope. Once a rift forms in this depression, enhanced rift growth may occur due to the strain-rate-weakening nature of ice [*Bassis and Ma*, 2015]. By contrast, *James et al.* [2014] interpreted these depressions as “flexion zones,” which form as the calving front advances into deeper water faster than it can viscously adjust to the buoyant disequilibrium. The ice must then adjust by brittle failure, causing the calving front to rotate outwards as a basal crevasse penetrates at depth. Based on the available bed-elevation measurements, Helheim’s terminus advanced into shallower water during non-tabular iceberg calving (Figure 2.1c). *James et al.* [2014] suggested that these bed-elevation measurements might be unreliable, but the bed-elevation measurements have since been re-processed, and we used those measurements in this study. Furthermore, Helheim’s high sensitivity to terminus position also implies retreat down a reverse bed slope (Figure 2.10a) [*Nick et al.*, 2009]. If rates of dynamic thinning and submarine melt were greater than the rate at which the calving front advanced into shallower water, then the calving front may still have come ungrounded *[James et al.*, 2014*; Murray et al.*, 2015]. However, when Helheim advanced to the top of the reverse bed slope and calved into deeper water, the terminus typically calved tabular rather than non-tabular icebergs. These observations may indicate that rift-driven, non-tabular iceberg calving typically occurs when a lightly grounded terminus is resting on a reverse bed slope. Consequently, seasonal dynamic thinning and thickening may affect non-tabular iceberg-calving rates by altering deviatoric stresses in the depression that forms upstream of the calving front.

While a full analysis of this mechanism and other potential controls on non-tabular and tabular iceberg calving is outside the scope of this study, our results highlight that seasonal terminus variations are affected by the spatial extent of floating ice near the terminus. For a lightly grounded glacier, such as Helheim, seasonal dynamic thinning and thickening can affect this spatial extent, which in turn affects iceberg calving. Consequently, temporal changes in the extent of floating ice may help explain why some glaciers, such as Helheim, show a clear seasonal pattern in terminus position and glacier velocity during some years but not during other years *[Howat et al., 2010; Schild and Hamilton*, 2013; *Moon et al*., 2014].

2.6 Conclusions

Our observations indicate that glacier geometry exerted a strong control on the seasonal and interannual evolution of Helheim and Kangerlussuaq from 2008 to 2016. These results are consistent with prior studies at Helheim and Kangerlusssuaq [*Howat et al.*, 2007; *Nick et al.*, 2009] and at other glaciers [e.g., *Joughin et al.*, 2012; *Motyka et al.*, 2017]. While Helheim stopped thinning shortly after its 2001–2005 retreat ended, Kangerlussuaq continued thinning through 2015. This thinning initially caused grounding-line retreat into deeper water, likely leading to further speedup, thinning, and retreat. By late summer 2011, Kangerlussuaq's grounding line had retreated into shallower water. Kangerlussuaq has since slowed and reduced its dynamic thinning rates, suggesting that its grounding line may be in a more stable position now that it rests on a down-glacier bed slope. Helheim's stable grounding-line position from 2008 to 2016 appears to be related to a down-glacier bed slope a few kilometers upstream of its terminus position. Given that both Helheim and Kangerlussuaq flow through basal troughs that become narrower and shallower <20 km upstream of their current grounding-line positions, the potential retreat of these glaciers over the next few centuries appears to be limited [*Nick et al.*, 2013].

We also observed different seasonal variability in terminus position, glacier velocity, surface elevation, and iceberg-calving behavior at Helheim and Kangerlussuaq, which we partially attribute to differences in ice dynamics related to the glaciers' geometries. Despite larger seasonal retreats at Kangerlussuaq than at Helheim, glacier velocity and surface elevation were more sensitive to terminus position at Helheim than at Kangerlussuaq. Helheim is likely more sensitive to terminus position due to its lightly grounded, rather than floating, terminus. Iceberg-calving behavior also depended on glacier geometry, with tabular iceberg calving typically indicating a floating terminus and rift-driven, non-tabular iceberg calving indicating a lightly grounded terminus resting on a reverse bed slope. Our results suggest that seasonal velocity variability and iceberg-calving behavior may provide additional clues about glacier geometry where we presently have limited bed- and surface-elevation measurements.

Given that seasonal elevation variations alter glacier geometry, these elevation variations may also affect the dynamic response of tidewater glaciers to environmental change. Many studies [*Schild and Hamilton*, 2013; *Moon et al.*, 2014] have found a clear, seasonal relationship between terminus position and environmental change at some tidewater glaciers, while other glaciers indicate a more complex relationship. Our results suggest that lightly grounded glaciers may be more likely to exhibit an inconsistent relationship between terminus position and environmental change, because seasonal elevation variations can affect the spatial extent of floating ice near their termini and thereby influence iceberg-calving behavior. Consequently, the effect of an oceanic or atmospheric change on tidewater glacier dynamics may differ depending on when the change occurs relative to seasonal changes in glacier geometry. Long-term observations of seasonal elevation change are currently only available for a few tidewater glaciers in Greenland; however, seasonal dynamic thinning/thickening is likely widespread, and further research is needed to better understand its importance for the long-term evolution of the Greenland Ice Sheet.

2.7 Acknowledgments

L.M. Kehrl was supported by the Department of Defense (DoD) through the National Defense Science and Engineering Graduate Fellowship (NDSEG) Program, I. Joughin was supported by the NSF Office of Polar Programs (NSF-OPP) through the Center for Remote Sensing of Ice Sheets (CReSIS) (NSF ANT-0424589), D.E. Shean was supported by a NASA NESSF fellowship (NNX12AN36H), and L. Krieger was supported by Deutsche Forschungsgemeinschaft (DFG, FL 848/1-1). The TerraSAR-X and TanDEM-X data were provided by the German Aerospace Center (DLR), projects HYD0754 and XTI_GLAC0400. NASA's MEaSUREs Program (NNX08AL98A andNNX13AI21A) supported the SAR processing. Velocity data are available from the National Snow and Ice Data Center (nsidc.org/data/measures/gimp). We acknowledge bed-elevation measurements from CReSIS (ANT-0424589 and NNX10AT68G) and surface-elevation measurements from NASA's Airborne Topographic Mapper (ATM) Program. We thank Claire Porter, Paul Morin, and others at the Polar Geospatial Center (NSF ANT-1043681), who managed tasking, ordering, and distribution of the WorldView/GeoEye stereo-imagery. Resources supporting the Worldview DEM processing were provided by the NASA High-End Computing (HEC) Program through the NASA Advanced Supercomputing (NAS) Division at Ames Research Center. SPOT-5 DEMs and imagery were provided at no cost by the French Space Agency (CNES) through the SPIRIT International Polar Year project. RACMO2.3 data were kindly provided by Brice Noël and Michiel van den Broeke (Utrecht University). This study used sea ice fraction from the Operational Sea Surface Temperature and Sea Ice Analysis System (OSTIA) from the Copernicus Marine Service. Other data are available from the author upon request. We thank Editor Bryn Hubbard and two anonymous reviewers for their helpful comments that improved the quality and clarity of this manuscript.

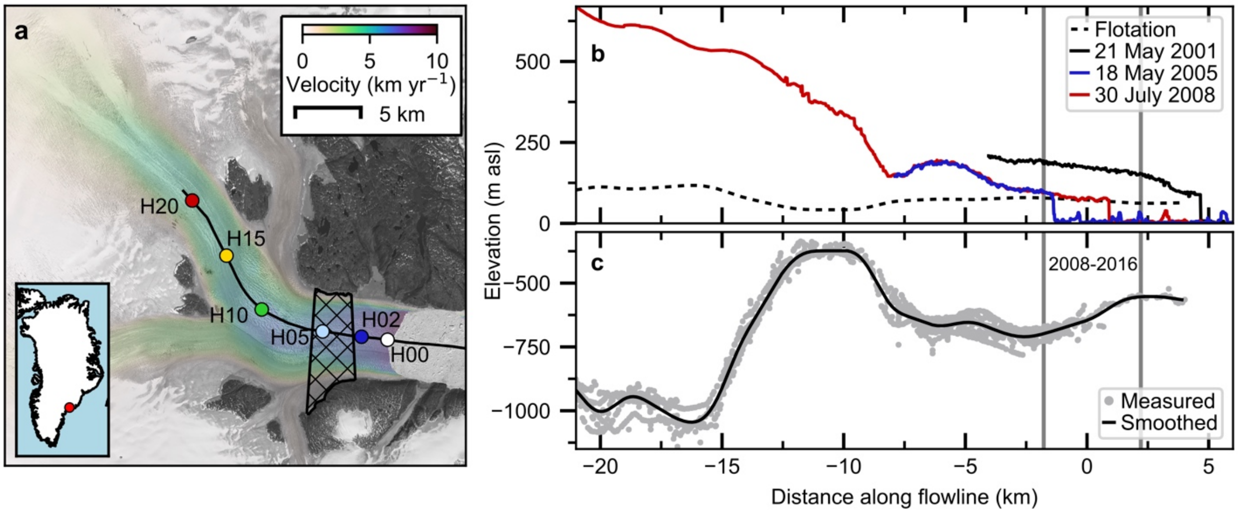

Figure 2.1. (a) Glacier velocity at Helheim from 30 June to 11 July 2014. Background image is the Landsat 8 panchromatic band from 4 July 2014. Colored circles indicate the locations of sample points plotted in Figure 2.3. Sample point names indicate the distance in kilometers from the mean terminus position from 2008 to 2016. We calculated surface-elevation change rates for the hatched region. Black curve indicates the profile shown in (b-c). (b) Glacier surface elevations from ATM. Black dashed line is the height where the ice should become afloat. (c) Smoothed bed elevations and all measured CreSIS bed elevations within 200 m of the profile. Gray vertical lines indicate the range of observed terminus positions from 2008 to 2016.

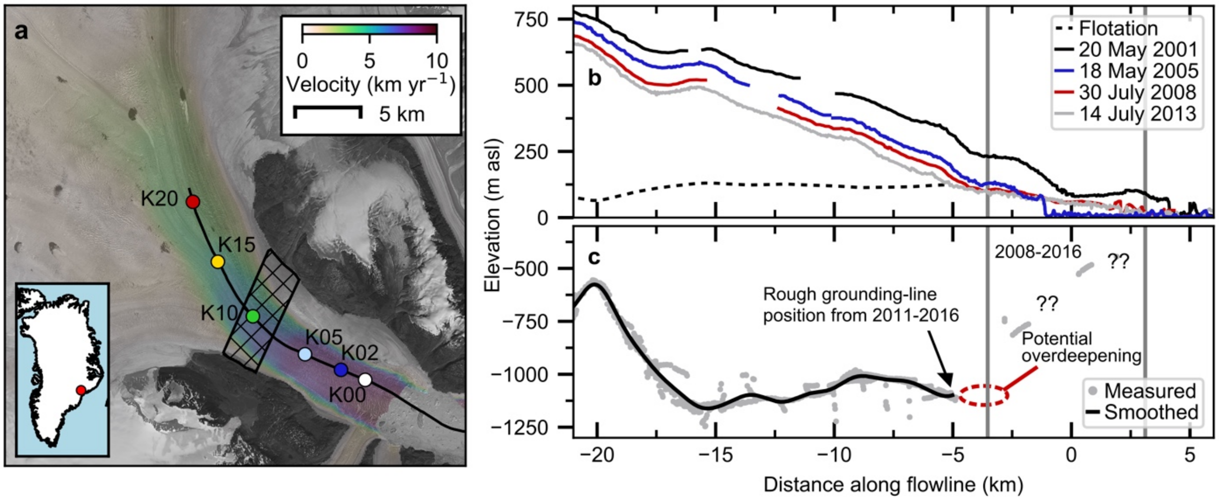

Figure 2.2. (a) Glacier velocity at Kangerlussuaq from 1-12 July 2014. Background image is the Landsat 8 panchromatic band from 6 July 2014. Colored circles indicate the locations of sample points plotted in Figure 2.6. We calculated surface-elevation change rates for the hatched region. Black curve indicates the profile shown in (b, c). See Figure 2.1 for descriptions of panels (b,c). Black arrow indicates the approximate location of Kangerlussuaq’s grounding line from 2011 to 2015, and the red ellipse indicates the location of a potential overdeepening discussed in the text. Bed elevations are very poorly constrained downstream of -5 km because the glacier was typically floating in this region when radar thicknesses were collected.

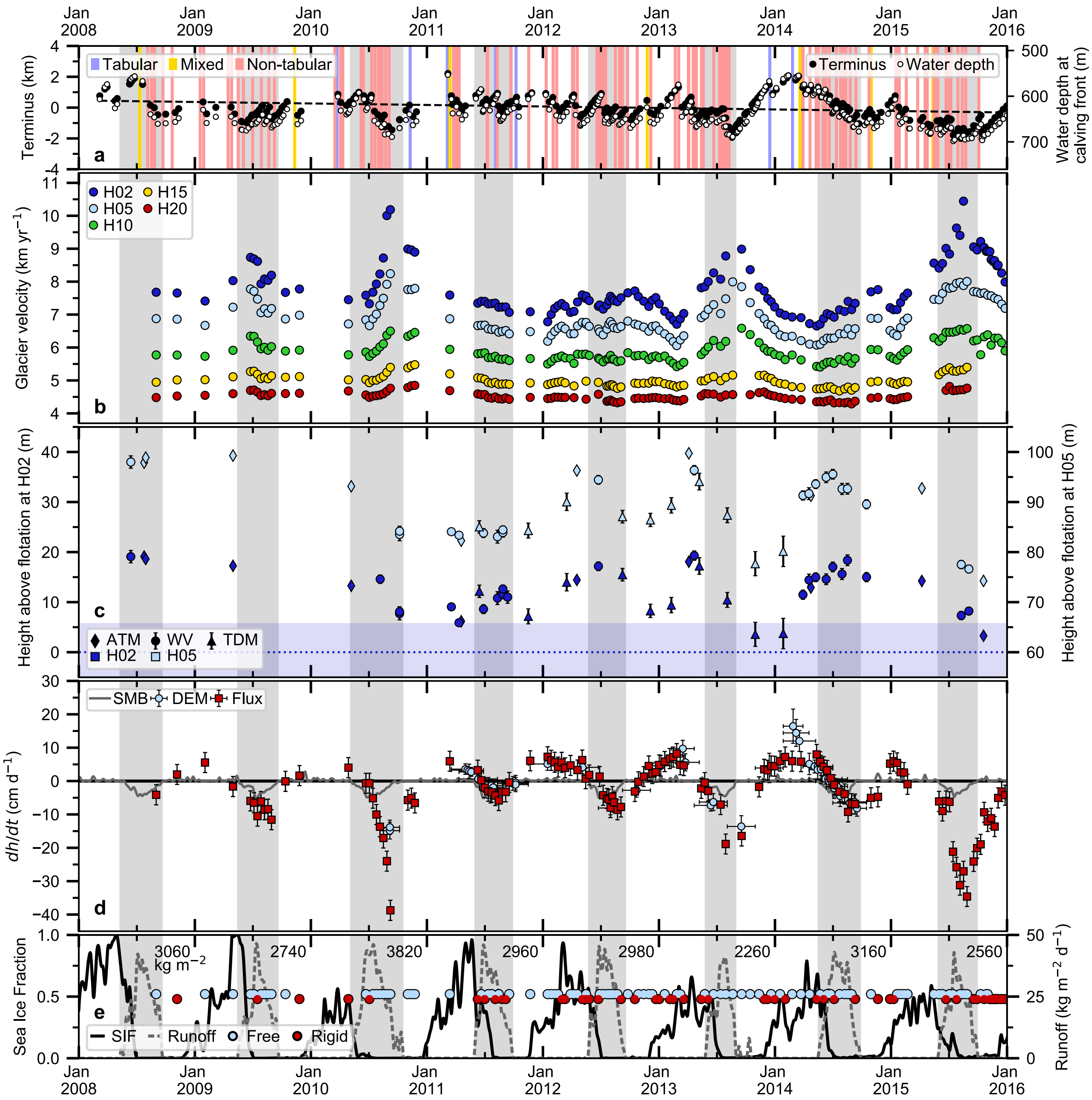

Figure 2.3. Observational record for Helheim. (a) Terminus position relative to the 2008–2016 average, water depth at the calving front, and calved iceberg type, (b) glacier velocity at sample points H02-H20 in Figure 2.1a, (c) height above flotation at H02 and H05, (d) surface-elevation change rates from the DEM and flux-gate methods, (e) ice-mélange conditions from TSX velocity estimates, sea-ice fraction from OSTIA, and surface runoff from RACMO2.3. Dashed line in (a) shows the linear trend in the observed terminus positions. Blue dotted line in (c)

indicates the height where H02 should become afloat with 50-m uncertainties in the bed elevation indicated by the shaded bar. Gray line in (d) shows the surface-elevation change rate due to surface mass balance processes predicted by RACMO2.3. Text above runoff curve in (e) indicates the total surface runoff for each year. Blue and red circles in (e) indicate free and rigid ice-mélange conditions, respectively. Vertical shaded bars indicate periods of surface runoff.

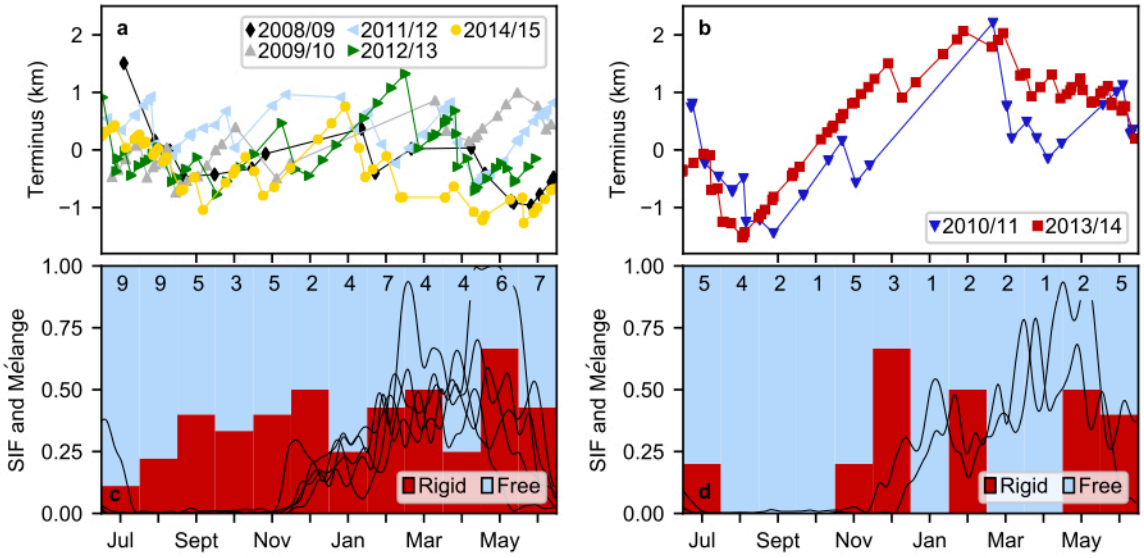

Figure 2.4. (a,b) Terminus position and (c,d) SIF and ice-mélange conditions during years when Helheim did (right) and did not (left) seasonally advance by >3 km. Ice-mélange conditions have been monthly binned for all years in each panel. Numbers indicate the total number of TSX velocity estimates used in each binning.

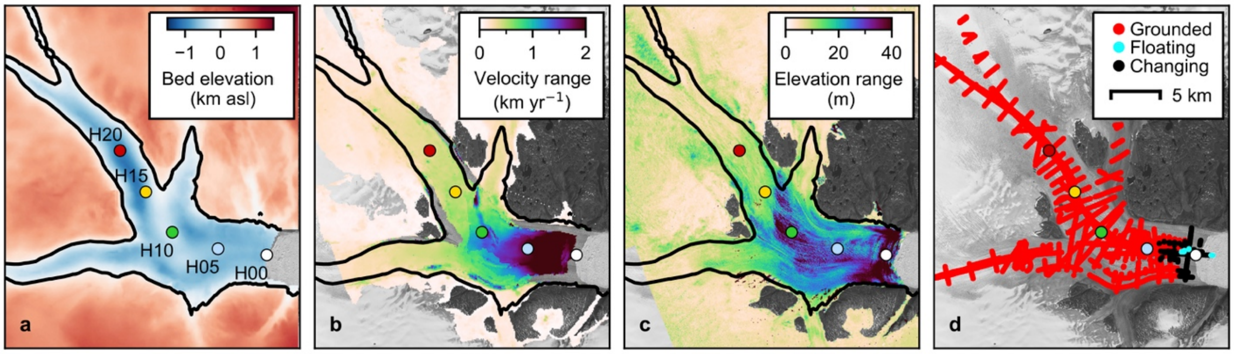

Figure 2.5. Range of observed glacier velocities and surface elevations at Helheim from 2011 to 2015. All linear trends have been removed before calculating the range. (a) Bed elevation from *Morlighem et al.* [2014], (b) range of observed glacier velocities, (c) range of observed surface elevations, and (d) the resulting changes in the flotation condition. Regions in red remained grounded, regions in blue remained floating, and regions in black changed between grounded and floating. Black curve in (a-c) indicates the region where the bed is below sea level.

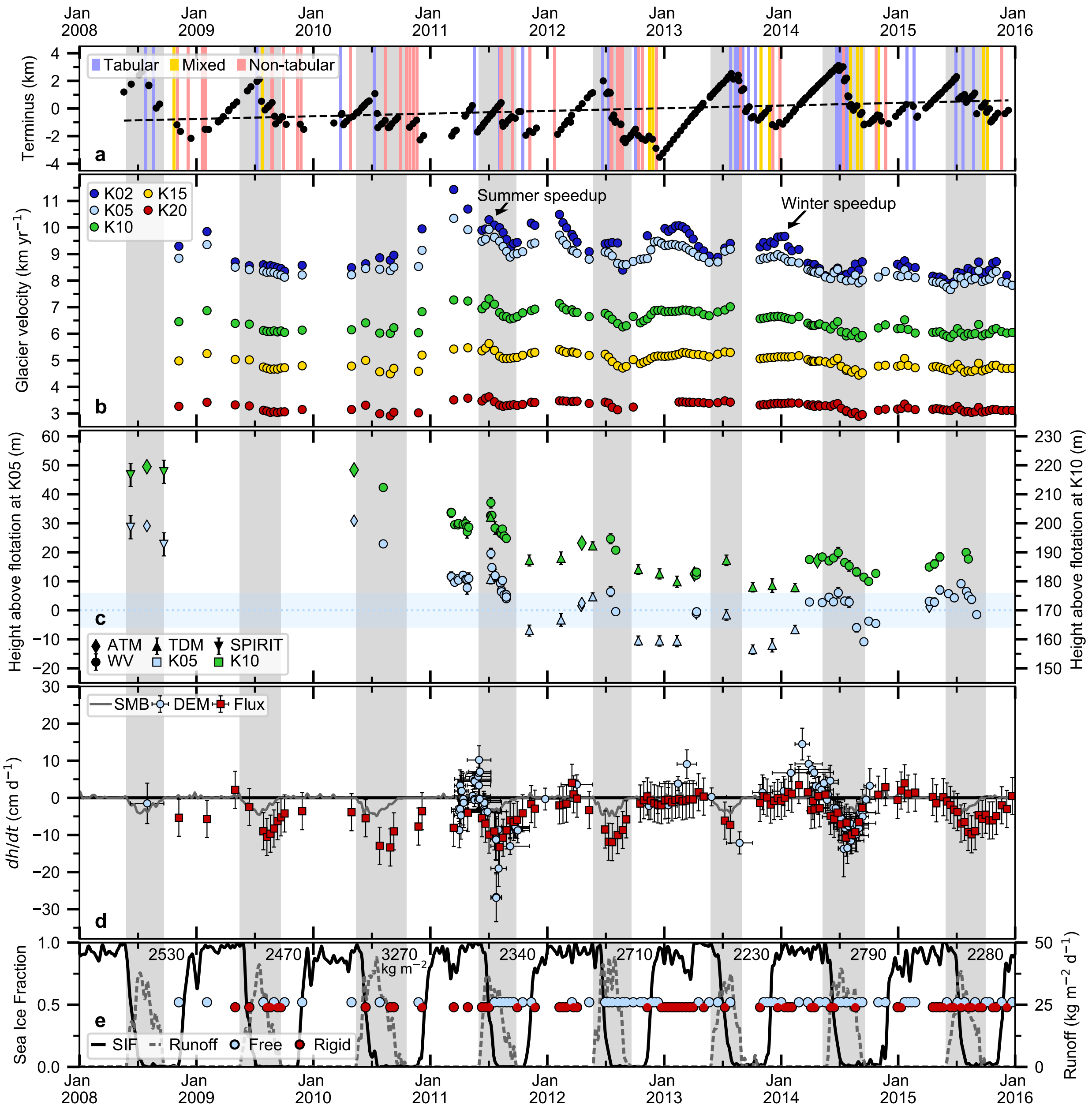

Figure 2.6. Observational record for Kangerlussuaq. Subpanels are the same as in Figure 2.3. Note that (c) shows height above flotation at K05 and K10. Light blue dotted line in (c) indicates the height where K05 should become afloat with 50-m uncertainties in the bed elevation indicated by the shaded bar.

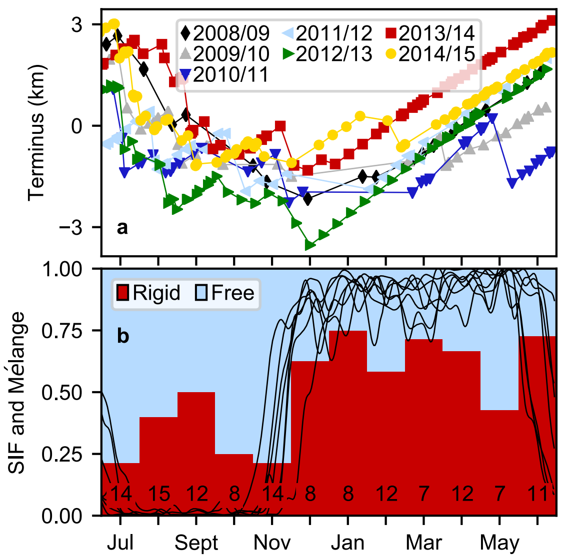

Figure 2.7. (a) Terminus position and (b) SIF and ice-mélange conditions at Kangerlussuaq. Ice-mélange conditions have been monthly binned, with the number indicating the total number of TSX velocity estimates used in each binning.

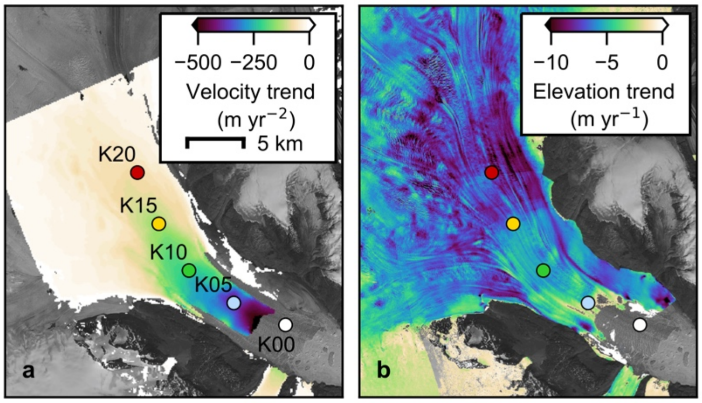

Figure 2.8. Linear trends in (a) glacier velocity and (b) surface elevation (i.e., average thinning rate) from 2011 to 2015 at Kangerlussuaq. All plotted trends have a p-value < 0.05.

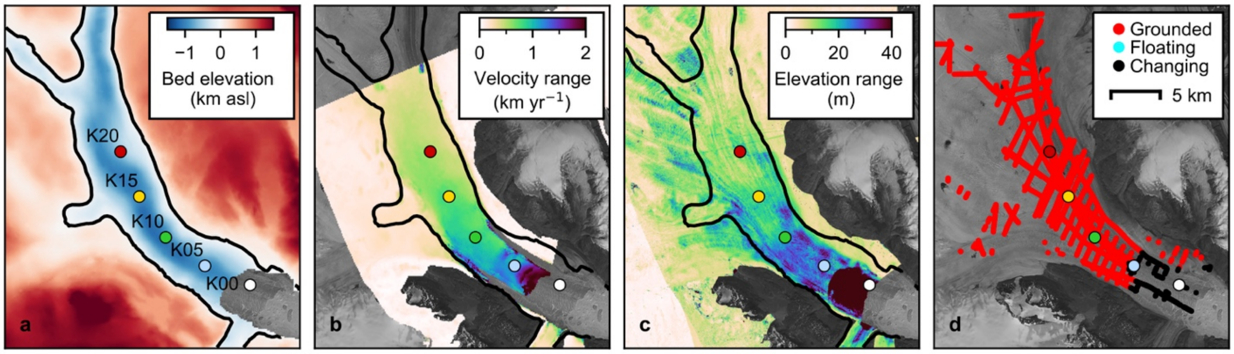

Figure 2.9. Range of observed glacier velocities and surface elevations from 2011 to 2015 at Kangerlussuaq. See Figure 2.5 for a description of the subpanels.

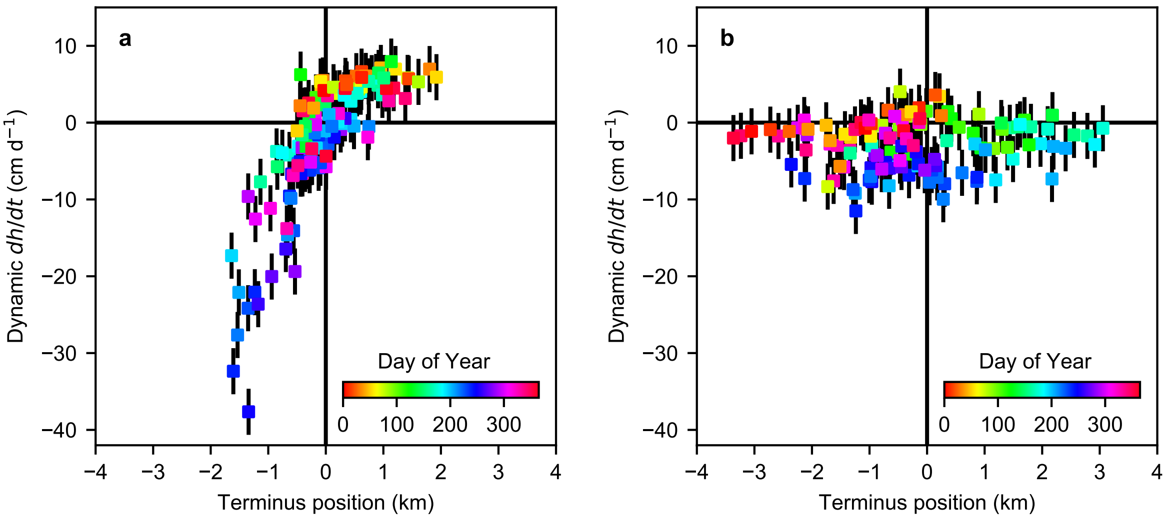

Figure 2.10. Relationship between the terminus position and dynamic surface-elevation change rate (first term on the right in Equation 2.1) at (a) Helheim and (b) Kangerlussuaq. Terminus position is relative to the mean 2008–2016 terminus position. Marker color indicates the day of year.

Chapter 3. Basal conditions for Helheim and Kangerlussuaq Glaciers, Southeast Greenland, from 2001 to 2016

Chapter 3 will be submitted to *The Cryosphere* under the title "Basal conditions for Helheim and Kangerlussuaq Glaciers, Southeast Greenland, from 2001 to 2016." The manuscript is authored by L. Kehrl, I. Joughin, B.E. Smith, and I. M. Howat. The supplement for this paper can be found in Appendix B. The dissertation author was the primary investigator and author of this paper.

3.1 Abstract

Basal conditions vary spatially and temporally under Greenland tidewater glaciers and can affect their response to climate change. Yet, these variations are not well understood or quantified. In this study, we investigated seasonal and interannual changes in basal conditions at Helheim and Kangerlussuaq glaciers from 2001 to 2016 using control methods. To test the sensitivity of the inferred basal conditions to the choice of forward model, we used forward models that solved both the full Stokes equations and the shallow-shelf approximation. Consistent with previous studies, we find a weak bed under the fast-flowing regions of Helheim and Kangerlussuaq that supports little of the driving stress. Embedded within the weak bed are sticky spots that fully support the local driving stress and resist basal sliding. When Helheim and Kangerlussuaq retreated, sped up, and thinned in the early 2000s, the basal shear stress decreased across the lower glacier. The basal shear stress also varied seasonally at Kangerlussuaq, reaching a maximum value in late summer or early fall, likely reflecting the development of a more efficient subglacial drainage system. It was less clear whether seasonal variations in the basal shear stress occurred at Helheim. The observed temporal relationship between the basal shear stress and basal velocity at Helheim and Kangerlussuaq likely cannot be explained by a Weertman basal sliding law or Mohr-Coulomb

parameterization; instead, we suggest that our snapshot inversions support spatially variable basal conditions, with different regions of the bed likely following different basal sliding laws.

3.2 Introduction

Many Greenland tidewater glaciers retreated, sped up, and thinned in the early 2000s [*Rignot and Kanagaratnam*, 2006; *Moon and Joughin*, 2008; *Moon et al.*, 2012]. While ocean warming likely contributed to this widespread retreat [*Holland et al.*, 2008; *Straneo et al.*, 2010], speedup and thinning also propagated inland through dynamic feedbacks [*Nick et al.*, 2009]. Speedup near the terminus causes thinning, which can steepen the surface slope, increase the driving stress, and allow the speedup to diffuse farther inland [*Howat et al.*, 2005]. Thinning can also reduce the effective pressure, which is the difference between the ice overburden pressure and the subglacial water pressure. The resistance to flow generated at the ice bed depends on the effective pressure, so a reduction in the effective pressure can cause additional speedup and thinning [*Joughin et al.*, 2012; *Habermann et al.*, 2013]. Inland thinning can account for over 75% of a glacier's dynamic mass loss [*Price et al.*, 2011], so understanding the processes that control the magnitude and extent of the inland response is critical for projecting future sea-level rise.

Much of a glacier catchment's inland response is affected by properties at its bed, which can vary spatially and temporally [*Clarke*, 2005]. Glacier beds are often divided into two types: hard and soft. Basal sliding over a hard, rough bed depends on regelation and creep around bed obstacles [*Weertman*, 1957] and cavitation [*Iken*, 1981; *Schoof*, 2005], whereas sliding over a soft bed depends on the deformation of the subglacial sediment [*Tulaczyk et al.*, 2000]. Both soft- and hard-bedded sliding can be affected by changes in the effective pressure: cavity formation can smooth bed obstacles on a hard bed [*Schoof*, 2005], and changes in the effective pressure can alter a soft bed's basal yield stress [*Tulaczyk et al.*, 2000]. While physically based models for basal sliding have been developed to describe these processes [e.g., *Gagliardini et al.*, 2007; *Schoof*, 2005], such models can be difficult to incorporate into ice-sheet models due to their poorly constrained parameters.

Consequently, most ice-sheet models use a Weertman sliding law, which relates the basal shear stress τ_b to the basal velocity u_b through a power law

$$\tau_b = \beta {u_b}^{1/m}, \tag{3.1}$$

where the basal friction coefficient β is a positive number and m is the sliding law exponent [*Weertman*, 1957]. The value of β depends on bed properties, including bed roughness, type, and effective pressure. Depending on the value of m, Eq. (3.1) can yield different types of basal sliding; with $m = 1$, Eq. (3.1) corresponds to a linear-viscous bed model [*Alley et al.*, 1986; *Blankenship et al.*, 1986], whereas $m = 3$ is often assumed to represent basal sliding over a hard bed [*Cuffey and Paterson*, 2010]. As $m \rightarrow \infty$, Eq. (3.1) approximates a plastic law for sediment deformation, where the basal shear stress is independent of the basal velocity. Sea-level rise projections are sensitive to the choice of m [*Ritz et al.*, 2015; *Brondex et al.*, 2017], as larger values cause changes at the ice-ocean boundary to propagate faster and farther inland [*Price et al.*, 2008].

While inverse methods can be used to infer β from a single set of observations for a given value of m [*MacAyeal*, 1993; *Arthern and Gudmundsson*, 2010], determining the best value of m requires observations collected at different times with substantially different basal shear stresses and/or basal velocities. In the inverse problem, the basal shear stress τ_b must achieve stress balance and is therefore independent of the value of m [*Joughin et al.*, 2004a]. If $m = 1$ in the inverse problem, then β accounts for any nonlinearity in the true value of m. *Gillet-Chaulet et al.* [2016] assimilated five years of surface velocities for Pine Island Glacier, West Antarctica, into a numerical model that solved the shallow-shelf approximation to infer a temporally constant β

using different values of m. Values of $m \leq 3$ underestimated the observed speedup from 1996 to 2010, while $m = 20$ produced the closest match to observations, likely implying plastic deformation of the underlying sediment. Similarly, *Joughin et al.* [2010] showed that the observed dynamic thinning at Pine Island Glacier could be explained by a mixed bed model, with plastic deformation in areas where $\tau_b < 40$ kPa and $m = 3$ elsewhere. At Greenland's largest glacier, Jakobshavn Isbrae, *Habermann et al.* [2013] found that a plastic Mohr-Coulomb parameterization could account for the temporal evolution of the basal shear stress from 1985 to 2008. While the above studies provide evidence for plastic deformation beneath tidewater glaciers in Greenland and Antarctica, these studies have been constrained by only a few sets of observations collected over several decades and consequently have neglected shorter, seasonal variations that might provide additional insight into the basal dynamics of tidewater glaciers.

In this study, we investigated seasonal and interannual changes in basal conditions at two of Greenland's largest tidewater glaciers, Helheim (HG) and Kangerlussuaq (KG), from 2001 to 2016 (Figure 3.1). Similar to many Greenland tidewater glaciers [*Moon and Joughin*, 2008; *Moon et al.*, 2012], HG and KG retreated, accelerated, and thinned in the early 2000s [*Rignot et al.*, 2004; *Howat et al.*, 2007; *Stearns and Hamilton*, 2007]. Both glaciers ended their retreats by 2006, but HG stopped thinning while KG continued thinning through 2015 [*Howat et al.*, 2011; *Bevan et al.*, 2012; *Kehrl et al.*, 2017]. HG and KG also seasonally retreated, sped up, and thinned from 2011 to 2015 [*Sundal et al.*, 2013; *Bevan et al.*, 2015; *Kehrl et al.*, 2017]. HG seasonally sped up and thinned in the late summer when its terminus was most retreated; KG, by contrast, sped up during the mid-summer and mid-winter in response to changes in surface melt and terminus position, respectively [*Kehrl et al.*, 2017].

To better understand the role of basal conditions in the seasonal and interannual evolution of HG and KG, we ran a series of steady-state inversions for both glaciers from 2001 to 2016. Following Goldberg et al. (2015), we refer to these inversions as “snapshot” inversions, because they are constrained by surface velocity and elevation measurements that are assumed to be contemporaneous. Each snapshot inversion was constrained by surface velocity and elevation measurements that were collected within the same month. We tested the sensitivity of the inferred basal conditions to the choice of forward model by using models that solved both the full Stokes equations and the shallow-shelf approximation [*MacAyeal*, 1989]. We focus our discussion on spatial and temporal patterns in the basal shear stress that remain consistent across all models. These patterns provide insight into the form of the basal sliding law under two of Greenland’s largest tidewater glaciers.

3.3 Methods

We used control methods [*MacAyeal*, 1993; *Morlighem et al.*, 2010; *Gillet-Chaulet et al.*, 2012] along with four forward models implemented in Elmer/Ice [*Gagliardini et al.*, 2013] to infer changes in basal conditions at KG and HG from 2001 to 2016. In the following sections, we first describe the data used to constrain the models and then describe our modelling approach.

3.3.1 Data

To develop a detailed timeseries of glacier surface velocity and elevation from 2001 to 2016, we combined data products from several satellite missions. For 2001 to 2011, we used surface velocity measurements from optical feature tracking of Landsat and Advanced Spaceborne Thermal Emissivity and Reflection Radiometer (ASTER) imagery [*Howat*, 2017]. Surface velocities for 2011 to 2016 were derived from speckle tracking of TerraSAR-X and TanDEM-X

(TSX) radar mosaics [*Joughin*, 2002; *Joughin et al.*, 2016; *Kehrl et al.*, 2017]. Reported uncertainties are ~3% for both velocity products [*Joughin et al.*, 2010a; *Howat*, 2017], but the uncertainty in the TSX velocity estimates may be even lower than this value due to recent improvements in Greenland digital elevation models [*Joughin et al.*, 2018]. To constrain glacier geometry, we used bed elevations from BedMachine V3 [*Morlighem et al.*, 2017] and surface elevations from ASTER [*Howat et al.*, 2007], SPIRIT [*Korona et al.*, 2009], Worldview, and TanDEM-X (TDM) [*Kehrl et al.*, 2017]. Reported elevation uncertainties are 7–10 m for ASTER [*Fujisada et al.*, 2005; *San and Süzen*, 2005], 6 m for SPIRIT [*Korona et al.*, 2009], and < 2 m for Worldview and TDM [*Shean et al.*, 2016; *Kehrl et al.*, 2017].

3.3.2 Modeling

To infer changes in basal conditions from 2001 to 2016, we ran 21 and 24 snapshot inversions for HG and KG, respectively. Each snapshot inversion was constrained by a set of surface velocity and elevation measurements, which were collected within a month of one another, and, for our purposes are effectively contemporaneous. This is an improvement in technique over previous studies [e.g., *Joughin et al.*, 2009; *Shapero et al.*, 2016] that used data collected over several years because contemporaneous data were unavailable. The data used in each inversion are given in Supplement Table B.1 and Table B.2. In the following sections, we describe the four forward models used for each snapshot inversion and the inverse problem.

3.3.2.1 Forward models

To test the sensitivity of the inferred basal conditions to the choice of forward model, we implemented four forward models using the finite-element package Elmer/Ice [*Gagliardini et al.*, 2013]. Two models solved the full Stokes equations, and the other two solved the equations with the depth-averaged shallow-shelf approximation [*MacAyeal*, 1989]. In all models, the constitutive relationship for ice flow is given by Glen's flow law [*Glen*, 1955] with an effective viscosity

$$\eta = \frac{1}{2}(EA)^{-1/n}\dot{\varepsilon}_e^{(1-n)/n}, \tag{3.2}$$

where E is an enhancement factor, A is the flow law parameter, $n = 3$ is the flow law exponent, and $\dot{\varepsilon}_e$ is the second invariant of the strain rate tensor. The value of E depends on ice fabric and water content; we set $E = 3$ in all models to account for polar ice undergoing simple shear [*Cuffey and Paterson*, 2010]. The value of A depends on the ice temperature through an Arrhenius relationship. Two models used a constant ice temperature of –10 °C, while the other two used spatially variable ice temperatures calculated with a steady-state thermomechanical model [*Zwinger et al.*, 2007]. We ran the thermomechanical model for the full HG and KG drainage basins [*Zwally et al.*, 2012], constrained at the glacier surface by surface temperatures from the Regional Atmospheric Climate Model Version 2.3 (RACMO 2.3) [*van Angelen et al.*, 2013; *Noël et al.*, 2015] and at the glacier bed by a geothermal heat flux of 60 mW m^{-2} [*Davies*, 2013]. The thermomechanical model calculated a temperate basal layer with a thickness of < 100 m over the regions of fast flow at KG and HG, with colder ice above (Figure B.1). The four forward models tested in this study include all four combinations of full Stokes (FS) or shallow-shelf approximation (SSA) with a constant (CT) or thermomechanical (MT) temperature model: FS-CT, FS-MT, SSA-CT, and SSA-MT.

In all models, we applied a Robin boundary condition given by Eq. (3.1) at the glacier bed and treated the glacier surface as a stress-free surface. We applied a Dirichlet boundary condition as determined by the observed surface velocity on all other boundaries. By imposing the observed velocity, we accounted for changes in the stress balance that occurred due to forcings both internal and external to the model domain, including downstream changes in effective pressure, grounding-line position, and terminus position. To discretize the model domain, we used an unstructured planar mesh with a resolution of ~250 m, which we vertically extruded to 12 layers for the full Stokes models. We limited our model domain to an upstream region where the glacier remained grounded to prevent uncertainties in grounding-line position from affecting our analysis (Figure 3.1).

3.3.2.2 Inverse problem

For each set of forward model and observations (Table B.1 and Table B.2), we used control methods [*MacAyeal*, 1993; *Morlighem et al.*, 2010; *Gillet-Chaulet et al.*, 2012] to infer the basal friction coefficient β over the glacier bed Γ_b by minimizing the misfit J_o between the modeled and observed horizontal velocity over the glacier surface Γ_s

$$J_o = \frac{1}{2}\int_{\Gamma_s}\left((u_x - {u_x}^{obs})^2 + (u_y - {u_y}^{obs})^2\right) d\Gamma, \tag{3.3}$$

where $\boldsymbol{u} = (u_x, u_y)$ is the modeled velocity and $\boldsymbol{u}^{obs} = ({u_x}^{obs},\ {u_y}^{obs})$ is the observed velocity. The area-weighted root-mean-square error (RMSE) is then $\sqrt{2J_o/A_{\Gamma_s}}$, where A_{Γ_s} is the area of the glacier surface.

In the inversions, we set $m = 1$ in Eq. (1) because the inferred basal shear stress should be independent of the value of m [*Joughin et al.*, 2010b; *Minchew et al.*, 2016]. To ensure a positive value of β, we solved the inverse problem with respect to a new variable α, where $\beta = \alpha^2$.

As in any ill-posed inverse problem, many possible solutions for β exist that fit the observed surface velocity to within the combined model and measurement error. It is not possible to differentiate between these solutions to find the true value of β, and consequently, an additional constraint must be added to find a solution that does not over-fit the data [*Habermann et al.*, 2012].

In this study, we added a Tikhonov regularization term to the cost function which penalized the first spatial derivative of β

$$J_{reg} = \frac{1}{2}\int_{\Gamma_b}\left(\left(\frac{\partial\beta}{\partial x}\right)^2 + \left(\frac{\partial\beta}{\partial y}\right)^2 + \left(\frac{\partial\beta}{\partial z}\right)^2\right)d\Gamma. \tag{3.4}$$

The total cost function J to be minimized is then

$$J = J_o + \lambda J_{reg}, \tag{3.5}$$

where the regularization parameter λ determines the trade-off between the data-model misfit J_o and the model norm J_{reg}. Ideally, we would choose the smoothest possible solution for β (i.e., the largest value of λ) that fits the observed velocity to within the combined model and measurement errors [*Aster et al.*, 2005]. This approach, however, is often not possible because errors in the model due to poorly constrained parameters and model simplifications are frequently not known. As a result, the L-curve method is often used to choose the optimal value of λ *[Jay-Allemand et al.*, 2011; *Habermann et al.*, 2013; *Shapero et al.*, 2016]. As the value of λ increases, the data-model misfit remains relatively constant up to a point, after which it abruptly increases. In the L-curve method, this inflection point corresponds to the optimal value of λ, because it provides the smoothest possible solution that can be achieved without drastically increasing the data-model misfit. It is important to remember that our choice of a smooth solution does not imply that the true solution must also be smooth; rather it is an acknowledgment that if the true solution contains more detail then we cannot distinguish it from noise, and so there is no point in including this level of detail in our solution.

3.3.3 Driving stress

To determine the importance of τ_b for the overall stress balance of the glacier, we calculated the along-flow component of the driving stress

$$\tau_d = \boldsymbol{\tau_d} \cdot \boldsymbol{u}^{obs} \,/\, \|\boldsymbol{u}^{obs}\|. \tag{3.6}$$

While the driving stress is aligned with the flow direction over large length scales, the driving stress can take on negative values over length scales less than a few ice thicknesses for reverse slopes and thereby oppose ice flow. Consequently, comparing the magnitudes of τ_b and τ_d without taking the flow direction into account can lead to a poor interpretation of the stress balance.

3.4 Results

Following the methods outlined above, we produced snapshot inversions for HG and KG from 2001 to 2016. Our snapshot inversions indicate seasonal and interannual variations in τ_b that are robust across all forward models. In the following sections, we describe the model performance, spatial and temporal variations in the basal shear stress, and the relationship between the basal velocity and basal shear stress.

3.4.1 Data-model misfit and regularization

We first used the L-curve method to determine an optimal value of the regularization parameter λ (Eq. (3.5)), as shown in Figure 3.2 for KG and Supplement Figure B.2 for HG. Based on these figures, we used $\lambda = 1e13$ for SSA-CT and SSA-MT and $\lambda = 1e12$ for FS-CT and FS-MT in all following inversions. With our choice of λ, the mean absolute difference between the modeled and observed velocities was < 200 m yr^{-1} for all velocity bins, corresponding to mean absolute residuals of > 5% for regions where u^{obs} < 1 km yr^{-1} and ~3% for regions where u^{obs} > 1 km yr^{-1}, as shown in Figure 3.2c for KG and Supplement Figure B.2c for HG. The expected uncertainty for the TSX velocity estimates is < 3% [*Joughin et al.*, 2010a, 2018], indicating that the models underfit the data (i.e., had misfits significantly larger than those expected based on the data error estimates) in regions of slow flow and provided a reasonable fit to the observations in regions of fast flow.

Figure 3.2d shows the data-model misfit for all snapshot inversions from 2001 to 2016 at KG. The area-weighted RMSE was ~150–250 m yr^{-1} for inversions before 2008 and ~125–150 m yr^{-1} for inversions after 2008. Out of the four forward models, FS-CT provided the closest match to the observed surface velocities for 22 of the 24 inversions at KG and for all 21 inversions at HG (Supplement Figure B.2d).

3.4.2 Spatial patterns in the inferred basal shear stress

The inferred basal shear stresses for the four forward models are shown in Figure 3.3 for KG for 22 May 2012 and in Supplement Figure B.3 for HG for 16 March 2012. In regions of fast flow (u^{obs} > 1 km yr^{-1}), all four models showed a weak bed ($\tau_b < 50$ kPa) with isolated sticky spots ($\tau_b > 300$ kPa). The basal shear stress in the weak-bedded regions was significantly smaller than the driving stress ($\tau_d \approx 300$ kPa). At KG, the area where $\tau_b < 10$ kPa comprised 30% of the area of fast flow in FS-CT, 20% of the area in FS-MT and SSA-CT, and 10% of the area in SSA-MT. At both glaciers, the sticky spots had a larger spatial extent and lower basal shear stress in FS-MT ($\tau_b \approx$ 300–400 kPa) compared to the other models ($\tau_b > 400$ kPa). In regions of slow flow (u^{obs} < 1 km yr^{-1}), the basal shear stress ($\tau_b \approx$ 150–200 kPa) was comparable to or slightly greater than the driving stress ($\tau_d \approx$ 150–200 kPa) for all models.

While the inferred basal shear stresses were qualitatively similar for all four models, the magnitudes of the inferred basal friction coefficients varied significantly among the models as indicated by their effect on modeled flow. Figure 3.3b-3.3e shows the residual between the modeled and observed velocities for KG for diagnostic simulations with different combinations of forward model and inferred basal friction coefficient. For each diagnostic simulation, we reported the mean absolute residual (MAR) for the region where $u^{obs} > 1$ km yr^{-1} over the observational period. We excluded comparison in regions where $u^{obs} < 1$ km yr^{-1} because the models did not adequately fit slower velocities (Figure 3.2c and Supplement Figure B.2c). As expected, MAR was low (< 3%) for diagnostic simulations that used the same forward model as the model used to infer the basal friction coefficient (Figure 3.3b1, 3.3c2, 3.3d3, and 3.3e4). MAR values were also low (~ 5%) for different combinations of SSA-CT and SSA-MT (Figure 3.3d4 and 3.3e3), because the magnitudes of the inferred basal friction coefficients were similar for the two models. The largest MAR values (> 20%) involved FS-MT as the forward model in the diagnostic simulation (Figure 3.3b2, 3.3d2, and 3.3e2) or in the inversion (Figure 3.3c1, 3.3c3, and 3.3c4). The results for HG, which were qualitatively similar to those for KG, are shown in Supplement Figure B.3b-B.3e.

Figure 3.4 shows the ratio of basal to surface velocity at KG and HG for FS-CT and FS-MT. For the region at KG where $u^{obs} > 1$ km yr^{-1}, basal sliding accounted for 73–82% of the surface motion over the observational period according to FS-CT and 53–66% of the surface motion according to FS-MT. At HG, basal sliding accounted for 76–81% of the surface motion according to FS-CT and 64–69% according to FS-MT. By construction, basal sliding accounted for 100% of the surface motion in SSA-CT and SSA-MT [MacAyeal, 1989].

3.4.3 Temporal variations in the inferred basal shear stress

Given that the snapshot inversions poorly fit regions of slow flow ($u^{obs} < 1$ km yr^{-1}; Figure 3.2c and Supplement Figure B.2c), we only considered the temporal evolution of the average basal shear stress in regions of fast flow ($u^{obs} > 1$ km yr^{-1}). We divided the regions of fast flow into an “upper” and “lower” glacier based on their observed surface velocities: the lower glacier covered the region where $u^{obs} > 4$ km yr^{-1} for all observations from 2001 to 2016 (dashed white curves in Figure 3.1), and the upper glacier covered the region where 1 km yr$^{-1} < u^{obs} < 4$ km yr^{-1} (dashed white and black curves in Figure 3.1). The average basal shear stress calculated for each region might be influenced by the boundary near the mesh edges. To determine the impact of boundary effects on the inferred temporal evolution of the basal shear stress, we experimented with excluding nodes within a given distance of the mesh boundary from our average values for each region; the results presented below, which used all nodes, were qualitatively similar to those obtained when we excluded nodes within 500 and 1000 m of the mesh boundary from our calculations.

Figure 3.5 shows the average surface velocity, ice thickness, driving stress, and basal shear stress for the upper and lower glacier at KG from 2001 to 2016. On average, τ_b supported 40–61% of τ_d over the lower glacier (Figure 3.5c) and 70–85% of τ_d over the upper glacier (Figure 3.5d), with the rest of τ_d supported by the lateral margins or slower-moving regions upstream. Between August 2003 and June 2005, the lower glacier sped up by 4 km yr^{-1} (Figure 3.5a) and thinned by 100 m (Figure 3.5b) during a period of terminus retreat [*Howat et al.*, 2007; *Joughin et al.*, 2008b]. Coincident with this speedup, τ_d increased by 50 kPa over the lower glacier, while τ_b decreased by 50–140 kPa. On the upper glacier, the increase in τ_b (10–20 kPa) accounted for roughly half of the increase in τ_d (30 kPa) during the speedup. By July 2007, the lower glacier had slowed by 2 km yr^{-1} and thinned by an additional 30 m. Coincident with this slowdown, τ_d decreased by 30 kPa for the lower glacier and by 20 kPa for the upper glacier. While τ_b remained low across the lower glacier during the slowdown, it subsequently increased by 10–60 kPa between July 2007 and August 2009 despite continued thinning. After August 2009, τ_b varied by < 10–40 kPa for the lower glacier and by < 10 kPa for the upper glacier.

Figure 3.6 shows terminus position [*Kehrl et al.*, 2017], surface velocity, basal velocity, driving stress, and basal shear stress averaged over the entire region of fast flow (u^{obs} > 1 km yr^{-}

^{1}) at KG from 2011 to 2015. Previous studies [*Sundal et al.*, 2013; *Kehrl et al.*, 2017] found two distinct periods of seasonal speedup at KG: (1) a mid-summer speedup of ~200 m yr^{-1} associated with surface-melt-induced basal lubrication and (2) a mid-winter speedup of varying magnitude associated with the seasonal retreat of KG's floating ice tongue (Figure 3.6a and 3.6c). Coincident with the mid-summer speedups from 2011 to 2015, the snapshot inversions indicated an increase in basal sliding that accounted for the observed speedup (Figure 3.6d) and a decrease in τ_b of 5–8 kPa over the region of fast flow (Figure 3.6e). Peak basal shear stresses occurred in the late summer or early fall. Seasonal changes in τ_b did not coincide with seasonal changes in τ_d.

Figure 3.7 shows the average surface velocity, ice thickness, driving stress, and basal shear stress for the upper and lower glacier at HG from 2004 to 2015. On average, τ_b supported 31–51% of τ_d over the lower glacier (Figure 3.7c) and 68–85% of τ_d over the upper glacier (Figure 3.7d), with the rest of τ_d supported by the lateral margins or slower-moving regions upstream. Between August 2004 and August 2005, the lower glacier sped up by 1 km yr^{-1} (Figure 3.7a) and thinned by 40 m (Figure 3.7b) during a period of terminus retreat [*Howat et al.*, 2005]. On the lower glacier, τ_d decreased by 5 kPa and τ_b decreased by 10–30 kPa during the speedup (Figure 3.7c). On the upper glacier, τ_d increased by 10 kPa; the four models indicate that τ_b may have increased (SSA-CT and SSA-MT) or decreased (FS-CT and FS-MT) during this time (Figure 3.7d). The lower glacier slowed by 1.9 km yr^{-1} and thickened by 10 m from August 2005 to August 2006 as its terminus re-advanced [*Howat et al.*, 2007; *Joughin et al.*, 2008b]. During the slowdown, τ_b increased by 10–20 kPa over the lower glacier. Since August 2006, τ_b has varied by < 20 kPa on the lower glacier and by < 10 kPa on the upper glacier.

Figure 3.8 shows terminus position [*Kehrl et al.*, 2017], surface velocity, basal velocity, driving stress, and basal shear stress averaged over the entire region of fast flow (u^{obs} > 1 km yr^{-}

^{1}) at HG from 2011 to 2015. Previous work [*Kehrl et al.*, 2017] showed that HG seasonally sped up and dynamically thinned during summers with significant terminus retreat from 2011 to 2015 (Figure 3.8a–3.8c). Despite significant retreat, speedup, and thinning during summer 2013 compared to the other summers, τ_b was similar to values calculated during other summers (Figure 3.8e). In contrast to KG, it is less clear whether seasonal variations in τ_b occurred at HG.

3.4.4 Relationship between the basal velocity and basal shear stress

Figure 3.9 shows the relationship between u_b and τ_b for the lower glacier, upper glacier, and entire region of fast flow at KG and HG. On lower KG, we find an inverse relationship between u_b and τ_b for all models, in which faster u_b is associated with smaller τ_b (Figure 3.9a). The relationship between u_b and τ_b is less clear for lower HG (Figure 3.9d); while the results generally support an inverse relationship, the slopes for SSA-CT and SSA-MT are not statistically different from zero according to a Wald Test with a significance level of 0.05. On upper KG and upper HG, our results are generally inconsistent with an inverse relationship; SSA-CT and SSA-MT suggest a positive relationship, while the relationships for FS-CT and FS-MT are even less clear. Supplement Tables S3 and S4 provide the Pearson correlation coefficients between u_b and τ_b for each individual region and forward model.

3.5 Discussion

In the following sections, we discuss spatial and temporal variations in the basal shear stress at HG and KG and then use these patterns to help constrain the form of the basal sliding law.

3.5.1 Spatial variations in the basal shear stress

Consistent with previous studies [*Joughin et al.*, 2012; *Habermann et al.*, 2013; *Shapero et al.*, 2016], our snapshot inversions indicate a predominantly weak bed that supports little of the driving stress in regions of fast flow at HG and KG (Figure 3.3 and Figure B.3). Embedded within the weak-bedded region are sticky spots where the bed fully supports the local driving stress and resists basal sliding. Altogether, the strong- and weak-bedded regions support 60-80% of the local driving stress in the region of fast flow, with the rest of the driving stress supported by the lateral margins or coupling to slower-moving areas upstream. The presence of a weak bed interspersed with sticky spots is a consistent result across all forward models; the spatial pattern of strong- and weak-bedded regions, however, differs among the models (Figure 3.3 and Figure B.3), indicating that care should be taken in interpreting small scale variations in the basal shear stress on the order of a few ice thicknesses. *Shapero et al.* [2016] found a more extensive weak bed under regions of fast flow at HG and KG than we found in this study, likely because they assumed colder ice and a lower enhancement factor. Out of the four forward models tested in this study, FS-MT produced the least extensive weak bed under regions of fast flow because internal deformation accounted for a larger proportion of the observed surface velocity (Figure 3.4). In FS-MT, internal deformation accounted for roughly one-third of the observed surface velocity in regions of fast flow, similar to values obtained from borehole tilt measurements at Jakobshavn Isbrae [*Lüthi et al.*, 2002] and Store Glacier [*Doyle et al.*, 2018] in West Greenland. Consequently, the implications of using a model based on the SSA, which neglects internal deformation, need to be considered when applied to Greenland tidewater glaciers.

Despite differences in model physics, the SSA and FS models fit the observed surface velocities similarly well (Figure 3.2). In solving the inverse problem, the inferred basal friction coefficient must compensate for the chosen model physics. Consequently, using a basal friction coefficient inferred from one model in a simulation with a different forward model causes the model to perform poorly when compared to observations and is therefore inadvisable (Figure 3.2).

Furthermore, the similarity in data-model misfit for all models suggests that data-model misfit is likely a poor metric for choosing an optimal model and that field-based constraints should be considered. Given our poor understanding of ice rheology at KG and HG, we do not choose a single model and instead focus our attention on temporal variations in the basal shear stress that are consistent across all models.

3.5.2 Interannual variations in the basal shear stress

In the early 2000s, many Greenland tidewater glaciers retreated, sped up, and thinned [*Rignot and Kanagaratnam*, 2006; *Moon and Joughin*, 2008; *Moon et al.*, 2012]. While very few studies have investigated changes in basal conditions during this time, previous studies at Jakobshavn indicate that retreat, speedup, and thinning coincided with a drop in the basal shear stress across the lower glacier [*Joughin et al.*, 2012; *Habermann et al.*, 2013]. Our results also suggest a decrease in the basal shear stress across lower HG and KG as the glaciers retreated, sped up, and thinned from 2003 to 2005 (Figure 3.5 and Figure 3.7). On upper KG and HG, the basal shear stress remained relatively constant or increased slightly. These results imply that the bed did not locally support changes in the stress balance associated with terminus retreat. Instead, changes in the stress balance were supported by enhanced basal resistance further upstream or along the lateral shear margins, allowing the speedups to propagate farther inland [*Joughin et al.*, 2012; *Bondzio et al.*, 2017].

3.5.3 Seasonal variations in the basal shear stress

Glacier velocity varies seasonally at many Greenland tidewater glaciers in response to seasonal changes in terminus position and surface-melt-induced basal lubrication [*Howat et al.*, 2010; *Moon et al.*, 2014]. At HG, seasonal speedups and dynamic thinning occurred in the late summer and appeared to be caused by seasonal variations in terminus position [*Kehrl et al.*, 2017]. While *Bevan et al.* [2015] suggested that the seasonal speedups and dynamic thinning might be caused by surface-melt-induced basal lubrication, surface melt has been shown to cause only small speedups at HG [*Andersen et al.*, 2010]. At KG, by contrast, seasonal speedups occurred in the mid-summer and mid-winter; the mid-summer speedup appeared to be related to changes in basal lubrication [*Sundal et al.*, 2011], while the mid-winter speedup was likely caused by changes in terminus position [*Kehrl et al.*, 2017]. If seasonal speedups at HG and KG are caused by changes in basal lubrication, then we might expect the speedups to coincide with a decrease in the basal shear stress. The basal shear stress should then increase over the summer as the effective pressure increases due to the development of a more efficient subglacial drainage system. *Vallot et al.* [2017] found seasonal variations in the inferred basal shear stress at Kronebreen, Svalbard, that likely reflected the development of a more efficient subglacial drainage system.

Our limited inversions make it difficult to determine the exact timing and magnitude of seasonal variations in the basal shear stress at HG and KG (Figure 3.6 and Figure 3.8). However, the basal shear stress at KG generally reached a minimum around the time of the mid-summer speedup and then increased over the summer, potentially indicating the development of a more efficient subglacial drainage system. At HG, we find no consistent seasonal pattern in the basal shear stress. Furthermore, when HG rapidly retreated, sped up, and thinned during summer 2013, the basal shear stress remained similar to values calculated in other summers, suggesting that the speedup was not associated with changes in basal lubrication and instead driven by changes in terminus position [*Kehrl et al.*, 2017]. Consequently, our results support previous studies, which have shown that KG may be more sensitive to surface-melt-induced basal lubrication than HG [*Nettles et al.*, 2008; *Andersen et al.*, 2010; *Sundal et al.*, 2013; *Kehrl et al.*, 2017].

3.5.4 Basal sliding law

The dynamics of Greenland tidewater glaciers are highly sensitive to the choice of basal sliding law, with nonlinear sliding laws allowing changes at the ice-ocean boundary to propagate faster and farther inland [*Price et al.*, 2008; *Brondex et al.*, 2017]. The form of the basal sliding under Greenland tidewater glaciers is still debated, and several basal sliding laws have been proposed [*Habermann et al.*, 2013; *Shapero et al.*, 2016; *Stearns and van der Veen*, 2018]. In the following section, we discuss the applicability of the proposed sliding laws to HG, KG, and other Greenland tidewater glaciers.

A Weertman basal sliding law is frequently used in numerical models of Greenland tidewater glaciers due to its simplicity [e.g., *Joughin et al.*, 2012; *Nick et al.*, 2009]. Yet our snapshot inversions, along with those from *Habermann et al.* [2013], indicate that a Weertman basal sliding law is likely unsuitable for many Greenland tidewater glaciers. A Weertman sliding law implies that the basal shear stress should increase with the basal velocity (Eq. (3.1)). While our snapshot inversions indicate that there may be a positive correlation between the basal shear stress and basal velocity for upper KG and HG, we find a negative correlation for lower KG and HG (Figure 3.9), in contrast to the results expected for a Weertman sliding law. Furthermore, a Weertman sliding law allows arbitrarily high basal shear stresses and is therefore unphysical, because it does not satisfy an upper bound on the basal shear stress given by the bed geometry and effective pressure [*Iken*, 1981]. The existence of this upper bound has been shown both numerically [*Schoof*, 2005; *Gagliardini et al.*, 2007] and experimentally [*Zoet and Iverson*, 2015, 2016]. We therefore suggest that a Weertman basal sliding law, while simple to implement, may be unsuitable for Greenland tidewater glaciers.

Seismic evidence [*Dow et al.*, 2013; *Walter et al.*, 2014; *Hofstede et al.*, 2018] has shown that several Greenland tidewater glaciers are underlain by sediment rather than hard bedrock, suggesting that a soft-bedded basal sliding law may be more appropriate. Inferred basal shear stresses are < 10 kPa for large regions of HG, KG, and Jakobshavn (Figure 3.3 and Figure B.3) [*Shapero et al.*, 2016]. These values are similar to basal shear stresses inferred for the Siple Coast Ice Streams, East Antarctica [*Joughin et al.*, 2004a], where deformable sediment facilitates fast flow [*Alley et al.*, 1986]. At low effective pressures, sediment is often assumed to behave as a Mohr-Coulomb plastic material with a basal yield strength [*Tulaczyk et al.*, 2000]. *Habermann et al.* [2013] suggested that the temporal evolution of the basal shear stress at Jakobshavn from 1985 to 2008 was generally consistent with a Mohr-Coulomb parameterization, where glacier thinning reduced the effective pressure and thereby lowered the basal yield strength. In calculating thinning-induced changes in the effective pressure, *Habermann et al.* [2013] assumed that the subglacial water pressure remained fixed due to its connection to the ocean. Our snapshot inversions from 2003 to 2005 also show a decrease in the basal shear stress across lower HG and KG that could be consistent with thinning-induced changes in the effective pressure and a Mohr-Coulomb parameterization (Figure 3.5). However, despite continued thinning across lower KG from 2007 to 2009, the basal shear stress increased, rather than decreased (Figure 3.5). Seasonal dynamic thinning at KG and HG also did not coincide with a seasonal decrease in the basal shear stress as might be expected for a Mohr-Coulomb parameterization (Figure 3.6 and Figure 3.8). Together, these results suggest that a Mohr-Coulomb parameterization with fixed subglacial water pressure may be inappropriate for HG and KG. While many studies [e.g., *Habermann et al.*, 2013; *Joughin et al.*, 2012] assume a fixed subglacial water pressure when calculating thinning-induced changes in the effective pressure, changes in ice thickness and slope affect the hydrologic potential driving water flow. Consequently, feedbacks between subglacial water pressure and ice thickness likely exist [*Hoffman and Price*, 2014], perhaps explaining the inconsistent relationship between the basal shear stress and glacier thinning at HG and KG. Alternatively, even if regions of HG and KG are underlain by deformable sediment, the basal dynamics may not follow a Mohr-Coulomb parameterization.

While it is difficult to tease out the relationship between the basal shear stress and basal velocity from our snapshot inversions and thereby constrain the form of the basal sliding law (Figure 3.9), our results generally support an inverse relationship between these terms under lower KG and HG. On upper KG and HG, the relationship between the basal shear stress and basal velocity is less clear. *Stearns and van der Veen* [2018] found no relationship between the basal shear stress and basal velocity at 140 Greenland tidewater glaciers; rather they argued for a basal sliding law in which the basal velocity depends on only the effective pressure and thereby the height above flotation. Their conclusions, however, were based on relationships in space, rather than in time. We find no temporal relationship between variations in ice thickness and basal velocity at HG and KG (Figure 3.5 and Figure 3.7), and consequently, our results do not support a basal sliding law that depends on only effective pressure.

Instead, we suggest that our snapshot inversions are more consistent with a spatially variable bed composed of both hard- and soft-bedded regions (Figure 3.3 and Figure B.3). If that is the case, then different regions may follow different basal sliding laws, perhaps explaining the varying relationship between the basal shear stress and basal velocity for the upper and lower glacier at KG and HG (Figure 3.9). *Hofstede et al.* [2018] found patches of consolidated and unconsolidated sediment that varied on a spatial scale of ~100 m in seismic profiles at Store Glacier. While inversions cannot identify variations in basal conditions at such small scales

[*Gudmundsson*, 2003], there is a strong correlation between the inferred basal shear stress and the basal acoustic impedance in seismic profiles averaged over larger distances [*Kyrke-Smith et al.*, 2017]. Consequently, we suggest that the relatively robust spatial pattern in the basal shear stress at HG and KG for all forward models likely implies a mixture of soft- and hard-bedded regions, which may follow different basal sliding laws. *Vallot et al.* [2017] found that the best-fit sliding law exponent in Eq. (3.1) varied spatially and temporally at Kronebreen, perhaps implying a spatially variable basal sliding law. Even if the basal sliding law varies spatially, it may still be possible to reproduce recent changes in Greenland tidewater glaciers using an ice-flow model that assumes a spatially constant basal sliding law [*Joughin et al.*, 2012; *Bondzio et al.*, 2017], because the hard-bedded regions, which support more of the driving stress, likely dominate the overall sliding behavior. However, our results suggest that the potential implications of a spatially variable basal sliding law should be considered.

3.6 Conclusions

Our results show seasonal and interannual variations in basal conditions under Helheim and Kangerlussuaq glaciers from 2001 to 2016. In all snapshot inversions, we find a weak bed interspersed with sticky spots under regions of fast flow. During large speedups, the basal shear stress remained constant or decreased across lower Helheim and Kangerlussuaq, implying that variations in the stress balance near the terminus were primarily supported outside of the regions of fast flow. Seasonal variations in the basal shear stress at Kangerlussuaq coincided with changes in surface runoff, likely reflecting the development of a more efficient subglacial drainage system. It is less clear if seasonal variations in the basal shear stress occurred at Helheim. Together, our results suggest that Helheim and Kangerlussuaq are likely underlain by both soft- and hard-bedded regions which may follow different basal sliding laws.

3.7 Data availability

Surface-velocity measurements from 2001 to 2016 are available from the National Snow and Ice Data Center (nsidc.org.data/measures/gimp). Surface-elevation measurements are from *Howat et al*. [2007] and *Kehrl et al.* [2017]. Snapshot inversions are available from the authors upon request. Code is available at https://github.com/kehrl/big3.

3.8 Acknowledgments

L. Kehrl was supported by the Department of Defense (DoD) through the National Defense Science & Engineering Graduate Fellowship (NDSEG) Program and by the NASA MEaSUREs Program (NNX13AI21A), I. Joughin was also supported by the NASA MEaSUREs program (NNX13AI21A), and B.E. Smith was supported by NASA grant NNX13AP96G. Numerical simulations were run through the NASA High-End Computing (HEC) Program through the NASA Advanced Supercomputing (NAS) Division at Ames Research Center. We thank Brice Noël and Michiel van den Broeke (Utrecht University) for providing RACMO 2.3 data.

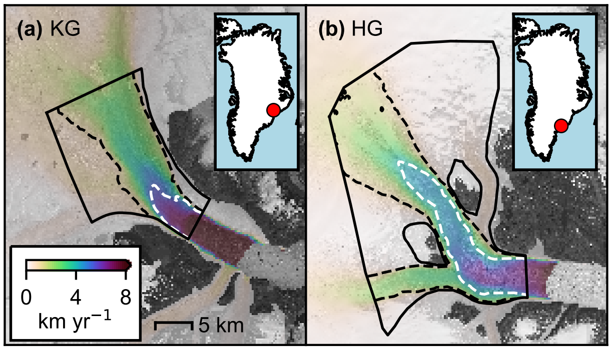

Figure 3.1. Glacier velocity at (a) Kangerlussuaq Glacier (KG) and (b) Helheim Glacier (HG) in July 2014. Black curves show model extent, dashed black curves highlight the region where observed surface velocities $u^{obs} > 1$ km yr^{-1} for all observations, and white dashed curves highlight the region where $u^{obs} > 4$ km yr^{-1} for all observations. Red circles on inset maps show the location of KG and HG in Greenland. Background images are from Landsat 8.

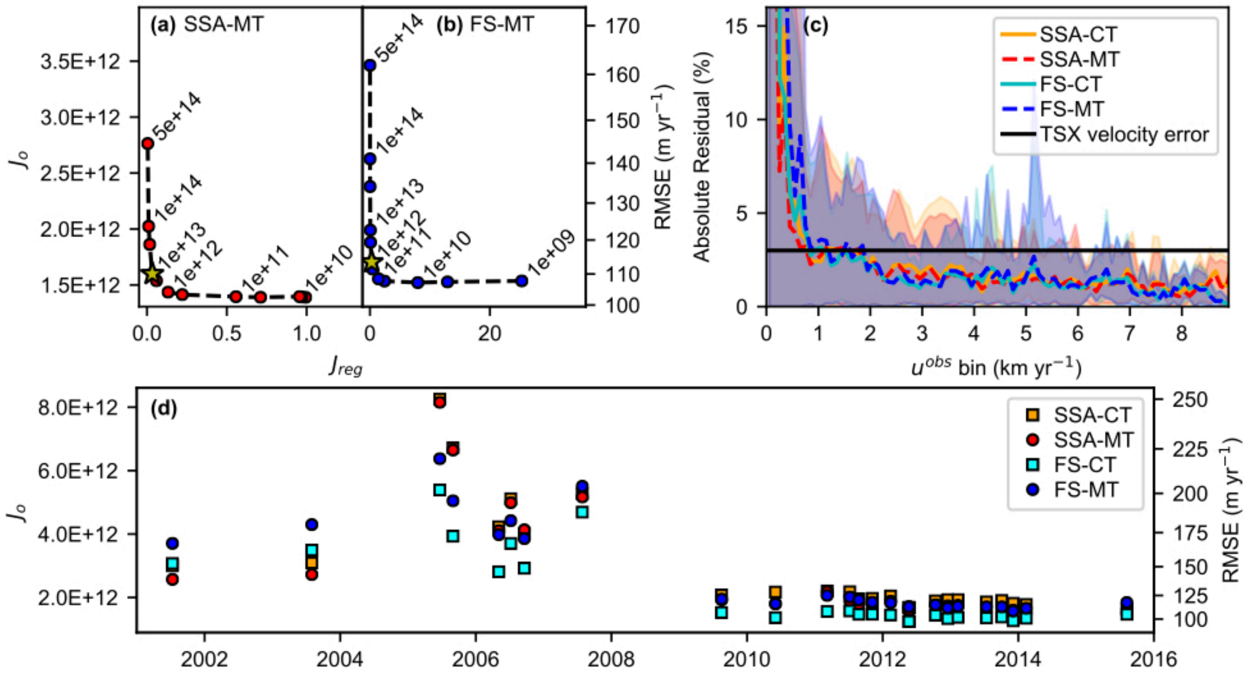

Figure 3.2. Data-model misfit for KG. (a,b) L-curves show model norm J_{reg} versus data-model misfit J_o for different values of the regularization parameter λ for (a) SSA-MT and (b) FS-MT. Yellow stars indicate the chosen regularization parameter for SSA-MT and SSA-CT ($\lambda = 1e13$) and for FS-MT and FS-CT ($\lambda = 1e12$). (c) Mean absolute residual between modeled and observed velocities binned by velocity u^{obs} every 100 m yr^{-1} for SSA-CT (orange), SSA-MT (red), FS-CT (cyan), and FS-MT (blue). Shaded bars show the 90th percentile range. Mean absolute residuals are less than the expected error for the TSX velocity estimates (black line) for u^{obs} > 1 km yr^{-1}. Inversions in (a–c) are constrained by observations from 22 May 2012. (d) Data-model misfit J_o and root-mean square error (RMSE) for all snapshot inversions from 2001 to 2016.

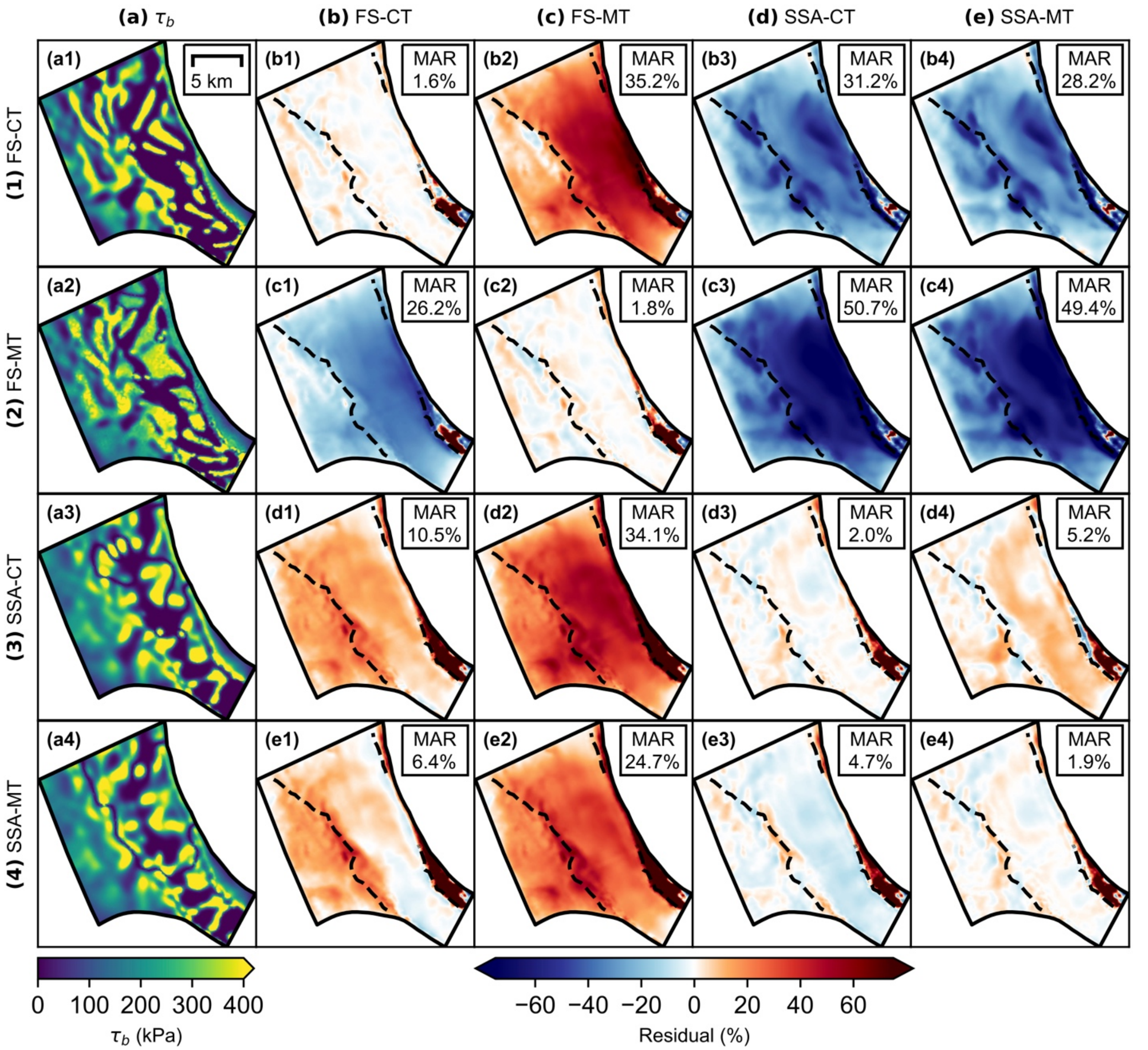

Figure 3.3. (a) Inferred basal shear stress τ_b and (b-e) residual between modeled and measured velocities for KG for 22 May 2012. Rows use a single basal friction coefficient field inferred from (1) FS-CT, (2) FS-MT, (3) SSA-CT, and (4) SSA-MT. Columns (b-e) indicate the forward model used for each diagnostic simulation: (b) FS-CT, (c) FS-MT, (d) SSA-CT, and (e) SSA-MT. For example, subpanel (c1) shows a diagnostic simulation using the FS-CT forward model with an inferred basal friction coefficient from FS-MT. The mean absolute residual (MAR) is calculated for the region where $u^{obs} > 1$ km yr^{-1}, as indicated by the dashed curves. Low MAR values are

expected for subpanels (b1), (c2), (d3), and (e4), which used the same forward model as the model used to infer the basal friction coefficient.

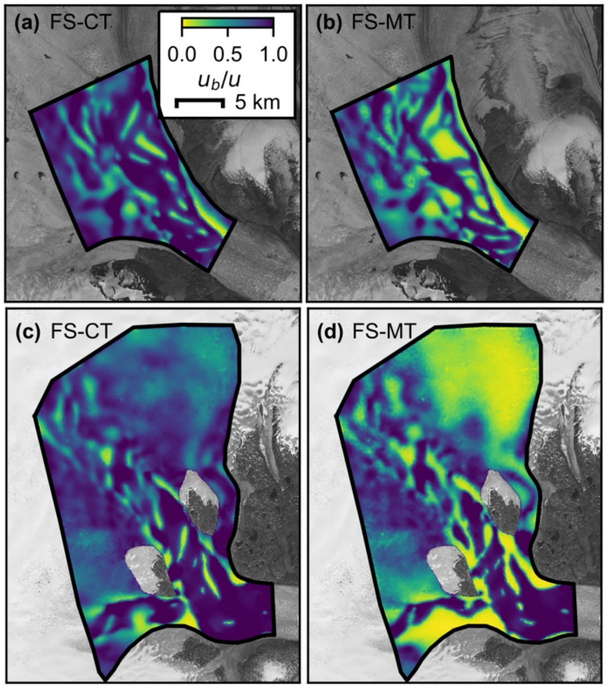

Figure 3.4. Ratio of the basal velocity u_b to the surface velocity u at KG for (a) FS-CT and (b) FS-MT on 22 May 2012 and at HG for (c) FS-CT and (d) FS-MT on 16 March 2012.

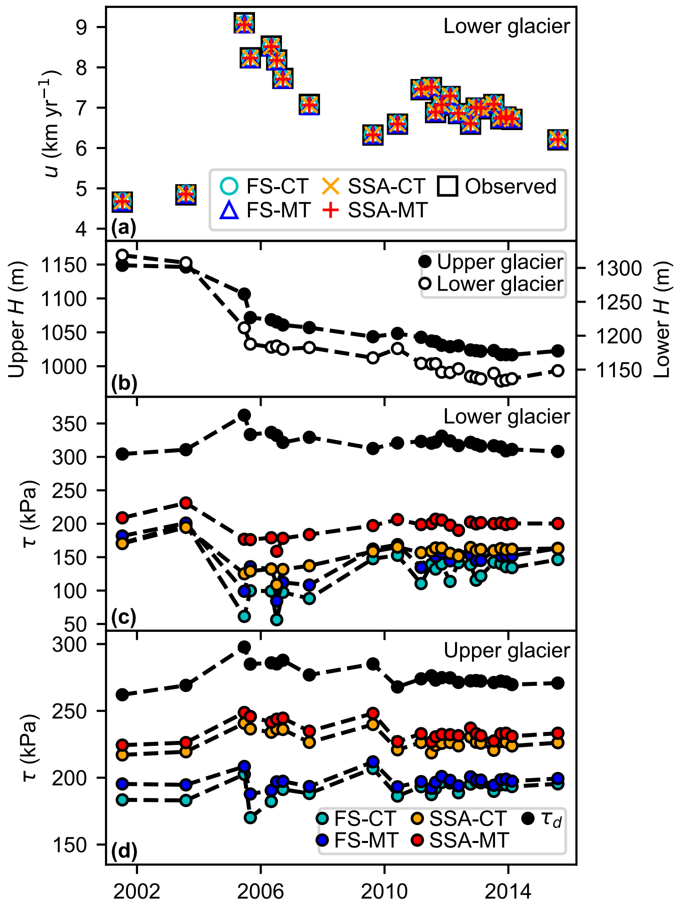

Figure 3.5. Average surface velocity and basal shear stress at KG from 2001 to 2016 for FS-CT (cyan), FS-MT (blue), SSA-CT (orange), and SSA-MT (red). (a) Average surface velocity u for the lower glacier (Figure 3.1a). White boxes indicate the observed velocity and colored markers indicate the modeled velocity from the snapshot inversions. (b) Average ice thickness H for the upper glacier (left; black circles) and for the lower glacier (right; white circles). (c) Average basal shear stress τ_b (colored circles) and driving stress τ_d (black circles) for the lower glacier. (d) Average basal shear stress and driving stress for the upper glacier.

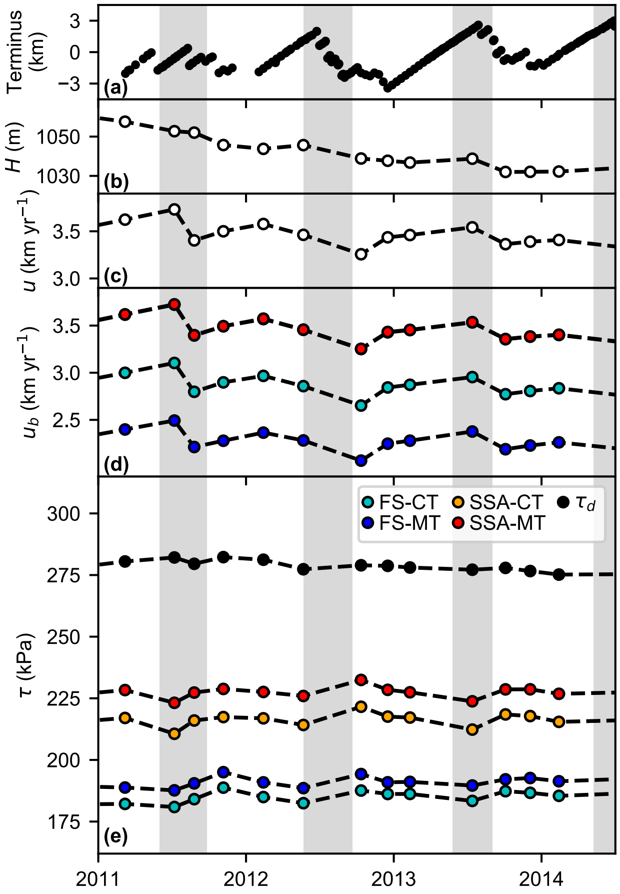

Figure 3.6. Average velocity and basal shear stress for KG for the region where $u^{obs} > 1$ km yr^{-1} from 2011 to 2015 for FS-CT (cyan), FS-MT (blue), SSA-CT (orange), and SSA-MT (red). (a) Average terminus position from *Kehrl et al.* [2017], with a positive change indicating advance, (b) average ice thickness H, (c) average surface velocity u, (d) average basal velocity u_b, and (e) average driving stress τ_d and basal shear stress τ_b. Grey vertical bars indicate periods of glacier surface runoff from RACMO 2.3 [*van Angelen et al.*, 2013; *Noël et al.*, 2015].

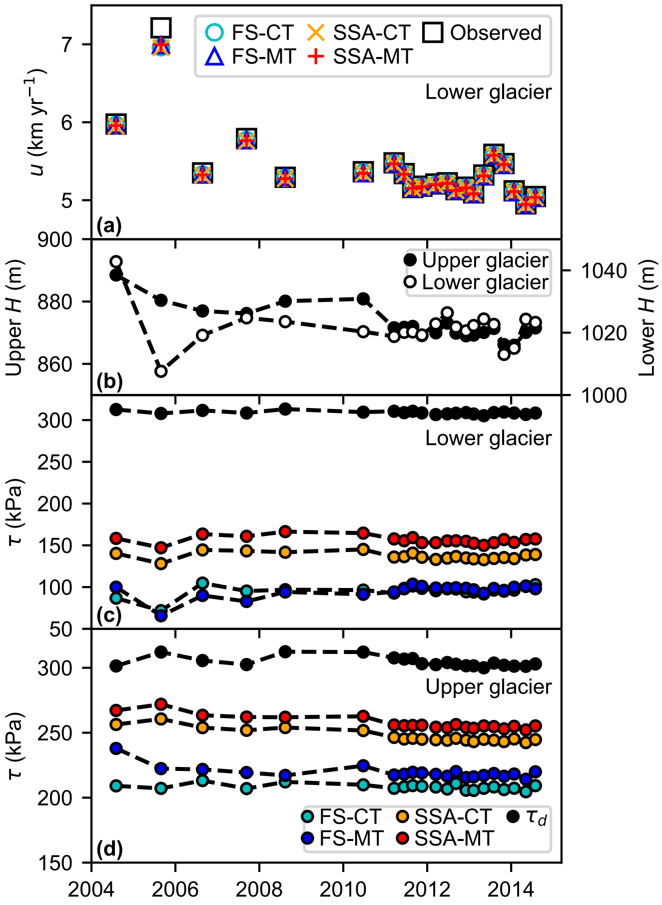

Figure 3.7. Average surface velocity and basal shear stress for the lower and upper glacier at HG from 2004 to 2015. See Figure 3.5 for a description of subpanels.

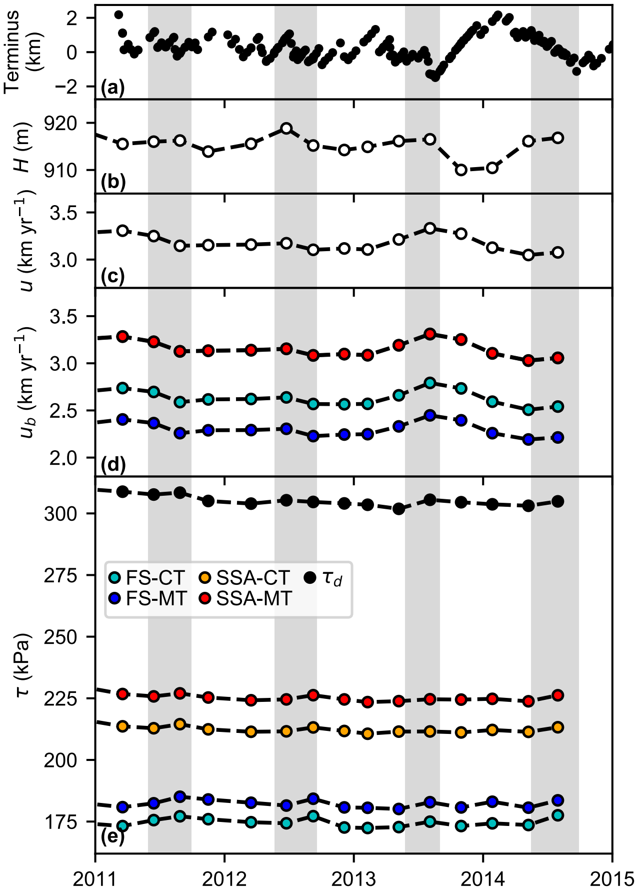

Figure 3.8. Average velocity and basal shear stress for HG for the region where $u^{obs} > 1$ km yr^{-1} from 2011 to 2015. See Figure 3.6 for a description of subpanels.

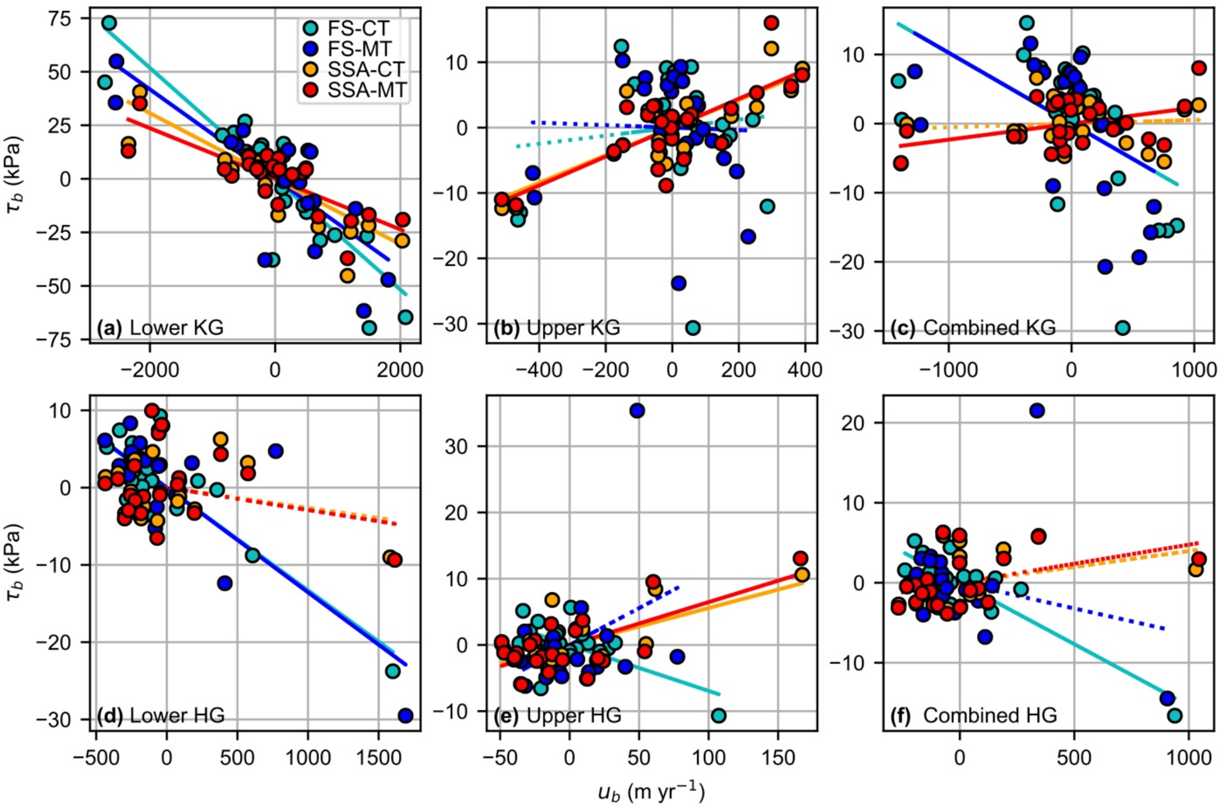

Figure 3.9. Average basal velocity u_b vs. average basal shear stress τ_b at (a, b, c) KG and (d, e, f) HG for (a, d) the lower glacier, (b, e) upper glacier, and (c, f) the entire region of fast flow. Solid (dashed) lines show best-fit lines with slopes that are (are not) significantly different from zero using a Wald Test with a significance level of 0.05. To show results for all forward models on the same scale, we have subtracted the average basal velocity and basal shear stress calculated for each model from the values shown.

Chapter 4. Evaluating the duration and continuity of potential climate records from the Allan Hills Blue Ice Area, East Antarctica

Chapter 4, in full, is a reprint of "Evaluating the duration and continuity of potential climate records from the Allan Hills Blue Ice Area, East Antarctica" authored by L. Kehrl, H. Conway, N. Holschuh, S. Campbell, A.V. Kurbatov, and N.E. Spaulding as it appears in *Geophysical Research Letters* 2018. The supplement for this paper can be found in Appendix C. The dissertation author was the primary investigator and author of this paper.

4.1 Abstract

The current ice-core record extends back 800,000 years. Geologic and glaciological evidence suggests that the Allan Hills Blue Ice Area, East Antarctica, may preserve a continuous record that extends further back in time. In this study, we use ice-penetrating radar and existing age constraints to map the internal stratigraphy and age structure of the Allan Hills Main Ice Field. The dated isochrones provide constraints for an ice-flow model to estimate the age of ice near the bed. Previous drilling in the region recovered stratigraphically disturbed sections of ice up to 2.7 million years old. Our study identifies a site ~5 km upstream which likely preserves a continuous record through Marine Isotope Stage 11 with the possibility that the record extends back one million years. Such records would provide new insight into the past climate and glacial history of the Ross Sea Sector.

4.2 *Introduction*

Ice cores currently provide detailed, continuous records of Earth's climate and atmosphere over the past 800,000 years (800 ka) [*EPICA Community Members*, 2004; *Masson-Delmotte et al.*, 2010]. Lower resolution climate records from before 800 ka have been obtained from marine sediments [*Lisiecki and Raymo*, 2005; *Clark et al.*, 2006]. Together these records show that glacial cycles transitioned from a periodicity of 41 ka to 100 ka between 1200 ka and 700 ka ago during the mid-Pleistocene transition (MPT). The causes of the MPT remain poorly understood; hypotheses include a long-term decrease in atmospheric carbon dioxide concentrations [*Berger et al.*, 1999], changes in sea-ice extent [*Tziperman and Gildor*, 2003], and the removal of regolith by glacial erosion in the Northern Hemisphere [*Clark et al.*, 2006]. Interest in the MPT has fueled the search for an ice core that spans this time interval, which could help elucidate the characteristics of the transition [*Jouzel and Masson-Delmotte*, 2010; *Fischer et al.*, 2013].

Previous studies have concluded that a continuous, million-year-old ice-core record is more likely to be preserved at a site that satisfies certain conditions: (1) it is near an ice divide, where stratigraphically disturbed ice is less likely due to slow flow [*van Liefferinge and Pattyn*, 2013]; (2) there is negligible basal melt, which removes old ice from the bed [*Fischer et al.*, 2013; *van Liefferinge and Pattyn*, 2013; *Parrenin et al.*, 2017]; and (3) there is limited basal relief, as steep basal topography tends to deform basal ice [*Fischer et al.*, 2013]. The Allan Hills Blue Ice Area, East Antarctica (Figure 4.1), is characterized by steep basal topography, seemingly disqualifying it in the search for an old ice core. Yet, stratigraphically discrete ice samples as old as 2.7±0.3 million years (Ma) have been recovered from the region (site BIT-58 in Figure 4.1a) [*Higgins et al.*, 2015; *Yan et al.*, 2017], indicating that the region could preserve a continuous, 1-Ma+ paleoclimate record.

In this study, we determine the likely duration and continuity of a potential paleoclimate record from the Allan Hills Blue Ice Area. Blue ice areas form in regions of high winds, where enhanced sublimation and wind erosion cause net ablation [*Bintanja*, 1999; *Sinisalo and Moore*, 2010]. Net ablation, combined with subglacial topographic barriers, causes the ice to flow towards the surface. These conditions produce steeply dipping englacial layers that outcrop at the surface [*Whillans and Cassidy*, 1983; *Bintanja*, 1999; *Grinsted et al.*, 2003; *Turney et al.*, 2013]. In the Allan Hills, tephra layers as old as 205 ka are exposed at the surface [*Dunbar et al.*, 1995], and meteorites with ages up to 2.2 Ma have been recovered [*Nishiizumi et al.*, 1989; *Delisle and Sievers*, 1991].

4.3 Methods

4.3.1 *Ice-penetrating radar*

Blue ice areas are typically characterized by steeply dipping englacial layers [*Bintanja*, 1999; *Grinsted et al.*, 2003], but previous studies [*Sinisalo et al.*, 2004; *Spaulding et al.*, 2013; *Winter et al.*, 2016], which used very high frequency (50-200 MHz) radar, have only detected these layers to a depth of ~100 m. We used a high frequency system, with resistively loaded dipole antennas tuned to a center frequency of 7 MHz (wavelength in ice of 24 m), to image englacial layers to a depth of ~900 m in the AH MIF (Figure 4.1b). To our knowledge, our radar profiles provide the first direct observations of deep englacial stratigraphy in a blue ice area. Radar reflections at this frequency primarily result from electrical conductivity contrasts caused by changes in acidity due to volcanic eruptions or deposition of impurities [*Fujita et al.*, 1999] and can be considered isochrones (layers of equal age). The transmitter and receiver (a digital oscilloscope) were separated by 39 m and towed in-line behind a snowmobile traveling at ~7 km/h. The receiver was triggered by the airwave from the transmitter. Each radar record consists of 512-stacked waveforms to improve the signal-to-noise ratio. The average distance between records is 2.5 m. We determine the location of each radar record using a GPS antenna (Garmin 17HVS) mounted 1.5 m behind the receiver; position uncertainties are less than 3 m. Additional data processing includes bandpass filtering and correcting for surface topography. Two-way travel time is converted to depth using wave speeds of 300 m/μs in air and 168.5 m/μs in ice.

4.3.2 *Age constraints*

We manually pick layers of local maximum power return in the radargrams and date those layers using age constraints from horizontal and vertical ice cores near site S27 [*Spaulding et al.*, 2013], which intersects Radar Track 4 (Figure 4.1). Ages from the 225 m, vertical core are linearly interpolated to 13 picked layers that intersect the core; these layers are determined to have ages of 117-243 ka [*Spaulding et al.*, 2013]. Where englacial layers intersect the surface upstream of S27, we assign ages from the horizontal core. Near-field radar effects prevent imaging within ~40 m of the surface, so we estimate the point of surface intersection by extrapolating layers using layer slopes calculated below this 40-m threshold. We then linearly interpolate ages from the horizontal ice core to these points of surface intersection, assigning ages spanning 89–108 ka to 15 layers. Figure 4.1c shows the depth-age scale for Radar Track 4. Finally, we use crossover points between Radar Track 4 and the other tracks to determine layer ages for all radar transects. Figure 4.1d shows the height of 105-ka ice above the bed for all radar transects. We estimate an age uncertainty of 7 ka for the inferred layer ages (Text C.1).

4.3.3 *Ice-flow model*

To determine the age structure near the bed, we adapt a flowline model that is based on mass conservation [*Grinsted et al.*, 2003]. We define x to be the distance along the flowline, y to be the coordinate perpendicular to the flowline, z to be the water-equivalent height above the bed, H to be the water-equivalent ice thickness, and $\tilde{z} = z/H$ to be the fractional ice thickness. The velocity components of x, y, z, and $\tilde{z}$ are u, v, w, and $\widetilde{w}$, respectively. The horizontal velocity is

$$u(\tilde{z}) = f(\tilde{z})u_s \tag{4.1a}$$

$$v(\tilde{z}) = 0 \tag{4.1b}$$

and the horizontal velocity gradient is

$$\frac{\partial u}{\partial x} = f(\tilde{z})\frac{\partial u_s}{\partial x} \tag{4.2a}$$

$$\frac{\partial v}{\partial y} = f(\tilde{z})\frac{\partial v_s}{\partial y}, \tag{4.2b}$$

where $f(\tilde{z})$ is a shape factor and the subscript s signifies the value at the surface. Following *Grinsted et al.* [2003], we use

$$f(\tilde{z}) = \frac{\tanh(k\tilde{z})}{\tanh(k)}, \tag{4.3}$$

which is similar to the shallow-ice approximation assuming no basal sliding [*Cuffey and Paterson*, 2010]. The value k determines the ice softness and thereby temperature profile used in the model. At the equilibrium line, the steady-state temperature profile is linear [*Cuffey and Paterson*, 2010]. Surface velocities are less than 0.5 m/a on both sides of the equilibrium line in the AH MIF [*Spaulding et al.*, 2012], indicating that a linear temperature profile is likely a reasonable assumption for the entire flowline [*Grinsted et al.*, 2003]. We set $k = 5$ for a linear temperature profile that decreases from -10 °C at the bed to -30 °C at the ice surface.

The model assumes that the ice thickness remains constant through time. Cosmogenic dating and erosional features indicate that the ice was roughly 100 m thicker in the AH MIF during the Last Glacial Maximum (26-19 ka) [*Atkins et al.*, 2002] but likely remained within that range over the last 1 Ma [*Yamane et al.*, 2015]. Given this assumption, volume conservation requires

$$\frac{\partial u_s}{\partial x} + \frac{\partial v_s}{\partial y} = \frac{1}{f_m}\left(\frac{\partial u_m}{\partial x} + \frac{\partial v_m}{\partial y}\right) = \frac{\dot{b}}{f_m H}, \tag{4.4}$$

where $\dot{b}$ is the surface mass balance, with subscript m indicating the mean over the ice column. From mass continuity, we also have

$$\frac{\partial u}{\partial x}+\frac{\partial v}{\partial y}+\frac{\partial w}{\partial z}=0 \tag{4.5a}$$

$$\frac{\partial w}{\partial z}=-f(\tilde{z})\left(\frac{\partial u_s}{\partial x}+\frac{\partial v_s}{\partial y}\right). \tag{4.5b}$$

Equation 4.5 can be integrated to determine the normalized vertical velocity

$$\widetilde{w}(\tilde{z}) = -\left(\frac{\partial u_s}{\partial x}+\frac{\partial v_s}{\partial y}\right)\int_0^{\tilde{z}} f(\tilde{z}')d\tilde{z}' \tag{4.6}$$

$$=\frac{\left(\frac{\partial u_s}{\partial x}+\frac{\partial v_s}{\partial y}\right)}{-k\tanh(k)}\left(\log\left(\frac{1+e^{-2k\tilde{z}}}{2}\right)+k\tilde{z}\right).$$

We combine the horizontal and vertical velocities from Equations 4.1 and 4.6 with a Lagrangian integration scheme to determine particle back trajectories and hence the age structure of the ice [*Grinsted et al.*, 2003].

While more sophisticated models provide better representations of ice-flow behavior [e.g., Elmer/Ice; *Gagliardini et al.*, 2013], these models require constraints from detailed observations that are not yet available for the AH MIF. Field observations are sparse [*Spaulding et al.*, 2012], and very little is known about the regional ice-flow history over the last 1 to 2 Ma [*Atkins et al.*, 2002; *Yamane et al.*, 2015]. The chosen model only requires surface elevation, bed elevation, surface velocity, mass balance, and ice-softness parameter (k) along a flowline.

We use Radar Track 1 as the basis for our flowline model because it extends the farthest upstream (Figure 4.1a). The model domain extends Radar Track 1 to the local ice divide (dashed line in Figure 4.1a) [*Spaulding et al.*, 2012], with the upstream geometry defined by surface and bed elevations from BedMap2 [*Fretwell et al.*, 2013]. We use ablation ($\dot{b}$) and surface velocity measurements (u_s) from four stakes installed within 500 m of the flowline from 1997 to 2010 (Figure 4.1a and Figure 4.2a) [*Spaulding et al.*, 2012]. No stake measurements exist within 10 km of the ice divide, so we assume that the velocity decreases linearly to zero at the divide. *Dadic et al.* [2015] estimated a long-term accumulation rate of 7.5 mm/a from a shallow ice core, but accumulation rates likely vary spatially and temporally [*Bintanja*, 1999; *Spaulding et al.*, 2012]. For simplicity, we assume a constant, present-day accumulation rate across the accumulation zone, $\dot{b}_o$, which we vary from 5 to 14 mm water equivalent per year (mmWE/a) in 1 mmWE/a increments to assess model sensitivity.

Surface velocity and mass balance likely changed through time. Accumulation rates have been shown to decrease by ~30-50% during glacial periods at other East Antarctica sites [*Watanabe et al.*, 2003; *Masson-Delmotte et al.*, 2010]. The change in sublimation rates during glacial periods, however, remains less clear [*Bintanja*, 1999; *Dadic et al.*, 2013]. We assume that snow accumulation rates decrease by 50% during glacial periods and that ablation rates remain constant through time. Surface velocities also likely varied due to changes in surface mass balance, ice temperature, and glacier geometry. To match the age of meteorites exposed at the surface in the Allan Hills Near Western Ice Field, *Grinsted et al.* [2003] found that present-day velocities must have decreased by 75% during glacial periods. We vary the ratio of glacial to present-day velocities, r, from 0 to 1 in 0.1 increments to assess the sensitivity of our results to this parameter. Glacial periods are determined using the MIS record from the EPICA Dome C ice core [*EPICA Community Members*, 2004].

To assess model performance for the 110 different combinations of present-day accumulation rate ($\dot{b}_o$) and the ratio of glacial to present-day velocities (r), we compare the modeled ages to the picked layer ages to determine the model misfit M

$$M(\dot{b}_o, r) = \sqrt{\frac{1}{n}\sum_{i=1}^{n}(t(i) - t_m(i))^2}, \qquad (4.7)$$

where $t(i)$ is the measured age of layer i at depth $z(i)$ and $t_m(i)$ is its modeled age. The number of layers n varies along the flowline. We calculate model misfit from $x = 0$ to $x = 19$ km to avoid biasing our results by high model misfit values in the ablation zone, where we are less interested in the depth-age scale. High model misfit values in the ablation zone do not affect the upstream model performance.

4.4 Results

Figure 4.2 shows the measured and modeled depth-age scales for Radar Track 1. We test the sensitivity of the modeled depth-age scale to the present-day accumulation rate ($\dot{b}_o$) and the ratio of glacial to present-day velocities (r). Different combinations of $\dot{b}_o$ and r produce similar model misfit values M of 8-10 ka, as shown in Figure 4.3a. An increase in $\dot{b}_o$ requires a decrease in r to match the age constraints. The modeled depth-age scale is relatively insensitive to the chosen model parameters. Figure 4.3b shows the depth-age scale for different best-fit combinations of $\dot{b}_o$ and r at $x = 16$ km (star in Figure 4.1d; 76° 44.184' S, 159° 4.004' E). At this location, 500-ka ice is 65-70 m above the bed and 1-Ma ice is 31-33 m above the bed for all best-fit model combinations. The temporal resolution of the depth-age scale at this location is ~1 ka/m at 250 ka, ~4 ka/m at 500 ka, ~23 ka/m at 750 ka, and ~38 ka/m at 1 Ma. For the rest of the basin, 500-ka ice is 55-70 m above the bed and 1-Ma ice is 25-35 m above the bed (Figure C.2).

Given modern observations of accumulation rates and surface velocities [*Spaulding et al.*, 2012; *Dadic et al.*, 2015], our results imply a significant decrease in surface velocity during glacial periods (Figure 4.3). For a present-day accumulation rate of $\dot{b}_o = 7$ mmWE/a, surface velocity must have decreased to 80% of present-day values during glacial periods ($r = 0.8$); for a present-day accumulation rate of $\dot{b}_o = 10$ mmWE/a, velocity must have decreased to 30% of present-day values ($r = 0.3$).

This decrease in surface velocity is confirmed by the near-surface internal stratigraphy, as shown in Figure 4.4. Near the surface in Layer 1, a positive thickness anomaly forms after the bedrock bump at $x = 7$ km (Figure 4.4a, c), perhaps due to enhanced flow convergence or snow accumulation. The thickness anomaly is then buried and advected downstream. By measuring how far this anomaly has moved over a given time interval, we can determine its velocity. The thickness anomaly is 12 km downstream in Layer 5, which is bound by isochrones with ages of 89 ka and 97 ka, implying a near-surface velocity of ~0.13 m/a, roughly 30% of present-day velocities over the basin [*Spaulding et al.*, 2012]. In the flowline model, if we similarly decrease surface velocities to 30% of their present-day values during glacial periods ($r = 0.3$), the model produces a similar downstream progression in layer thickness (Figure 4.4b, d).

4.5 Discussion

Ice-core drilling in blue ice areas has the potential to replicate and extend the existing ice-core record back beyond 800 ka. Low accumulation rates, thin ice cover, and slow flow promote the preservation of old ice in these regions [*Spaulding et al.*, 2012]. Together with previous modeling studies in blue ice areas [*Grinsted et al.*, 2003; *Moore et al.*, 2006], our results show that surface velocities were slower in the past, and consequently, ice older than expected from modern ice-flow observations is likely present. Blue ice areas, however, are also frequently characterized by complex flow as ice interacts with steep basal topography *[Zwinger et al.*, 2014], which can result in spatial variations in the extent of old ice (Figure 4.1d) or stratigraphically disturbed ice [*Higgins et al.*, 2015]. Hence, even with evidence of very old ice from exposed tephra layers, meteorites, and discrete ice samples [*Dunbar et al.*, 1995; *Higgins et al.*, 2015; *Yan et al.*, 2017], careful site selection is necessary to ensure the retrieval of a continuous, undisturbed ice-core record.

Our results identify a potential region for a continuous, 1-Ma record from the AH MIF accumulation zone (star in Figure 4.1d; 76° 44.184’ S, 159° 4.004’ E). While stratigraphically disturbed ice has been recovered near BIT-58 (Figure 4.1a) [*Higgins et al.*, 2015], our radargrams reveal undisturbed internal stratigraphy to at least 900-m depth in the basin 5-10 km upstream, with no evidence of discontinuities near the surface due to erosion (Figure 4.1b) [*Winter et al.*, 2016]. Our flow model predicts 1-Ma ice 25-35 m above the bed in this basin. These results indicate that it may be possible to acquire a continuous, 1-Ma ice-core record near steep basal topography, which suggests that the current criteria for selecting a 1-Ma+ ice-core site should be expanded to include these regions [*Fischer et al.*, 2013; *van Liefferinge and Pattyn*, 2013]. Significant thinning as ice flows out of this basin may help explain the stratigraphically disturbed ice near BIT-58.

The lack of radar-detected layers near the base of the ice makes it difficult to assess whether 1-Ma ice near the bed is disturbed. The oldest radar-detected englacial layer at EPICA Dome C was ~500 ka [*Winter et al.*, 2017], but the ice-core record was continuous to 800 ka [*EPICA Community Members*, 2004]. Ice retrieved within 60 m of the bed at EPICA Dome C could not be stratigraphically interpreted [*Tison et al.*, 2015]. If layers are continuous to 60 m above the bed in the AH MIF, our model predicts a continuous record through ~500 ka. Basal ice in the AH MIF is likely colder that at EPICA Dome C [*Tison et al.*, 2015]; *Higgins et al.* [2015] found no evidence that the bed had chemically or physically altered ice collected 5 m above the bed at BIT-58. At Taylor Dome, where basal conditions are more similar to those in the AH MIF, the ice-core record was continuous to 24 m above the bed [*Steig et al.*, 2000]. If layers are continuous to 24 m above the bed in the AH MIF, then a continuous, 1-Ma ice-core record may be preserved.

The temporal resolution of 1-Ma ice in an AH MIF ice core (~38 ka/m) will be less than that from other proposed 1-Ma+ sites where the ice thickness is much greater [e.g., 10 ka/m for 1.5-Ma ice near Dome C in *Parrenin et al.*, 2017]. It is difficult to evaluate whether the AH MIF record will have sufficient temporal resolution to resolve 41-ka glacial cycles at 1 Ma [*Fischer et al.*, 2013; *Bereiter et al.*, 2014]. However, the emergence of new analytic methods and measurements [e.g., *Bender et al.*, 2008; *NEEM Community Members*, 2013; *Buizert et al.*, 2014; *Higgins et al.*, 2015; *Baggenstos et al.*, 2017; *Yan et al.*, 2017] is enabling the extraction of paleoclimate records from low-resolution, stratigraphically disturbed ice. Hence, even if the basal section of the AH MIF ice core is stratigraphically disturbed, it may still be possible to untangle the paleoclimate record using these methods.

At the very least, the AH MIF should provide a continuous, high-resolution record through MIS 11. Only three ice-core records (Dome Fuji, Vostok, EPICA Dome C) currently extend through this time interval [*Petit et al.*, 1999; *EPICA Community Members*, 2004], and none of these records are located in the Ross Sea Sector. An ice core from the AH MIF could help constrain the behavior of the Ross Ice Shelf and West Antarctic Ice Sheet during the closest-known analogue for the present-day interglacial period [*Howard*, 1997; *Loutre and Berger*, 2003].

4.6 Conclusions

We combined an ice-flow model, ice-penetrating radar, and existing age constraints to assess past ice flow in the Allan Hills Main Ice Field. Using the approach outlined above, we found that surface velocities were 30% of modern-day values during the last glacial period, indicating that older ice than expected from modern field observations is likely present. Our results reveal a potential drill site for a continuous, 1-Ma ice-core record from the Allan Hills Main Ice Field, with 1-Ma ice 25-35 m above the bed. This site does not meet current criteria used in the search for 1-Ma+ ice-core sites, indicating that rugged topography should not disqualify potential ice-core sites evaluated in future studies. While 1-Ma ice at this site may be stratigraphically disturbed, the proposed drill site should provide a continuous record through at least Marine Isotope Stage 11.

4.7 Acknowledgments

We thank the US National Science Foundation (grants PLR-1443260 & -1443461) for supporting this project, and the Antarctic Support Contractor, Air National Guard, Kenn Borek Air, and UNAVCO for logistical and field support. L. Kehrl was supported by a National Defense Science & Engineering Graduate Fellowship, and N. Holschuh was supported by NASA grant NNX16AM01G. Radar data are available at the US Antarctica Program Data Center (http://www.usap-dc.org/view/dataset/601005). Stake measurements and age constraints are from *Spaulding et al.* [2012] and *Spaulding et al.* [2013]. Code for the ice-flow model is available at https://github.com/kehrl/allanhills.

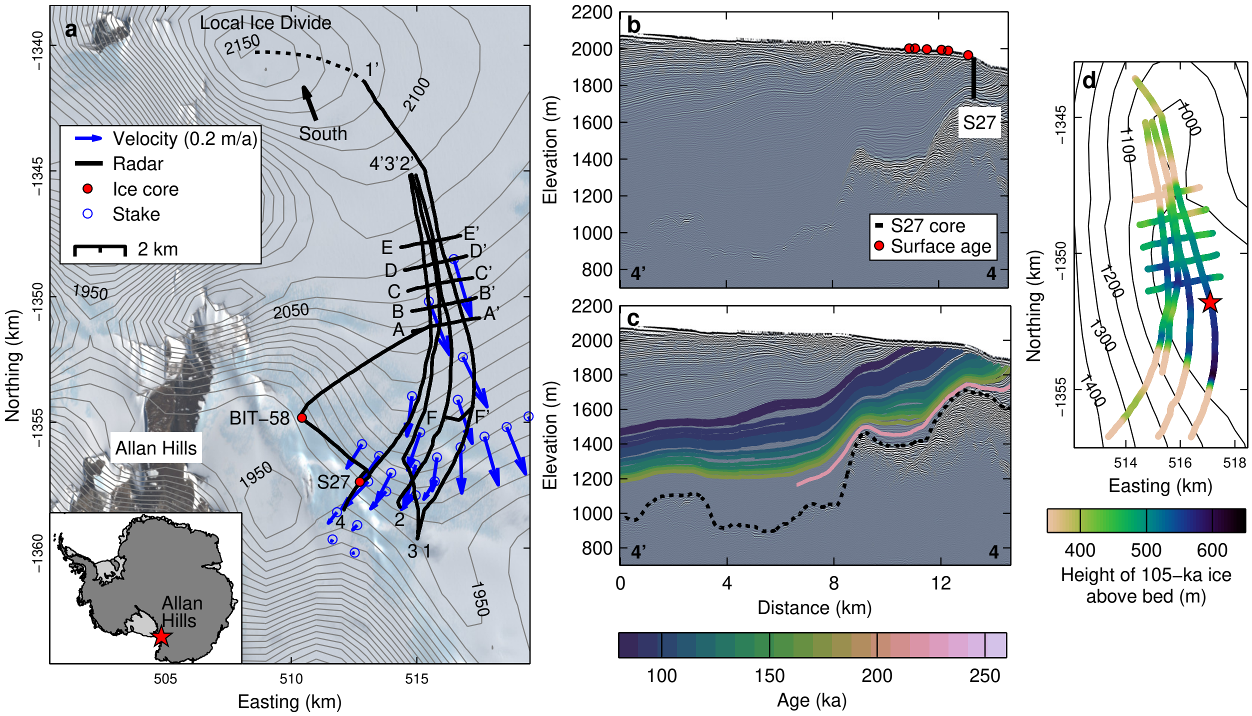

Figure 4.1. Allan Hills Main Ice Field, East Antarctica. (a) Map showing ice-penetrating radar transects (black curves), ice cores (red circles) [*Spaulding et al.*, 2013; *Higgins et al.*, 2015], stakes (blue circles) [*Spaulding et al.*, 2012], and surface velocities (blue vectors) [*Spaulding et al.*, 2012]. Black dashed curve extends Radar Track 1 to the local ice divide. Black arrow indicates South direction. Surface-elevation contours from BedMap2 (light gray lines) are shown every 10 m [*Fretwell et al.*, 2013]. Background image is a Landsat 8 image from 12 January 2016. Coordinates system is Antarctica Polar Stereographic. (b) Ice-penetrating radar data along Radar Track 4, annotated to show locations of surface ice ages (red circles) as well as ice core S27 (black line), and (c) picked layer ages (colors) and bed (black dashed curve) along Radar Track 4. (d) Height of 105-ka ice above the bed. Bed-elevation contours from BedMap2 (black lines) are shown every 100 m. Star indicates the proposed drill site shown in Figure 4.3b.

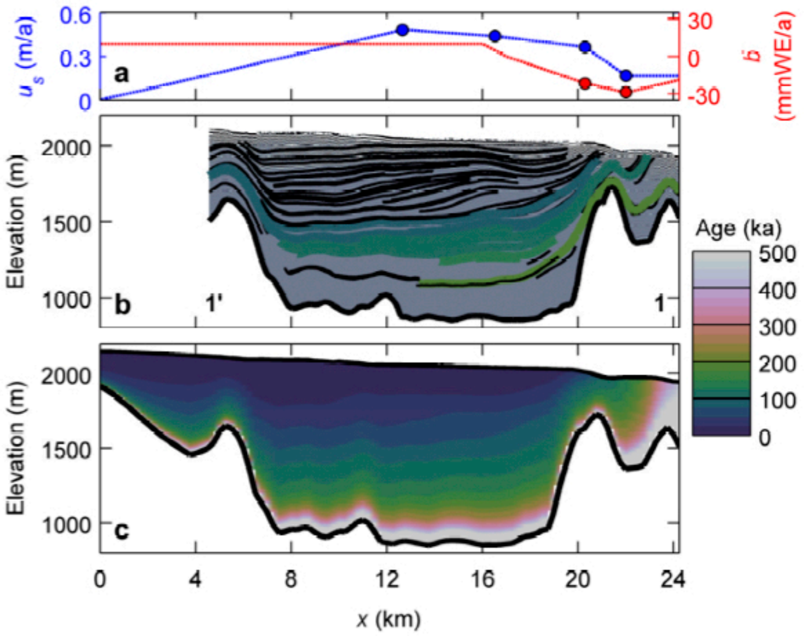

Figure 4.2. Measured and modeled depth-age scale for Radar Track 1. (a) Present-day surface velocity (u_s) and surface mass balance ($\dot{b}$) linearly interpolated from measured values (colored circles) from *Spaulding et al.* [2012], (b) measured depth-age scale, and (c) modeled depth-age scale. Black curves in (b) indicate undated, picked layers. For this model run, the present-day accumulation rate ($\dot{b}_o$) is 10 mmWE/a and surface velocities decrease to 30% of their present-day values during glacial periods ($r = 0.3$).

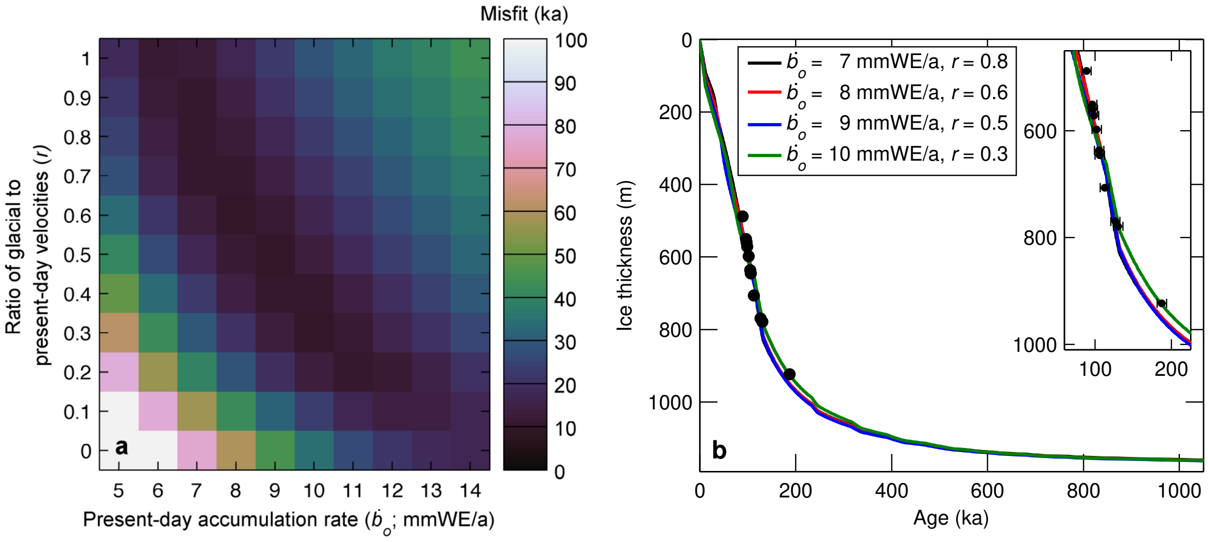

Figure 4.3. Model sensitivity to the present-day accumulation rate ($\dot{b}_o$) and the ratio of glacial to present-day velocities (r). (a) Model misfit M and (b) measured (points) and modeled (lines) depth-age scales for the proposed drill site at $x = 16$ km (red star in Figure 4.1d).

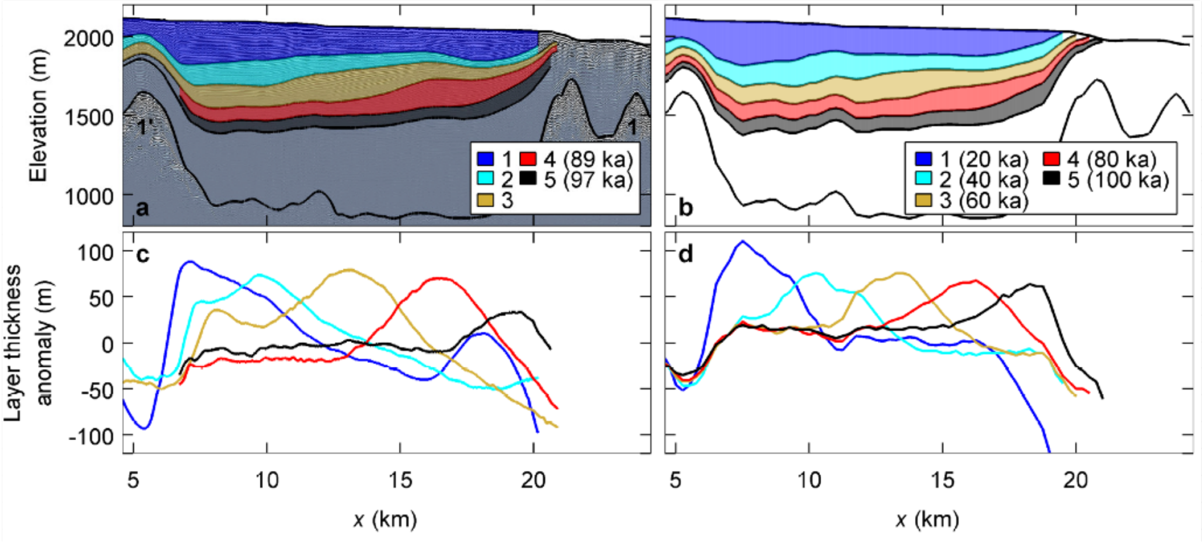

Figure 4.4. (a) Dated radiostratigraphy and (b) model-derived age structure along Radar Track 1. The thickness of discrete stratigraphic packages seen in the data (shaded in a) and reproduced by the flowline model (shaded in b) has been plotted in (c) and (d) respectively, normalized to the mean package thickness. Panels (c) and (d) highlight the apparent propagation of a thickness anomaly downstream through time, seen in the youngest layers at $x = 7$ km. The rate of anomaly propagation, deduced from dated isochrones and validated using the flowline model, implies that surface velocities were 30% of modern observed velocities during the last glacial period.

Chapter 5. Summary and future work

In the following chapter, I summarize the main findings of this dissertation and provide suggestions for future work.

5.1 Dynamics of Helheim and Kangerlussuaq Glaciers, Southeast Greenland

In Chapter 2, I showed that Helheim and Kangerlussuaq behaved differently on a seasonal and interannual timescale from 2008 to 2016. Kangerlussuaq's floating ice tongue calved large, tabular icebergs, while Helheim's lightly grounded terminus calved small, non-tabular icebergs. Furthermore, seasonal speedups and dynamic thinning at Helheim corresponded with variations in terminus position, while the relationship between glacier speed, surface elevation, and terminus position at Kangerlussuaq was less clear. Based on these observations, I suggested that the dynamics of Helheim and Kangerlussuaq differed because of differences in the spatial extent of floating ice near their termini.

Given that seasonal dynamic thinning and thickening can alter the spatial extent of floating ice near the terminus, it is possible that these variations may be important for the long-term evolution of these glaciers. For example, is a tidewater glacier more sensitive to surface melt or ice-mélange weakening during a particular time of the year? Future work should be directed towards understanding the effects of seasonal dynamic thinning and thickening on the long-term evolution of Greenland tidewater glaciers.

In Chapter 3, I showed that basal conditions at Helheim and Kangerlussuaq varied spatially and temporally from 2001 to 2016. I used four forward models to test the sensitivity of the inferred basal shear stress to the choice of forward model, showing that some patterns remained consistent across all models and others did not. All four models showed that the basal shear stress across lower Helheim and Kangerlussuaq remained relatively constant or decreased during terminus-driven speedups, suggesting that the changes in stress balance associated with terminus retreat were supported outside of the regions of fast flow. I found that the inferred relationship between the basal shear stress and basal velocity was generally inconsistent with a Weertman basal sliding law or Mohr-Coulomb parameterization and instead suggested that a spatially variable basal sliding law may be more appropriate.

Future work should be directed towards better understanding the form of the basal sliding law under Greenland tidewater glaciers. While this is easier said than done, I have a few suggestions. The results of this dissertation indicate that snapshot inversions throughout a glacier's multiyear evolution can be a useful tool in characterizing the basal sliding law. Thus far, most studies that have employed snapshot inversions [e.g., *Joughin et al.*, 2012; *Habermann et al.*, 2013] have investigated changes in basal conditions during retreat, speedup, and thinning. How do basal conditions vary during periods of advance, slowdown, and thickening? By investigating changes in basal conditions during different phases of a glacier's evolution, we may learn something new about the basal sliding law. Furthermore, the detailed timeseries of surface velocity and elevation measurements that are now available at Helheim, Kangerlussuaq, and Jakobshavn provide a unique opportunity to test which basal sliding laws are most consistent with the observational record. Prognostic simulations should not only help constrain the form of the basal sliding law but also provide insight into the potential implications of different basal sliding laws for the future evolution of these glaciers.

5.2 Dynamics of the Allan Hills Blue Ice Area, East Antarctica

In Chapter 4, I determined a potential location to drill a million-year-old ice core in the Allan Hills Blue Ice Area and showed that the englacial stratigraphy likely suggested that glacier velocity was 30% of present-day values during the last glaciation. These results were based on an analysis of ice-penetrating radar data, age constraints, and surface-velocity measurements within 10 km of the proposed drill site. The ice dynamics further upstream remain poorly understood, and consequently I had to make several assumptions about the upstream region for this analysis. Future work should be directed towards better understanding the region upstream; ice-penetrating radar data should be collected to investigate the internal stratigraphy and bed geometry, and stakes should be installed to determine surface velocities and thereby the origin of the ice in the Allan Hills. With additional data, a more physically-based ice-flow model could be used to validate the results in this dissertation.

REFERENCES

Alley, R. B., D. D. Blankenship, C. R. Bentley, and S. T. Rooney (1986), Deformation of till beneath ice stream B, West Antarctica, *Nature*, *322*(6074), 57–59, doi:10.1038/322057a0.

Alley, R. B., H. J. Horgan, I. R. Joughin, K. M. Cuffey, T. K. Dupont, B. R. Parizek, S. Anandakrishan, and J. Bassis (2008), A simple law for ice-shelf calving, *Science*, *322*, 1344.

Alley, R. B., S. Anandakrishnan, K. Christianson, H. J. Horgan, A. Muto, B. R. Parizek, D. Pollard, and R. T. Walker (2015), Oceanic Forcing of Ice-Sheet Retreat: West Antarctica and More, *Annu. Rev. Earth Planet. Sci.*, *43*(1), 207–231, doi:10.1146/annurev-earth-060614-105344.

Amundson, J. M. (2016), A mass-flux perspective of the tidewater glacier cycle, *J. Glaciol.*, *62*(231), 82–93, doi:10.1017/jog.2016.14.

Amundson, J. M., M. A. Fahnestock, M. Truffer, J. Brown, M. P. Lüthi, and R. J. Motyka (2010), Ice mélange dynamics and implications for terminus stability, Jakobshavn Isbræ, Greenland, *J. Geophys. Res.*, *115*(F1), F01005, doi:10.1029/2009JF001405.

Andersen, M. L. et al. (2010), Spatial and temporal melt variability at Helheim Glacier, East Greenland, and its effect on ice dynamics, *J. Geophys. Res. Earth Surf.*, *115*, 1–18, doi:10.1029/2010JF001760.

Andresen, C. S. et al. (2012), Rapid response of Helheim Glacier in Greenland to climate variability over the past century, *Nat. Geosci.*, *5*, 37–41, doi:10.1038/ngeo1349.

van Angelen, J. H., M. R. van den Broeke, B. Wouters, and J. T. M. Lenaerts (2013), Contemporary (1960-2012) Evolution of the Climate and Surface Mass Balance of the Greenland Ice Sheet, *Surv. Geophys.*, *35*(5), 1155–1174, doi:10.1007/s10712-013-9261-z.

Arthern, R. J., and G. H. Gudmundsson (2010), Initialization of ice-sheet forecasts viewed as an inverse Robin problem, *J. Glaciol.*, *56*(197), 527–533, doi:10.3189/002214310792447699.

Aster, R., B. Borchers, and C. Thurber (2005), *Parameter Estimation and Inverse Problems*, Academic Press, New York.

Atkins, C. B., P. J. Barrett, and S. R. Hicock (2002), Cold glaciers erode and deposit: Evidence from Allan Hills, Antarctica, *Geology*, *30*(7), 659–662, doi:10.1130/0091-7613(2002)030<0659:CGEADE>2.0.CO;2.

Baggenstos, D., T. K. Bauska, J. P. Severinghaus, J. E. Lee, H. Schaefer, C. Buizert, E. J. Brook, S. Shackleton, and V. V Petrenko (2017), Atmospheric gas records from Taylor Glacier, Antarctica, reveal ancient ice with ages spanning the entire last glacial cycle, *Clim. Past*, *13*(7), 943–958, doi:10.5194/cp-13-943-2017.

Bamber, J. L. et al. (2013), A new bed elevation dataset for Greenland, *Cryosph.*, *7*, 499–510, doi:10.5194/tc-7-499-2013.

Bassis, J. N., and S. Jacobs (2013), Diverse calving patterns linked to glacier geometry, *Nat. Geosci.*, *6*(10), 833–836, doi:10.1038/ngeo1887.

Bassis, J. N., and Y. Ma (2015), Evolution of basal crevasses links ice shelf stability to ocean forcing, *Earth Planet. Sci. Lett.*, *409*, 203–211, doi:10.1016/j.epsl.2014.11.003.

Bender, M., T. Sowers, and L. Labeyrie (1994), The Dole effect and its variations during the last 130,000 years as measured in the Vostok ice core, *Glob. Biogechemical Cycles*, *8*(3), 363–376.

Bender, M. L., B. Barnett, G. Dreyfus, J. Jouzel, and D. Porcelli (2008), The contemporary degassing rate of 40Ar from the solid Earth, *PNAS*, *105*(24), 8232–8237, doi:10.1073/pnas.0711679105.

Benn, D. I., C. R. Warren, and R. H. Mottram (2007), Calving processes and the dynamics of calving glaciers, *Earth-Science Rev.*, *82*, 143–179.

Bereiter, B., H. Fischer, J. Schwander, and T. F. Stocker (2014), Diffusive equilibration of N2, O2 and CO2 mixing ratios in a 1.5-million-years-old ice core, *Cryosphere*, *8*(1), 245–256, doi:10.5194/tc-8-245-2014.

Berger, A., X. S. Li, and M. F. Loutre (1999), Modelling northern hemisphere ice volume over the last 3 Ma, *Quat. Sci. Rev.*, *18*, 1–11.

Bevan, S. L., A. J. Luckman, and T. Murray (2012), Glacier dynamics over the last quarter of a century at Helheim, Kangerdlugssuaq, and 14 other major Greenland outlet glaciers, *Cryosph.*, *6*(5), 923–937, doi:10.5194/tc-6-923-2012.

Bevan, S. L., A. J. Luckman, S. A. Khan, and T. Murray (2015), Seasonal dynamic thinning at Helheim Glacier, *Earth Planet. Sci. Lett.*, *415*, 47–53, doi:10.1016/j.epsl.2015.01.031.

Bintanja, R. (1999), On the glaciological, meteorological, and climatological significance of Antarctic Blue Ice Areas, *Rev. Geophys.*, *37*(3), 337–359.

Blair, B., and M. Hofton (2010), IceBridge LVIS L2 geolocated ground elevation and return energy quartiles. Boulder, CO, USA, *NASA Distrib. Act. Arch. Cent. Natl. Snow Ice Data Cent.*

Blankenship, D. D., C. R. Bentley, S. T. Rooney, and R. B. Alley (1986), Seismic measurements reveal a saturated porous layer beneath an active Antarctic ice stream, *Nature*, *322*(6074), 54–57, doi:10.1038/322054a0.

Bondzio, J. H., M. Morlighem, H. Seroussi, T. Kleiner, M. Rückamp, J. Mouginot, T. Moon, E. Y. Larour, and A. Humbert (2017), The mechanisms behind Jakobshavn Isbræ's acceleration and mass loss: A 3-D thermomechanical model study, *Geophys. Res. Lett.*, (May), doi:10.1002/2017GL073309.

Van Den Broeke, M. R., E. M. Enderlin, I. M. Howat, P. Kuipers Munneke, B. P. Y. Noël, W. Jan Van De Berg, E. Van Meijgaard, and B. Wouters (2016), On the recent contribution of the Greenland ice sheet to sea level change, *Cryosphere*, *10*(5), 1933–1946, doi:10.5194/tc-10-1933-2016.

Brondex, J., O. Gagliardini, F. Gillet-Chaulet, and G. Durand (2017), Sensitivity of grounding line dynamics to the choice of the friction law, *J. Glaciol.*, *63*(241), 854–866, doi:10.1017/jog.2017.51.

Budd, W. F. (1970), Ice flow over bedrock perturbations, *J. Glaciol.*, *9*(55), 29–48.

Buizert, C. et al. (2014), Radiometric 81Kr dating identifies 120,000-year-old ice at Taylor Glacier, Antarctica., *PNAS*, *111*(19), 6876–6881, doi:10.1073/pnas.1320329111.

Cavitte, M. P., D. D. Blankenship, D. A. Young, D. M. Schroeder, F. Parrenin, E. Lemeur, J. A. MacGregor, and M. J. Siegert (2016), Deep radiostratigraphy of the East Antarctic plateau: connecting the Dome C and Vostok ice core sites, *J. Glaciol.*, *62*(232), 323–334, doi:10.1017/jog.2016.11.

Clark, P. U., D. Archer, D. Pollard, J. D. Blum, J. A. Rial, V. Brovkin, A. C. Mix, N. G. Pisias, and M. Roy (2006), The middle Pleistocene transition: characteristics, mechanisms, and implications for long-term changes in atmospheric pCO2, *Quat. Sci. Rev.*, *25*, 3150–3184, doi:10.1016/j.quascirev.2006.07.008.

Clarke, G. K. C. (2005), Subglacial Processes, *Annu. Rev. Earth Planet. Sci.*, *33*(1), 247–276, doi:10.1146/annurev.earth.33.092203.122621.

Cook, S., I. C. Rutt, T. Murray, A. J. Luckman, T. Zwinger, N. Selmes, A. Goldsack, and T. D.

James (2014), Modelling environmental influences on calving at Helheim Glacier in eastern Greenland, *Cryosph.*, *8*(3), 827–841, doi:10.5194/tc-8-827-2014.

Cuffey, K. M., and W. S. B. Paterson (2010), *The physics of glaciers*, 4th ed., Elsevier, Oxford.

Dadic, R., R. Mott, M. Lehning, M. Carenzo, B. Anderson, and A. Mackintosh (2013), Sensitivity of turbulent fluxes to wind speed over snow surfaces in different climatic settings, *Adv. Water Resour.*, *55*, 178–189, doi:10.1016/j.advwatres.2012.06.010.

Dadic, R., M. Schneebeli, N. A. N. Bertler, M. Schwikowski, and M. Matzl (2015), Extreme snow metamorphism in the Allan Hills, Antarctica, as an analogue for glacial conditions with implications for stable isotope composition, *J. Glaciol.*, *61*(230), 1171–1182, doi:10.3189/2015JoG15J027.

Davies, J. H. (2013), Global map of solid Earth surface heat flow, *Geochemistry, Geophys. Geosystems*, *14*(10), 4608–4622, doi:10.1002/ggge.20271.

Delisle, G., and J. Sievers (1991), Sub-ice topography and meteorite finds near the Allan Hills and near the Western Ice Field, Victoria Land, Antarctica, *J. Geophys. Res.*, *96*(E1), 15,577-15,587.

Donlon, C. J., M. Martin, J. Stark, J. Roberts-Jones, E. Fiedler, and W. Wimmer (2012), The Operational Sea Surface Temperature and Sea Ice Analysis (OSTIA) system, *Remote Sens. Environ.*, *116*, 140–158, doi:10.1016/j.rse.2010.10.017.

Dow, C. F., A. Hubbard, A. D. Booth, S. H. Doyle, A. Gusmeroli, and B. Kulessa (2013), Seismic evidence of mechanically weak sediments underlying Russell Glacier, West Greenland, *Ann. Glaciol.*, *54*(64), 135–141, doi:10.3189/2013AoG64A032.

Doyle, S. H., B. Hubbard, P. Christoffersen, T. J. Young, C. Hofstede, M. Bougamont, J. E. Box, and A. Hubbard (2018), Physical Conditions of Fast Glacier Flow: 1. Measurements From Boreholes Drilled to the Bed of Store Glacier, West Greenland, *J. Geophys. Res. Earth Surf.*, *123*(2), 324–348, doi:10.1002/2017JF004529.

Dunbar, N. W., P. R. Kyle, W. C. McIntosh, and R. P. Esser (1995), Allan Hills, Antarctica: a new source of glacial tephrochronological data, *Antarct. J. United States*, *30*(5), 76–78.

Dutton, A., A. E. Carlson, A. J. Long, G. A. Milne, P. U. Clark, R. DeConto, B. P. Horton, S. Rahmstorf, and M. E. Raymo (2015), Sea-level rise due to polar ice-sheet mass loss during past warm periods, *Science*, *349*(6244), aaa4019-aaa4019, doi:10.1126/science.aaa4019.

Enderlin, E. M., I. M. Howat, and A. Vieli (2013), High sensitivity of tidewater outlet glacier dynamics to shape, *Cryosph.*, *7*, 1007–1015, doi:10.5194/tc-7-1007-2013.

Enderlin, E. M., I. M. Howat, S. Jeong, M. J. Noh, J. H. Van Angelen, and M. R. Van Den Broeke (2014), An improved mass budget for the Greenland ice sheet, *Geophys. Res. Lett.*, *41*(3), 866–872, doi:10.1002/2013GL059010.

EPICA Community Members (2004), Eight glacial cycles from an Antarctic ice core, *Nature*, *429*(6992), 623–628, doi:10.1038/nature02599.

Everett, A. et al. (2016), Annual down-glacier drainage of lakes and water-filled crevasses at Helheim Glacier , southeast Greenland, *J. Geophys. Res. Earth Surf.*, *121*, 1819–1833, doi:10.1002/2016JF003831.

Felikson, D. et al. (2017), Inland thinning on the Greenland ice sheet controlled by outlet glacier geometry, *Nat. Geosci.*, (April), doi:10.1038/ngeo2934.

Fischer, H. et al. (2013), Where to find 1.5 million yr old ice for the IPICS “Oldest-Ice” ice core, *Clim. Past*, *9*(6), 2489–2505, doi:10.5194/cp-9-2489-2013.

Fretwell, P. et al. (2013), Bedmap2: Improved ice bed, surface and thickness datasets for Antarctica, *Cryosphere*, *7*(1), 375–393, doi:10.5194/tc-7-375-2013.

Fudge, T. J., E. D. Waddington, H. Conway, J. M. D. Lundin, and K. Taylor (2014), Interpolation methods for Antarctic ice-core timescales: Application to Byrd, Siple Dome and Law Dome ice cores, *Clim. Past*, *10*(3), 1195–1209, doi:10.5194/cp-10-1195-2014.

Fujisada, H., G. B. Bailey, G. G. Kelly, S. Hara, and M. J. Abrams (2005), ASTER DEM performance, *IEEE Trans. Geosci. Remote Sens.*, *43*(12), 2707–2713, doi:10.1109/TGRS.2005.847924.

Fujita, S., H. Maeno, S. Uratsuka, T. Furukawa, S. Mae, Y. Fujii, and O. Watanabe (1999), Nature of radio echo layering in the Antarctic ice sheet detected by a two-frequency experiment, *J. Geophys. Res.*, *104*(B6), 13013–13024, doi:10.1029/1999JB900034.

Gagliardini, O., D. Cohen, P. Raback, and T. Zwinger (2007), Finite-element modeling of subglacial cavities and related friction law, *J. Geophys. Res.*, *112*, F02027, doi:10.1029/2006JF000576,.

Gagliardini, O. et al. (2013), Capabilities and performance of Elmer/Ice, a new-generation ice sheet model, *Geosci. Model Dev.*, *6*(4), 1299–1318, doi:10.5194/gmd-6-1299-2013.

Gillet-Chaulet, F., O. Gagliardini, H. Seddik, M. Nodet, G. Durand, C. Ritz, T. Zwinger, R. Greve, and D. G. Vaughan (2012), Greenland ice sheet contribution to sea-level rise from a new-generation ice-sheet model, *Cryosphere*, *6*(6), 1561–1576, doi:10.5194/tc-6-1561-2012.

Gillet-Chaulet, F., G. Durand, O. Gagliardini, C. Mosbeux, J. Mouginot, F. Rémy, and C. Ritz (2016), Assimilation of surface velocities between 1996 and 2010 to constrain the form of the basal friction law under Pine Island Glacier, *Geophys. Res. Lett.*, (1), 1–11, doi:10.1002/2016GL069937.

Glen, J. (1955), The creep of polycrystalline ice, *Proc. R. Soc. London, Ser. A, Math. Phys. Sci.*, *228*(1175), 519–538.

Goldberg, D. N., P. Heimbach, I. Joughin, and B. Smith (2015), Committed retreat of Smith, Pope, and Kohler Glaciers over the next 30 years inferred by transient model calibration, *Cryosph.*, *9*, 2429–2446, doi:10.5194/tcd-9-4459-2015.

Grinsted, A., J. Moore, V. B. Spikes, and A. Sinisalo (2003), Dating Antarctic blue ice areas using a novel ice flow model, *Geophys. Res. Lett.*, *30*(19), 2005, doi:10.1029/2003GL017957.

Gudmundsson, G. H. (2003), Transmission of basal variability to a glacier surface, *J. Geophys. Res. Solid Earth*, *108*(B5), 1–19, doi:10.1029/2002JB002107.

Gudmundsson, G. H., J. Krug, G. Durand, L. Favier, and O. Gagliardini (2012), The stability of grounding lines on retrograde slopes, *Cryosph.*, *6*, 1497–1505, doi:10.5194/tc-6-1497-2012.

Habermann, M., D. Maxwell, and M. Truffer (2012), Reconstruction of basal properties in ice sheets using iterative inverse methods, *J. Glaciol.*, *58*(210), 795–807, doi:10.3189/2012JoG11J168.

Habermann, M., M. Truffer, and D. Maxwell (2013), Changing basal conditions during the speed-up of Jakobshavn Isbræ, Greenland, *Cryosph.*, *7*(6), 1679–1692, doi:10.5194/tc-7-1679-2013.

Hanna, E., J. Cappelen, X. Fettweis, P. Huybrechts, A. J. Luckman, and M. H. Ribergaard (2009), Hydrologic response of the Greenland ice sheet: the role of oceanographic warming, *Hydrol. Process.*, *23*, 7–30, doi:10.1002/hyp.

Higgins, J. A., A. V Kurbatov, N. E. Spaulding, E. Brook, D. S. Introne, L. M. Chimiak, Y. Yan, P. A. Mayewski, and M. L. Bender (2015), Atmospheric composition 1 million years ago from blue ice in the Allan Hills, Antarctica, *Proc. Natl. Acad. Sci.*, *112*(22), 6887–6891, doi:10.1073/pnas.1420232112.

Hoffman, M., and S. Price (2014), Feedbacks between coupled subglacial hydrology and glacier dynamics, *J. Geophys. Res. Earth Surf.*, *119*(3), 414–436, doi:10.1002/2013JF002943.

Hofstede, C., P. Christoffersen, B. Hubbard, S. H. Doyle, T. J. Young, A. Diez, O. Eisen, and A. Hubbard (2018), Physical Conditions of Fast Glacier Flow: 2. Variable Extent of Anisotropic Ice and Soft Basal Sediment From Seismic Reflection Data Acquired on Store Glacier, West Greenland, *J. Geophys. Res. Earth Surf.*, *123*(2), 349–362, doi:10.1002/2017JF004297.

Höhle, J., and M. Höhle (2009), Accuracy assessment of digital elevation models by means of robust statistical methods, *ISPRS J. Photogramm. Remote Sens.*, *64*(4), 398–406, doi:10.1016/j.isprsjprs.2009.02.003.

Holland, D. M., R. H. Thomas, B. Young, M. H. Ribergaard, and B. Lyberth (2008), Acceleration of Jakobshavn Isbrae triggered by warm subsurface ocean waters, *Nat. Geosci.*, *1*, 659–664, doi:10.1038/ngeo316.

Howard, W. R. (1997), A warm future in the past, *Nature*, *388*(6641), 418–419, doi:10.1038/41201.

Howat, I. (2017), MEaSURES Greenland Ice Velocity: Selected Glacier Site Velocity Maps from Optical Images, Version 2. OPT_E66.50N and OPT_E68.80N Boulder, CO, USA, *NASA Natl. Snow Ice Data Cent. Distrib. Act. Arch. Cent.*, doi:10.5067/VM5DZ20MYF5C.

Howat, I. M., I. R. Joughin, S. Tulaczyk, and S. Gogineni (2005), Rapid retreat and acceleration of Helheim Glacier, east Greenland, *Geophys. Res. Lett.*, *32*(22), L22502, doi:10.1029/2005GL024737.

Howat, I. M., I. R. Joughin, and T. A. Scambos (2007), Rapid changes in ice discharge from Greenland outlet glaciers, *Science*, *315*(5818), 1559–61, doi:10.1126/science.1138478.

Howat, I. M., I. R. Joughin, M. A. Fahnestock, B. E. Smith, and T. A. Scambos (2008), Synchronous retreat and acceleration of southeast greenland outlet glaciers 2000-06: ice dynamics and coupling to climate, *J. Glaciol.*, *54*(187), 646–660.

Howat, I. M., J. E. Box, Y. Ahn, A. Herrington, and E. M. McFadden (2010), Seasonal variability in the dynamics of marine-terminating outlet glaciers in Greenland, *J. Glaciol.*, *56*(198), 601–613, doi:10.3189/002214310793146232.

Howat, I. M., Y. Ahn, I. R. Joughin, M. R. van den Broeke, J. T. M. Lenaerts, and B. E. Smith (2011), Mass balance of Greenland's three largest outlet glaciers, 2000-2010, *Geophys. Res. Lett.*, *38*(12), doi:10.1029/2011GL047565.

Iken, A. (1981), The effect of the subglacial water pressure on the sliding velocity of a glacier in an idealized numerical model, *J. Glaciol.*, *27*, 407–421.

Inall, M. E., T. Murray, F. R. Cottier, K. Scharrer, T. J. Boyd, K. J. Heywood, and S. L. Bevan (2014), Oceanic heat delivery via Kangerdlugssuaq Fjord to the south-east Greenland ice sheet, *J. Geophys. Res. Ocean.*, *119*, 631–645, doi:10.1002/2013JC009295.

IPCC (2014a), *Climate Change 2014: Impacts, Adaptation, and Vulnerability. Contribution of Working Group II to the Fifth Assessment Report of the Intergovernmental Panel on Climate Change*, Cambridge University Press, Cambridge, United Kingdom and New York, NY, USA.

IPCC (2014b), *Climate Change 2014: The Physical Basis. Contribution of Working Group I to the Fifth Assessment Report of the Intergovernmental Panel on Climate Change*, preliminar., Cambridge University Press, Cambridge, United Kingdom and New York, NY, USA.

James, T. D., T. Murray, N. Selmes, K. Scharrer, and M. O'Leary (2014), Buoyant flexure and basal crevassing in dynamic mass loss at Helheim Glacier, *Nat. Geosci.*, *7*(8), 593–596, doi:10.1038/ngeo2204.

Jay-Allemand, M., F. Gillet-Chaulet, O. Gagliardini, and M. Nodet (2011), Investigating changes in basal conditions of Variegated Glacier prior and during its 1982–1983 surge, *Cryosph. Discuss.*, *5*(3), 1461–1494, doi:10.5194/tcd-5-1461-2011.

Jensen, T. S., J. E. Box, and C. S. Hvidberg (2016), A sensitivity study of annual area change for Greenland ice sheet marine terminating outlet glaciers: 1999-2013, *J. Glaciol.*, *62*(231), 72–81, doi:10.1017/jog.2016.12.

Joughin, I., I. Howat, B. Smith, and T. Scambos (2016), MEaSUREs Greenland Ice Velocity: Selected Glacier Site Velocity Maps from InSAR, Version 1, *NASA Natl. Snow Ice Data Cent. Distrib. Act. Arch. Cent.*, doi:https://doi.org/10.5067/MEASURES/CRYOSPHERE/nsidc-0481.001.

Joughin, I., B. E. Smith, and I. Howat (2018), Greenland Ice Mapping Project: Ice flow velocity variation at sub-monthly to decadal timescales, *Cryosph.*, *12*(7), 2211–2227, doi:10.5194/tc-12-2211-2018.

Joughin, I. R. (2002), Ice-sheet velocity mapping: a combined interferometric and speckle-tracking approach, *Ann. Glaciol.*, *34*, 195–201.

Joughin, I. R., D. R. MacAyeal, and S. Tulaczyk (2004a), Basal shear stress of the Ross ice streams from control method inversions, *J. Geophys. Res.*, *109*, B09405, doi:10.1029/2003JB002960.

Joughin, I. R., W. Abdalati, and M. A. Fahnestock (2004b), Large fluctuations in speed on Greenland's Jakobshavn Isbrae glacier., *Nature*, *432*(7017), 608–10, doi:10.1038/nature03130.

Joughin, I. R., I. M. Howat, M. Fahnestock, B. E. Smith, W. Krabill, R. B. Alley, H. Stern, and M. Truffer (2008a), Continued evolution of Jakobshavn Isbrae following its rapid speedup, *J. Geophys. Res. Earth Surf.*, *113*(F04006), doi:10.1029/2008JF001023.

Joughin, I. R., I. M. Howat, R. B. Alley, G. Ekstrom, M. A. Fahnestock, T. Moon, M. Nettles, M. Truffer, and V. C. Tsai (2008b), Ice-front variation and tidewater behavior on Helheim and Kangerdlugssuaq Glaciers, Greenland, *J. Geophys. Res.*, *113*, F01004, doi:10.1029/2007JF000837.

Joughin, I. R., S. B. Das, M. A. King, B. E. Smith, I. M. Howat, and T. Moon (2008c), Seasonal speedup along the western flank of the Greenland Ice Sheet, *Science*, *320*, 781–783, doi:10.1126/science.1153288.

Joughin, I. R., S. Tulaczyk, J. L. Bamber, D. D. Blankenship, J. W. Holt, T. A. Scambos, and D. G. Vaughan (2009), Basal conditions for Pine Island and Thwaites Glaciers, West Antarctica, determined using satellite and airborne data, *J. Glaciol.*, *55*(190), 245–257, doi:10.3189/002214309788608705.

Joughin, I. R., B. E. Smith, I. M. Howat, T. Scambos, and T. Moon (2010a), Greenland flow variability from ice-sheet-wide velocity mapping, *J. Glaciol.*, *56*(197), 415–430.

Joughin, I. R., B. E. Smith, and D. M. Holland (2010b), Sensitivity of 21st century sea level to ocean-induced thinning of Pine Island Glacier, Antarctica, *Geophys. Res. Lett.*, *37*(20), L20502, doi:10.1029/2010GL044819.

Joughin, I. R., B. E. Smith, I. M. Howat, D. Floricioiu, R. B. Alley, M. Truffer, and M. A. Fahnestock (2012), Seasonal to decadal scale variations in the surface velocity of Jakobshavn Isbrae, Greenland: Observation and model-based analysis, *J. Geophys. Res.*, *117*(F2), F02030, doi:10.1029/2011JF002110.

Jouzel, J., and V. Masson-Delmotte (2010), Deep ice cores: The need for going back in time, *Quat. Sci. Rev.*, *29*(27–28), 3683–3689, doi:10.1016/j.quascirev.2010.10.002.

Kehrl, L., H. Conway, N. Holschuh, S. Campbell, A. V. Kurbatov, and N. E. Spaulding (2018), Evaluating the duration and continuity of potential climate records from the Allan Hills Blue Ice Area, East Antarctica, *Geophys. Res. Lett.*, 1–9, doi:10.1029/2018GL077511.

Kehrl, L. M., I. Joughin, D. E. Shean, D. Floricioiu, and L. Krieger (2017), Seasonal and interannual variabilities in terminus position, glacier velocity, and surface elevation at Helheim and Kangerlussuaq Glaciers from 2008 to 2016, *J. Geophys. Res. Earth Surf.*, *122*(9), 1635–1652, doi:10.1002/2016JF004133.

Korona, J., E. Berthier, M. Bernard, F. Remy, and E. Thouvenot (2009), SPIRIT. SPOT 5 stereoscopic survey of Polar Ice: Reference Images and Topographies during the fourth International Polar Year (2007-2009), *ISPRS J. Photogramm. Remote Sens.*, *64*(2), 204–212, doi:10.1016/j.isprsjprs.2008.10.005.

Krabill, W. B. (2010), IceBridge ATM L2 Icessn Elevation, Slope, and Roughness, Version 2. Greenland. Boulder, Colorado, USA: NASA DAAC at the National Snow and Ice Data Center, *NASA Natl. Snow Ice Data Cent. Distrib. Act. Arch. Cent.*, doi:10.5067/CPRXXK3F39RV.

Krieger, G. et al. (2013), TanDEM-X: A radar interferometer with two formation-flying satellites, *Acta Astronaut.*, *89*, 83–98, doi:10.1016/j.actaastro.2013.03.008.

Kyrke-Smith, T. M., G. H. Gudmundsson, and P. E. Farrell (2017), Can Seismic Observations of Bed Conditions on Ice Streams Help Constrain Parameters in Ice Flow Models?, *J. Geophys. Res. Earth Surf.*, *122*(11), 2269–2282, doi:10.1002/2017JF004373.

van Liefferinge, B., and F. Pattyn (2013), Using ice-flow models to evaluate potential sites of million year-old ice in Antarctica, *Clim. Past*, *9*(5), 2335–2345, doi:10.5194/cp-9-2335-2013.

Lisiecki, L. E., and M. E. Raymo (2005), A Pliocene-Pleistocene stack of 57 globally distributed benthic δ 18O records, *Paleoceanography*, *20*(1), 1–17, doi:10.1029/2004PA001071.

Loutre, M. F., and A. Berger (2003), Marine Isotope Stage 11 as an analogue for the present interglacial, *Glob. Planet. Change*, *36*(3), 209–217, doi:10.1016/S0921-8181(02)00186-8.

Lüthi, M., M. Funk, A. Iken, S. Gogineni, and M. Truffer (2002), Mechanisms of fast flow in Jakobshavns Isbræ, Greenland, Part III: Measurements of ice deformation, temperature and cross-borehole conductivity in boreholes to the bedrock, *J. Glaciol.*, *48*(162), 369–385, doi:10.3189/172756502781831322.

MacAyeal, D. R. (1989), Large-scale ice flow over a viscous basal sediment: theory and application to Ice Stream B, Antarctica, *J. Geophys. Res.*, *94*, 4071–4087.

MacAyeal, D. R. (1993), A tutorial on the use of control methods in ice sheet modeling, *J. Glaciol.*, *39*(131), 91–98.

Masson-Delmotte, V. et al. (2010), EPICA Dome C record of glacial and interglacial intensities, *Quat. Sci. Rev.*, *29*(1–2), 113–128, doi:10.1016/j.quascirev.2009.09.030.

Meier, M. F., and A. Post (1987), Fast tidewater glaciers, *J. Geophys. Res.*, *92*(B9), 9051–9058.

Minchew, B., M. Simons, H. Björnsson, F. Pálsson, M. Morlighem, H. Seroussi, E. Larour, and S. Hensley (2016), Plastic bed beneath Hofsjökull ice cap, central Iceland, and the sensitivity of ice flow to surface meltwater flux, *J. Glaciol.*, *62*(231), 147–158, doi:10.1017/jog.2016.26.

Moon, T., and I. R. Joughin (2008), Changes in ice front position on Greenland's outlet glaciers from 1992 to 2007, *J. Geophys. Res.*, *113*, F02022, doi:10.1029/2007JF000927.

Moon, T., I. R. Joughin, B. E. Smith, and I. M. Howat (2012), 21st-century evolution of Greenland outlet glacier velocities., *Science*, *336*, 576–578, doi:10.1126/science.1219985.

Moon, T., I. R. Joughin, B. E. Smith, M. R. Broeke, W. J. Berg, B. Noël, and M. Usher (2014), Distinct patterns of seasonal Greenland glacier velocity, *Geophys. Res. Lett.*, *41*, 7209–7216, doi:10.1002/2014GL061836.

Moon, T., I. R. Joughin, and B. E. Smith (2015), Seasonal to multiyear variability of glacier surface velocity, terminus position, and sea ice/ice melange in northwest Greenland, *J. Geophys. Res. Earth Surf.*, *120*, 818–833, doi:10.1002/2015JF003494.

Moore, J. C., F. Nishio, S. Fujita, H. Narita, E. Pasteur, A. Grinsted, A. Sinisalo, and N. Maeno (2006), Interpreting ancient ice in a shallow ice core from the South Yamato (Antarctica) blue ice area using flow modeling and compositional matching to deep ice cores, *J. Geophys. Res. Atmos.*, *111*(16), 1–17, doi:10.1029/2005JD006343.

Morlighem, M., E. Rignot, H. Seroussi, E. Larour, H. Ben Dhia, and D. Aubry (2010), Spatial patterns of basal drag inferred using control methods from a full-Stokes and simpler models for Pine Island Glacier, West Antarctica, *Geophys. Res. Lett.*, *37*(14), 1–6, doi:10.1029/2010GL043853.

Morlighem, M., E. Rignot, J. Mouginot, H. Seroussi, and E. Larour (2014), Deeply incised submarine glacial valleys beneath the Greenland ice sheet, *Nat. Geosci.*, *7*, 18–22, doi:10.1038/NGEO2167.

Morlighem, M. et al. (2017), BedMachine v3: Complete Bed Topography and Ocean Bathymetry Mapping of Greenland From Multibeam Echo Sounding Combined With Mass Conservation, *Geophys. Res. Lett.*, *44*(21), 11,051-11,061, doi:10.1002/2017GL074954.

Motyka, R. J., M. Truffer, M. A. Fahnestock, J. Mortensen, S. Rysgaard, and I. M. Howat (2011), Submarine melting of the 1985 Jakobshavn Isbræ floating tongue and the triggering of the current retreat, *J. Geophys. Res.*, *116*, F01007, doi:10.1029/2009JF001632.

Motyka, R. J. et al. (2017), Asynchronous behavior of outlet glaciers feeding Godthåbsfjord (Nuup Kangerlua) and the triggering of Narsap Sermia's retreat in SW Greenland, *J. Glaciol.*, *63*(238), 288–308, doi:10.1017/jog.2016.138.

Murray, T. et al. (2010), Ocean regulation hypothesis for glacier dynamics in southeast Greenland and implications for ice sheet mass changes, *J. Geophys. Res. Earth Surf.*, *115*(3), 1–15, doi:10.1029/2009JF001522.

Murray, T., N. Selmes, T. D. James, S. Edwards, I. Martin, T. O'Farrell, R. Aspey, I. Rutt, M. Nettles, and T. Bauge (2015), Dynamics of glacier calving at the ungrounded margin of Helheim Glacier, southeast Greenland, *J. Geophys. Res. Earth Surf.*, *120*, 964–982, doi:10.1002/2015JF003531.

NEEM Community Members (2013), Eemian interglacial reconstructed from a Greenland folded ice core, *Nature*, *493*(7433), 489–494, doi:10.1038/nature11789.

Nettles, M. et al. (2008), Step-wise changes in glacier flow speed coincide with calving and glacial earthquakes at Helheim Glacier, Greenland, *Geophys. Res. Lett.*, *35*(24), 1–5.

Nick, F. M., A. Vieli, I. M. Howat, and I. R. Joughin (2009), Large-scale changes in Greenland outlet glacier dynamics triggered at the terminus, *Nat. Geosci.*, *2*(2), 110–114, doi:10.1038/ngeo394.

Nick, F. M., A. Vieli, M. L. Andersen, I. R. Joughin, A. J. Payne, T. L. Edwards, F. Pattyn, and R. S. W. van de Wal (2013), Future sea-level rise from Greenland's main outlet glaciers in a warming climate, *Nature*, *497*(7448), 235–8, doi:10.1038/nature12068.

Nishiizumi, K., D. Elmore, and P. W. Kubik (1989), Update on terrestrial ages of Antarctic meteorites, *Earth Planet. Sci. Lett.*, *93*(3–4), 299–313, doi:10.1016/0012-821X(89)90029-0.

Noël, B., W. J. Van De Berg, E. Van Meijgaard, P. Kuipers Munneke, R. S. W. Van De Wal, and M. R. Van Den Broeke (2015), Evaluation of the updated regional climate model RACMO2.3: Summer snowfall impact on the Greenland Ice Sheet, *Cryosphere*, *9*(5), 1831–1844, doi:10.5194/tc-9-1831-2015.

Noël, B., W. Jan Van De Berg, H. MacHguth, S. Lhermitte, I. Howat, X. Fettweis, and M. R. Van Den Broeke (2016), A daily, 1 km resolution data set of downscaled Greenland ice sheet surface mass balance (1958-2015), *Cryosphere*, *10*(5), 2361–2377, doi:10.5194/tc-10-2361-2016.

O'Leary, M., and P. Christoffersen (2013), Calving on tidewater glaciers amplified by submarine frontal melting, *Cryosph.*, *7*(1), 119–128, doi:10.5194/tc-7-119-2013.

Parrenin, F. et al. (2017), Is there 1.5 million-year old ice near Dome C, Antarctica?, *Cryosph.*, *11*, 2427–2437, doi:10.5194/tc-11-2427-2017.

Petit, J. R. et al. (1999), Climate and atmospheric history of the past 420,000 years from the Vostok ice core, Antarctica, *Nature*, *399*, 429–436.

Poinar, K., I. R. Joughin, D. Lilien, L. Brucker, L. M. Kehrl, and S. Nowicki (2017), Drainage of Southeast Greenland firn aquifer water through crevasses to the bed, *Front. Earth Sci.*, *5*, 5, doi:10.3389/FEART.2017.00005.

Price, S. F., H. Conway, E. D. Waddington, and R. A. Bindschadler (2008), Model investigations of inland migration of fast-flowing outlet glaciers and ice streams, *J. Glaciol.*, *54*(184), 49–60.

Price, S. F., A. J. Payne, I. M. Howat, and B. E. Smith (2011), Committed sea-level rise for the next century from Greenland ice sheet dynamics during the past decade, *Proc. Natl. Acad. Sci.*, *108*(22), 8978–8983, doi:10.1073/pnas.1017313108.

Pritchard, H. D., S. R. M. Ligtenberg, H. A. Fricker, D. G. Vaughan, M. R. van den Broeke, and L. Padman (2012), Antarctic ice-sheet loss driven by basal melting of ice shelves, *Nature*.

Reeh, N. (1968), On the calving of ice from floating glaciers, *J. Glaciol.*, *7*(50), 215–232.

Rignot, E., I. Fenty, Y. Xu, C. Cai, I. Velicogna, C. Cofaigh, J. A. Dowdeswell, W. Weinrebe, G. Catania, and D. Duncan (2016), Bathymetry data reveal glaciers vulnerable to ice-ocean interaction in Uummannaq and Vaigat glacial fjords, west Greenland, *Geophys. Res. Lett.*, *43*, 2667–2674, doi:10.1002/2016GL067832.

Rignot, E. J., and P. Kanagaratnam (2006), Changes in the velocity structure of the Greenland Ice Sheet, *Science*, *311*(5763), 986–990, doi:10.1126/science.1121381.

Rignot, E. J., D. Braaten, S. P. Gogineni, W. B. Krabill, and J. R. McConnell (2004), Rapid ice discharge from southeast Greenland glaciers, *Geophys. Res. Lett.*, *31*(10), 2–5, doi:10.1029/2004GL019474.

Ritz, C., T. L. Edwards, G. Durand, A. J. Payne, V. Peyaud, and R. C. A. Hindmarsh (2015), Potential sea-level rise from Antarctic ice-sheet instability constrained by observations, *Nature*, *528*(7580), 115–118, doi:10.1038/nature16147.

Rossi, C., F. Rodriguez Gonzalez, T. Fritz, N. Yague-Martinez, and M. Eineder (2012), TanDEM-X calibrated Raw DEM generation, *ISPRS J. Photogramm. Remote Sens.*, *73*, 12–20, doi:10.1016/j.isprsjprs.2012.05.014.

San, B. T., and M. L. Süzen (2005), Digital elevation model (DEM) generation and accuracy assessment from ASTER stereo data, *Int. J. Remote Sens.*, *26*(22), 5013–5027, doi:10.1080/01431160500177620.

Schild, K. M., and G. S. Hamilton (2013), Seasonal variations of outlet glacier terminus position in Greenland, *J. Glaciol.*, *59*(216), 759–770, doi:10.3189/2013JoG12J238.

Schoof, C. G. (2005), The effect of cavitation on glacier sliding, *Proc. R. Soc. A Math. Phys. Eng. Sci.*, *461*(2055), 609.

Schoof, C. G. (2007), Ice sheet grounding line dynamics: Steady states, stability, and hysteresis, *J. Geophys. Res.*, *112*, F03S28, doi:10.1029/2006JF000664.

Seale, A., P. Christoffersen, R. I. Mugford, and M. O'Leary (2011), Ocean forcing of the Greenland Ice Sheet: Calving fronts and patterns of retreat identified by automatic satellite monitoring of eastern outlet glaciers, *J. Geophys. Res. Earth Surf.*, *116*, F03013, doi:10.1029/2010JF001847.

Shapero, D. R., I. R. Joughin, K. Poinar, M. Morlighem, and F. Gillet-Chaulet (2016), Basal resistance for three of the largest Greenland outlet glaciers, *J. Geophys. Res. Earth Surf.*, *121*, doi:10.1002/2015JF003643.

Shean, D. E., O. Alexandrov, Z. M. Moratto, B. E. Smith, I. R. Joughin, C. C. Porter, and P. J. Morin (2016), An automated, open-source pipeline for mass production of digital elevation models (DEMs) from very-high-resolution commercial stereo satellite imagery, *ISPRS J. Photogramm. Remote Sens.*, *116*, 101–117, doi:10.1016/j.isprsjprs.2016.03.012.

Shepherd, A. P. et al. (2012), A reconciled estimate of ice-sheet mass balance, *Science*, *338*(6111), 1183–9, doi:10.1126/science.1228102.

Sinisalo, A., and J. C. Moore (2010), Antarctic blue ice areas - towards extracting palaeoclimate information, *Antarct. Sci. Antarct. Sci. Ltd*, *22*(2), 99–115, doi:10.1017/S0954102009990691.

Sinisalo, A., A. Grinsted, and J. Moore (2004), Dynamics of the Scharffenbergbotnen blue-ice area, Dronning Maud Land, Antarctica, *Ann. Glaciol.*, *39*, 417–422, doi:doi:10.3189/172756404781814177.

Spaulding, N. E., V. B. Spikes, G. S. Hamilton, P. A. Mayewski, N. W. Dunbar, R. P. Harvey, J. Schutt, and A. V Kurbatov (2012), Ice motion and mass balance at the Allan Hills blue-ice area, Antarctica, with implications for paleoclimate reconstructions, *J. Glaciol.*, *58*(208), 399–406, doi:10.3189/2012JoG11J176.

Spaulding, N. E., J. A. Higgins, A. V Kurbatov, M. L. Bender, S. A. Arcone, S. Campbell, N. W. Dunbar, L. M. Chimiak, D. S. Introne, and P. A. Mayewski (2013), Climate archives from 90 to 250 ka in horizontal and vertical ice cores from the Allan Hills Blue Ice Area, Antarctica, *Quat. Res.*, *80*(3), 562–574, doi:10.1016/j.yqres.2013.07.004.

Stearns, L. A., and G. S. Hamilton (2007), Rapid volume loss from two East Greenland outlet glaciers quantified using repeat stereo satellite imagery, *Geophys. Res. Lett.*, *34*, L05503, doi:10.1029/2006GL028982.

Stearns, L. A., and C. J. van der Veen (2018), Friction at the bed does not control fast glacier flow, *Science*, *361*(6399), 273–277, doi:10.1126/science.aat2217.

Steig, E. J., D. L. Morse, E. D. Waddington, M. Stuiver, P. M. Grootes, P. A. Mayewski, M. S. Twickler, and S. I. Whitlow (2000), Wisconsinan and Holocene climate history from an ice core at Taylor Dome, Western Ross Embayment, Antarctica, *Geogr. Ann. Ser. A Phys. Geogr.*, *82*(2–3), 213–235, doi:10.1111/j.0435-3676.2000.00122.x.

Straneo, F., G. S. Hamilton, D. A. Sutherland, L. A. Stearns, F. Davidson, M. O. Hammill, G. B. Stenson, and A. Rosing-Asvid (2010), Rapid circulation of warm subtropical waters in a major glacial fjord in East Greenland, *Nat. Geosci.*, *3*(3), 182–186, doi:10.1038/ngeo764.

Straneo, F., R. G. Curry, D. A. Sutherland, G. S. Hamilton, C. Cenedese, K. Våge, and L. A.

Stearns (2011), Impact of fjord dynamics and glacial runoff on the circulation near Helheim Glacier, *Nat. Geosci.*, *4*(5), 322–327, doi:10.1038/ngeo1109.

Sundal, A. V, A. P. Shepherd, P. W. Nienow, E. Hanna, S. Palmer, and P. Huybrechts (2011), Melt-induced speed-up of Greenland ice sheet offset by efficient subglacial drainage, *Nature*, *469*(7331), 521–4, doi:10.1038/nature09740.

Sundal, A. V, A. P. Shepherd, M. R. van den Broeke, J. H. Van Angelen, N. Gourmelen, and J. Park (2013), Controls on short-term variations in Greenland glacier dynamics, *J. Glaciol.*, *59*(217), 883–892, doi:10.3189/2013JoG13J019.

Tison, J. L. et al. (2015), Retrieving the paleoclimatic signal from the deeper part of the EPICA Dome C ice core, *Cryosphere*, *9*(4), 1633–1648, doi:10.5194/tc-9-1633-2015.

Truffer, M., and R. Motyka (2016), Where glaciers meet water: Subaqueous melt and its relevance to glaciers in various settings, *Rev. Geophys.*, *54*(1), 220–239, doi:10.1002/2015RG000494.

Tulaczyk, S., W. B. Kamb, H. F. Engelhardt, B. Kamb, and H. F. Engelhardt (2000), Basal mechanics of ice stream B, West Antarctica 1. Till mechanics, *J. Geophys. Res.*, *105*(B1), 463–481, doi:10.1029/1999JB900329.

Turney, C., C. Fogwill, T. D. Van Ommen, A. D. Moy, D. Etheridge, M. Rubino, M. A. J. Curran, and A. Rivera (2013), Late Pleistocene and early Holocene change in the Weddell Sea: A new climate record from the Patriot Hills, Ellsworth Mountains, West Antarctica, *J. Quat. Sci.*, *28*(7), 697–704, doi:10.1002/jqs.2668.

Tziperman, E., and H. Gildor (2003), On the mid-Pleistocene transition to 100-kyr glacial cycles and the asymmetry between glaciation and deglaciation times, *Paleoceanography*, *18*(1), 1–8, doi:10.1029/2001PA000627.

Vallot, D., R. Pettersson, A. Luckman, D. I. Benn, T. Zwinger, W. J. Van Pelt, J. Kohler, M. Schäfer, B. Claremar, and N. R. Hulton (2017), Basal dynamics of Kronebreen, a fast-flowing tidewater glacier in Svalbard: Non-local spatio-temporal response to water input, *J. Glaciol.*, *63*(242), 1012–1024, doi:10.1017/jog.2017.69.

Voytenko, D., A. Stern, D. M. Holland, T. H. Dixon, K. Christianson, and R. T. Walker (2015), Tidally driven ice speed variation at Helheim Glacier, Greenland, observed with terrestrial radar interferometry, *J. Glaciol.*, *61*(226), 301–308, doi:10.3189/2015JoG14J173.

Walter, F., S. O'Neel, D. McNamara, W. T. Pfeffer, J. N. Bassis, and H. A. Fricker (2010), Iceberg calving during transition from grounded to floating ice: Columbia Glacier, Alaska, *Geophys. Res. Lett.*, *37*(15), 1–5, doi:10.1029/2010GL043201.

Walter, F., J. Chaput, and M. P. Lüthi (2014), Thick sediments beneath Greenland's ablation zone and their potential role in future ice sheet dynamics, *Geology*, *42*(6), 487–490, doi:10.1130/G35492.1.

Watanabe, O., H. Shoji, K. Satow, H. Motoyama, Y. Fujii, H. Narita, and S. Aoki (2003), Dating of the Dome Fuji, Antarctica deep ice core, *Mem. Natl. Inst. Polar Res. Spec. issue*, *57*, 25–37.

Weertman, J. (1957), On the sliding of glaciers, *J. Glaciol.*, *3*, 33–38, doi:10.1007/978-94-015-8705-1_19.

Whillans, I. M., and W. A. Cassidy (1983), Catch a Falling Star: Meteorites and Old Ice, *Science*, *222*(4619), 55–57.

Winter, A., D. Steinhage, E. J. Arnold, D. D. Blankenship, M. G. P. Cavitte, H. J. Corr, J. Paden, S. Urbini, D. A. Young, and O. Eisen (2017), Comparison of measurements from different radio-echo sounding systems and synchronization with the ice core at Dome C, Antarctica, *Cryosph.*, *11*, 653–668, doi:10.5194/tc-11-653-2017.

Winter, K. et al. (2016), Assessing the continuity of the blue ice climate record at Patriot Hills, Horseshoe Valley, West Antarctica, *Geophys. Res. Lett.*, *43*, 2019–2026, doi:10.1002/2015GL066476.

Yamane, M., Y. Yokoyama, A. Abe-Ouchi, S. Obrochta, F. Saito, K. Moriwaki, and H. Matsuzaki (2015), Exposure age and ice-sheet model constraints on Pliocene East Antarctic ice sheet dynamics., *Nat. Commun.*, *6*, 7016, doi:10.1038/ncomms8016.

Yan, Y., J. Ng, J. Higgins, A. Kurbatov, H. Clifford, N. Spaulding, J. Severinghaus, E. Brook, P. Mayewski, and M. Bender (2017), 2.7-Million-Year-Old Ice from Allan Hills Blue Ice Areas, East Antarctica Reveals Climate Snapshots Since Early Pleistocene, in *Goldschmidt Abstracts*, p. 4359.

Zoet, L. K., and N. R. Iverson (2015), Experimental determination of a double-valued drag relationship for glacier sliding, *J. Glaciol.*, *61*(225), 1–7, doi:10.3189/2015JoG14J174.

Zoet, L. K., and N. R. Iverson (2016), Rate-weakening drag during glacier sliding, *J. Geophys. Res. Earth Surf.*, *121*(7), 1206–1217, doi:10.1002/2016JF003909.

Zwally, H., R. Schutz, C. Bentley, J. Bufton, T. Herring, J. Minster, J. Spinhirne, and R. Thomas (2003), GLAS/ICESat L2 Greenland ice sheet altimetry, *Natl. Snow Ice Data Center, Boulder, CO.*

Zwally, H. J., M. B. Giovinetto, M. A. Beckley, and J. L. Saba (2012), Antarctic and Greenland Drainage Systems,

Zwinger, T., R. Greve, O. Gagliardini, T. Shiraiwa, and M. Lyly (2007), A full Stokes-flow thermo-mechanical model for firn and ice applied to the Gorshkov crater glacier, Kamchatka, *Ann. Glaciol.*, *45*, 29–37, doi:10.3189/172756407782282543.

Zwinger, T., M. Schäfer, C. Martín, and J. C. Moore (2014), Influence of anisotropy on velocity and age distribution at Scharffenbergbotnen blue ice area, *Cryosph.*, *8*(2), 607–621, doi:10.5194/tc-8-607-2014.

APPENDIX A

This section is the supplement for Chapter 2, "Seasonal and interannual variabilities in terminus position, glacier velocity, and surface elevation at Helheim and Kangerlussuaq Glaciers from 2008 to 2016" authored by L. M. Kehrl, I. Joughin, D. E. Shean, D. Floricioiu, and L. Krieger, as it appears in *Journal of Geophysical Research: Earth Surface* 2017.

A.1 Assumption of negligible basal melt

To estimate surface-elevation change rates using the flux-gate method, we assumed that basal melt is negligible. In this section, we discuss the validity of this assumption and the potential uncertainty that it introduces into our surface-elevation change rate estimates. The basal melt rate over grounded ice, $\dot{b}$, can be estimated from

$$\dot{b} = \frac{1}{\rho L_f}\left[\tau_b u_b - k_r \frac{\partial T}{\partial z}|_r + k_i \frac{\partial T}{\partial z}|_i\right], \tag{A.1}$$

where ρ is the ice density (917 kg m^{-3}), L_f is the latent heat of fusion (335,000 J kg^{-1}), τ_b is the basal shear stress, u_b is the sliding speed, k_r is the thermal conductivity of the rock (3.3 W m^{-1} K^{-1}) , $\frac{\partial T}{\partial z}|_r$ is the temperature gradient in the rock, k_i is the thermal conductivity of the ice (2.1 W m^{-1} K^{-1}), and $\frac{\partial T}{\partial z}|_i$ is the temperature gradient in the ice [*Cuffey and Paterson*, 2010]. The first term indicates melt due to frictional heat generated by basal sliding and the second two terms indicate melt due to conduction. Frictional heat should generate much larger melt rates beneath a grounded tidewater glacier than heat conduction. Consequently, if we neglect the last two terms and use reasonable values of τ_b= 40 kPa [*Shapero et al.*, 2016] and u_b= 7 km yr^{-1} for Helheim Glacier, the basal melt rate should be about 0.6 cm d^{-1}. Even if the basal shear stress τ_b is closer to the driving stress (~150-200 kPa), the basal melt rate should be less than ~3 cm d^{-1}, which is within our uncertainty estimates of 3-5 cm d^{-1} for glacier surface-elevation change rates (Figure A.2).

A.2 Surface-elevation change rate error estimates

Both changes in the surface-velocity gradient (i.e., longitudinal strain rate) and the ice-thickness gradient can affect the surface-elevation change rate, dh/dt (Equation 2.1). To highlight the importance of these two terms, we report both the relative velocity between the outflow and inflow boundaries, $\bar{u}_o - \bar{u}_i$, and the relative thickness between the two boundaries, $\bar{H}_i - \bar{H}_o$, in this section. The bar denotes the average value over the middle 4-km of the boundary. We average values over 4 km to avoid the shear margins, where our velocity measurements tend to be less accurate.

Figures A.3 and A.4 show the surface-elevation change rate, the relative velocity between the boundaries, the relative ice thickness, and the ice flux at the two boundaries for Helheim and Kangerlussuaq, respectively. At both glaciers, a change in relative velocity of 100 m yr^{-1} altered dh/dt by ~5-8 cm d^{-1}. In comparison, increasing or decreasing the ice thickness between the two boundaries by 5 m altered dh/dt by ~2 cm d^{-1}. Given the observed changes in glacier velocity and ice thickness, the elevation changes appear to have been largely driven by changes in glacier velocity, rather than by changes in ice thickness.

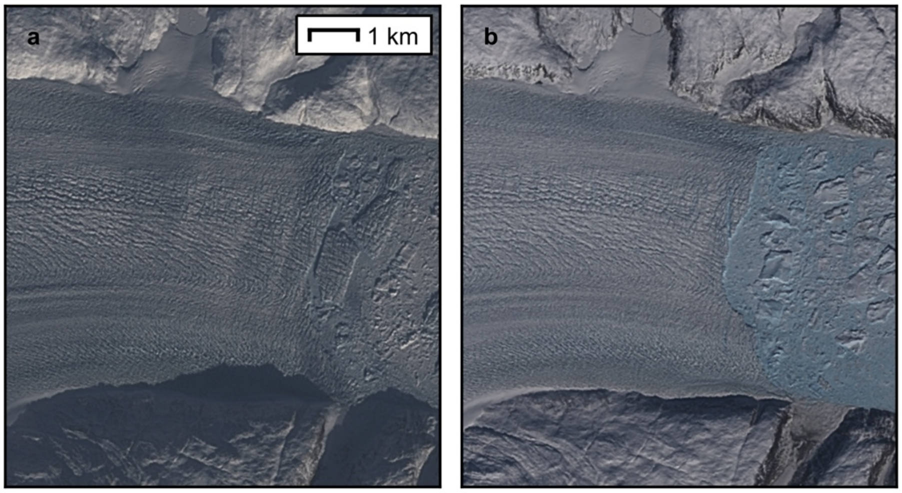

Figure A.1. Example of (a) a tabular iceberg-calving episode (7 March 2014) and (b) a non-tabular iceberg-calving episode (1 May 2014) at Helheim. Both images are from Landsat 8.

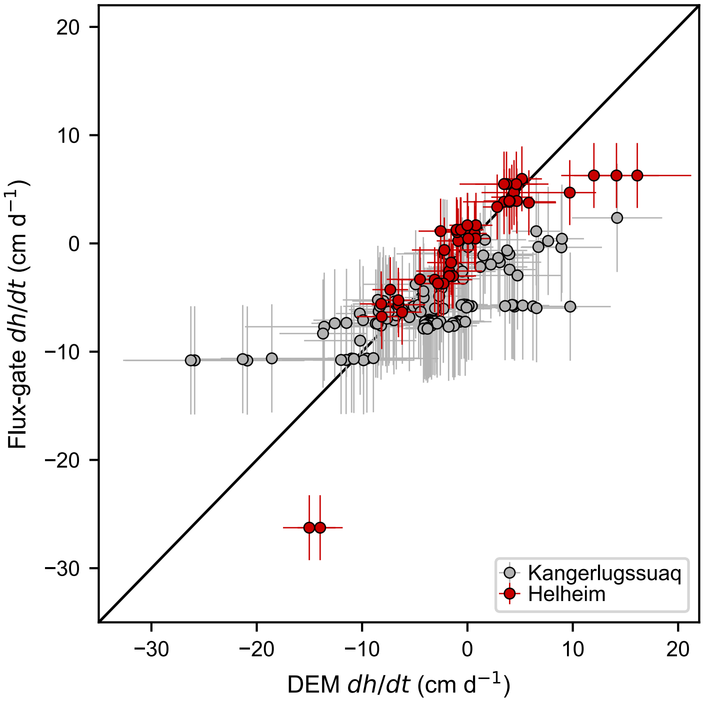

Figure A.2. Comparison of surface-elevation change rates, *dh/dt*, using the DEM and flux-gate methods. The RMS difference was 3 cm d^{-1} for Helheim and 5 cm d^{-1} for Kangerlussuaq. Black line indicates a 1:1 ratio.

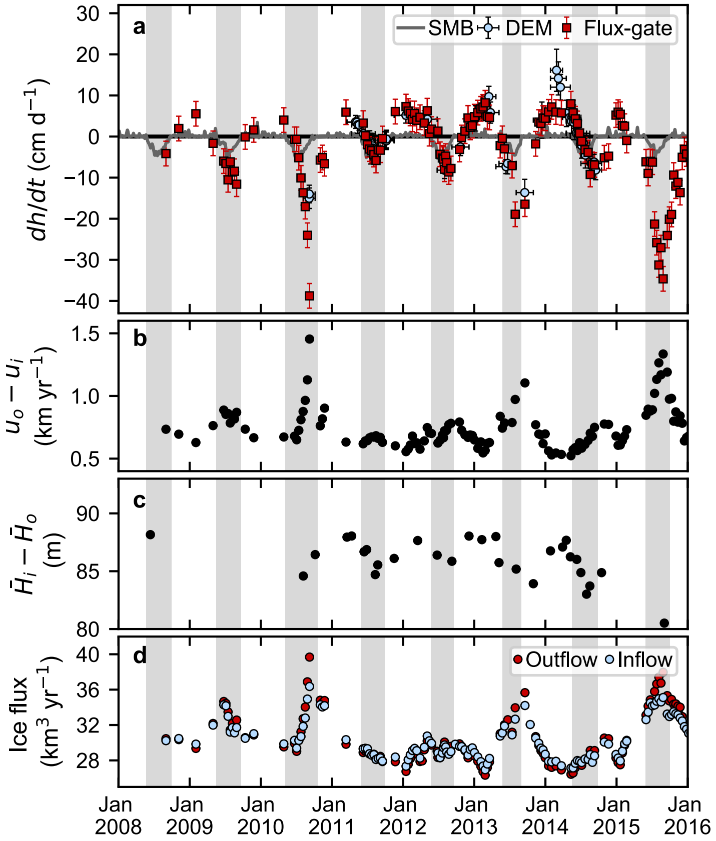

Figure A.3. (a) Surface-elevation change rates, *dh/dt*, at Helheim from the DEM and flux-gate methods for the hatched region in Figure 2.1a. The gray curve indicates the expected surface-elevation change rate due to surface mass balance processes from RACMO2.3. (b) Relative difference in the velocity between the outflow and inflow boundaries, (c) relative difference in the surface elevation between the inflow and outflow boundaries, and (d) ice flux through the inflow and outflow boundaries. Gray vertical bars indicate periods of surface runoff.

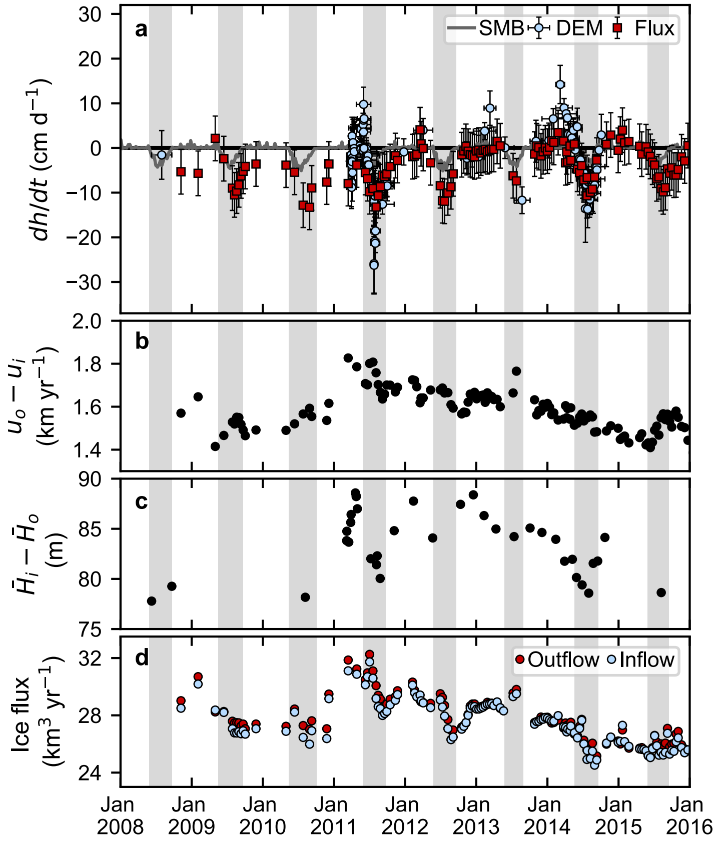

Figure A.4. Surface-elevation change rates at Kangerlussuaq for the hatched region in Figure 2.2b. Subpanels are the same as in Figure A.3.

APPENDIX B

This section is the supplement for Chapter 3, "Basal conditions for Helheim and Kangerlussuaq Glaciers, Southeast Greenland, from 2001 to 2016" authored by L. Kehrl, I. Joughin, B.E. Smith, and I. M. Howat.

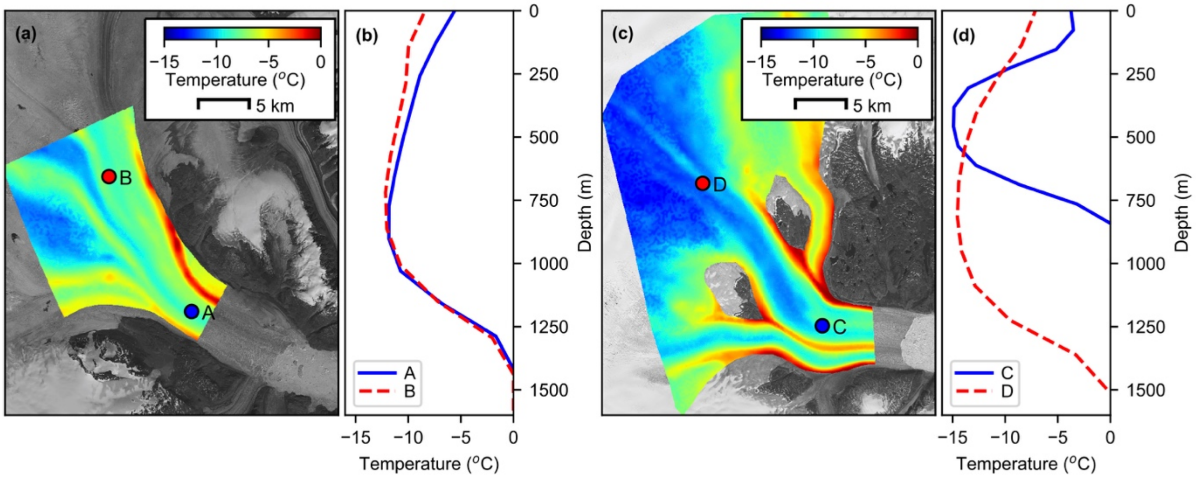

Figure B.1. Depth-averaged temperature at (a) KG and (c) HG. Temperature profiles at sample points A and B are shown in (b) and at sample points C and D in (d).

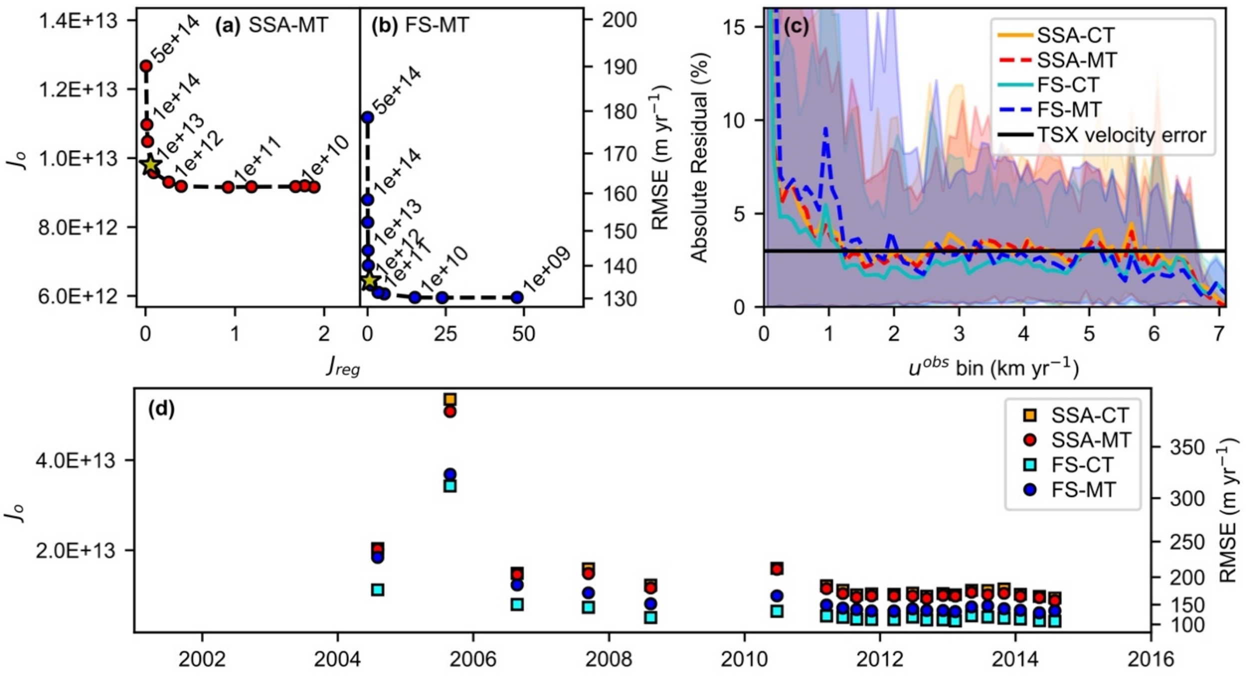

Figure B.2. Data-model misfit for HG. (a,b) L-curves show model norm J_{reg} versus data-model misfit J_o for different values of the regularization parameter λ for (a) SSA-MT and (b) FS-MT. Yellow stars indicate the chosen regularization parameter for SSA-MT and SSA-CT ($\lambda = 1e13$) and for FS-MT and FS-CT ($\lambda = 1e12$). (c) Mean absolute residual between modeled and observed velocities binned by velocity u^{obs} every 100 m yr^{-1} for SSA-CT (orange), SSA-MT (red), FS-CT (cyan), and FS-MT (blue). Shaded bars show the 90th percentile range. Mean absolute residuals are similar to the expected error for TSX velocity estimates (black line) for u^{obs} > 1 km yr^{-1}. Inversions in (a–c) are constrained by observations from 16 March 2012 (d) Data-model misfit J_o for all inversions from 2001 to 2016.

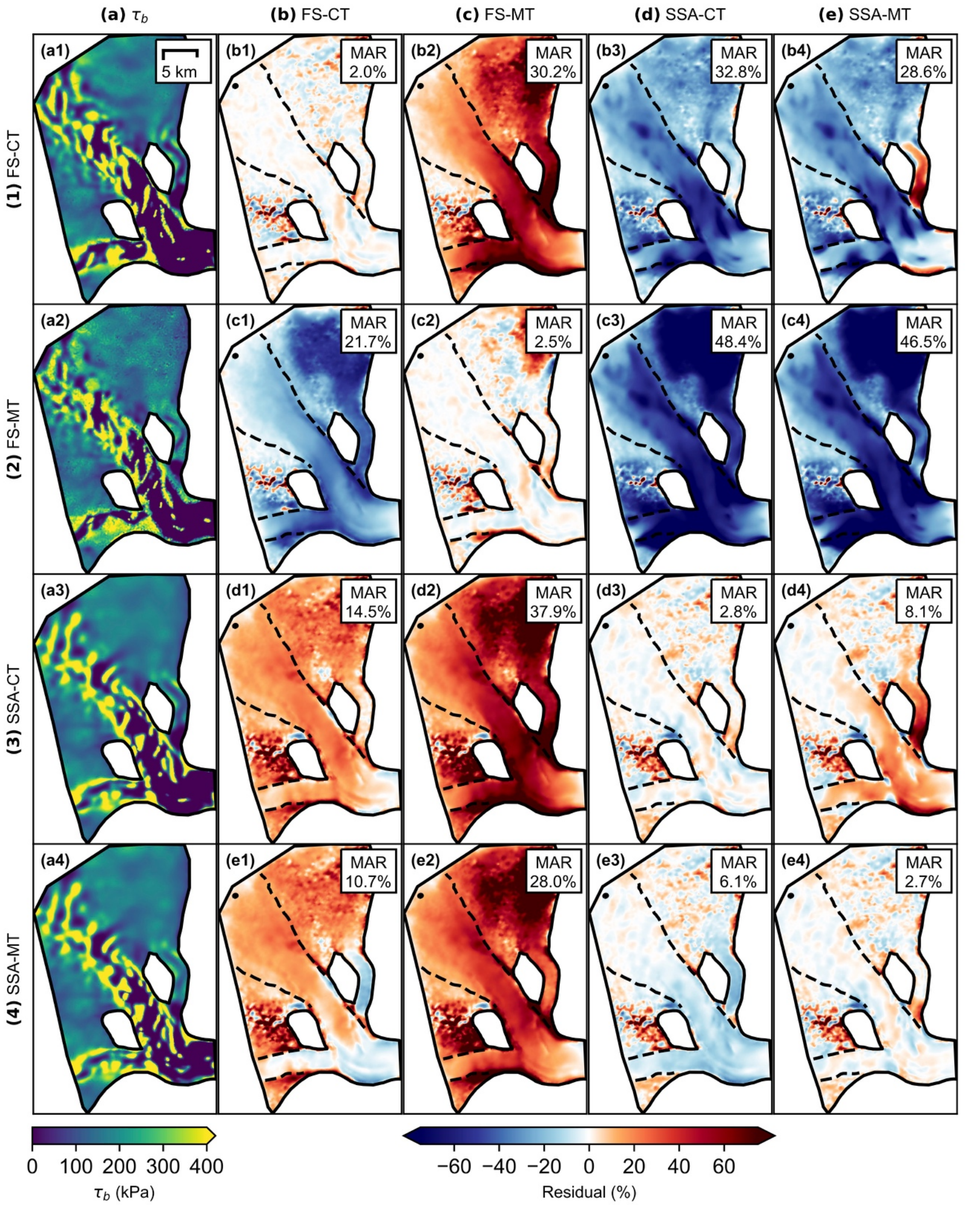

Figure B.3. (a) Inferred basal shear stress τ_b and (b-e) residual between modeled and measured velocities for HG for 16 March 2012. Rows use a single basal friction coefficient field inferred from (1) FS-CT, (2) FS-MT, (3) SSA-CT, and (4) SSA-MT. Columns (b-e) indicate the forward model used for each steady-state simulation: (b) FS-CT, (c) FS-MT, (d) SSA-CT, (e) SSA-MT.

For example, subpanel c1 shows a steady-state simulation using the FS-CT forward model with an inferred basal friction coefficient from FS-MT. The mean absolute residual (MAR) is calculated for the region where the observed velocity is greater than 1 km yr^{-1}, as indicated by the dashed curve. Low MAR values are expected for subpanels b1, c2, d3, and e4, which use the same forward model as the model used to infer the basal friction coefficient.

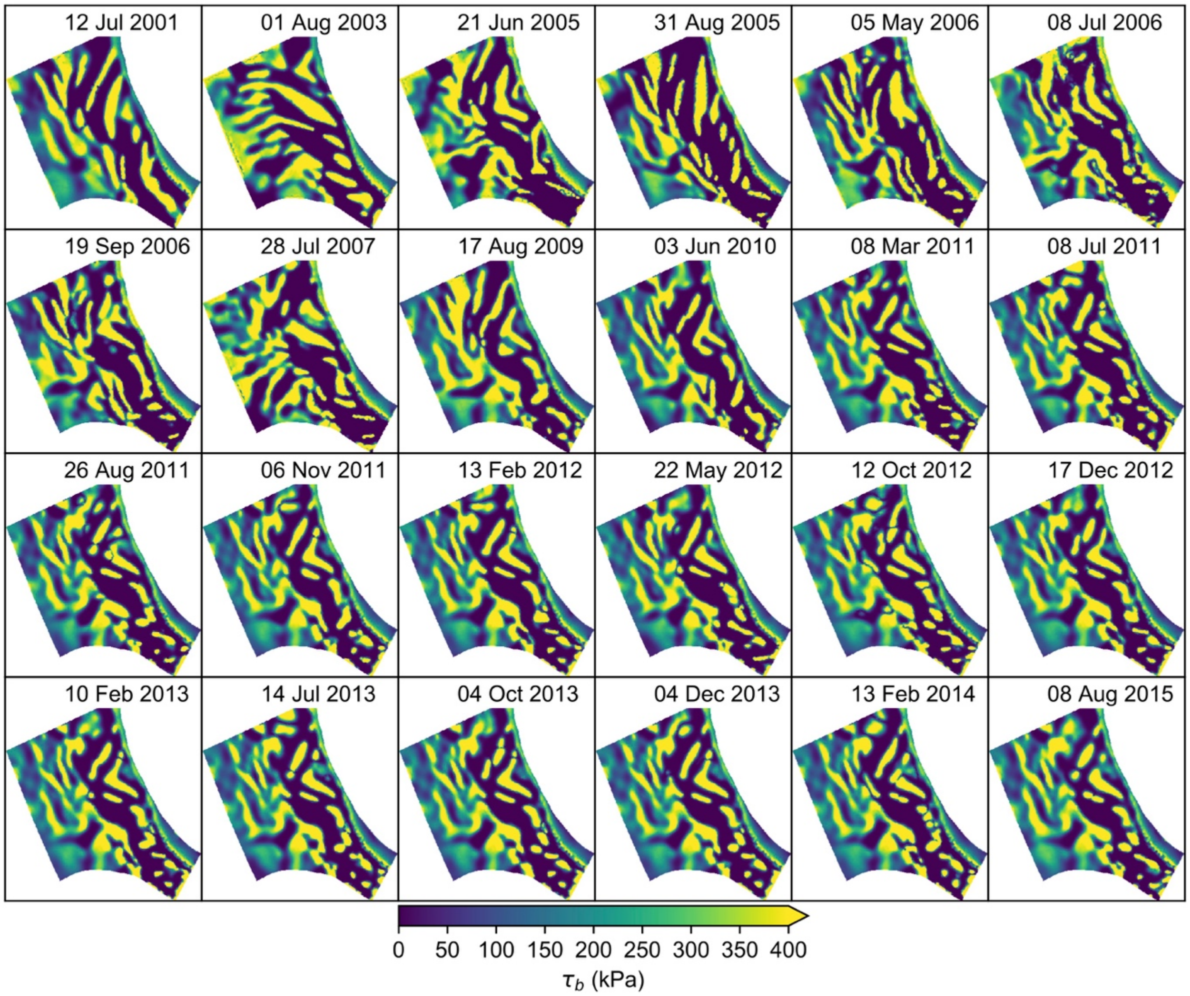

Figure B.4. Basal shear stress at KG for all snapshot inversions using FS-CT.

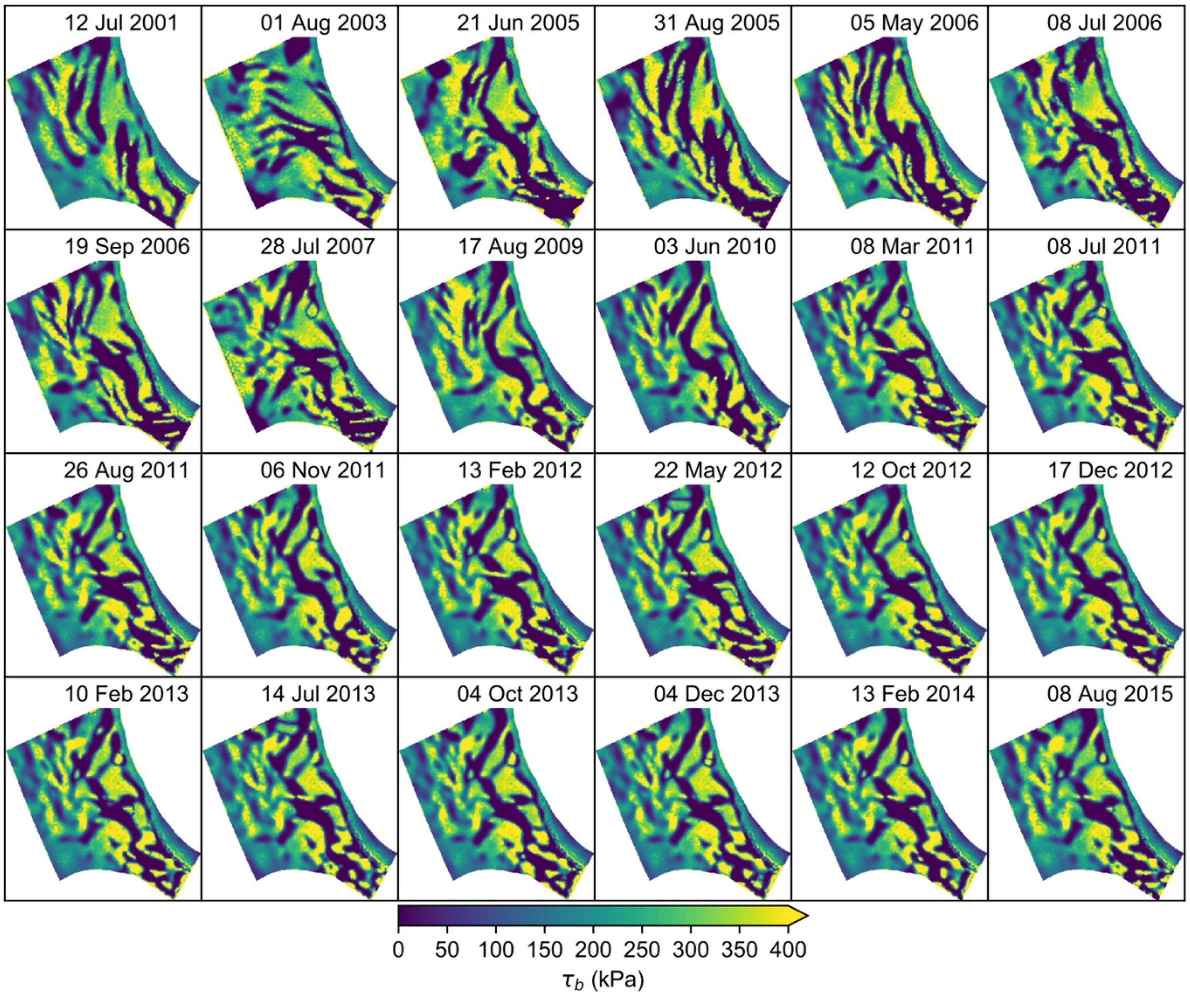

Figure B.5. Basal shear stress at KG for all snapshot inversions using FS-MT.

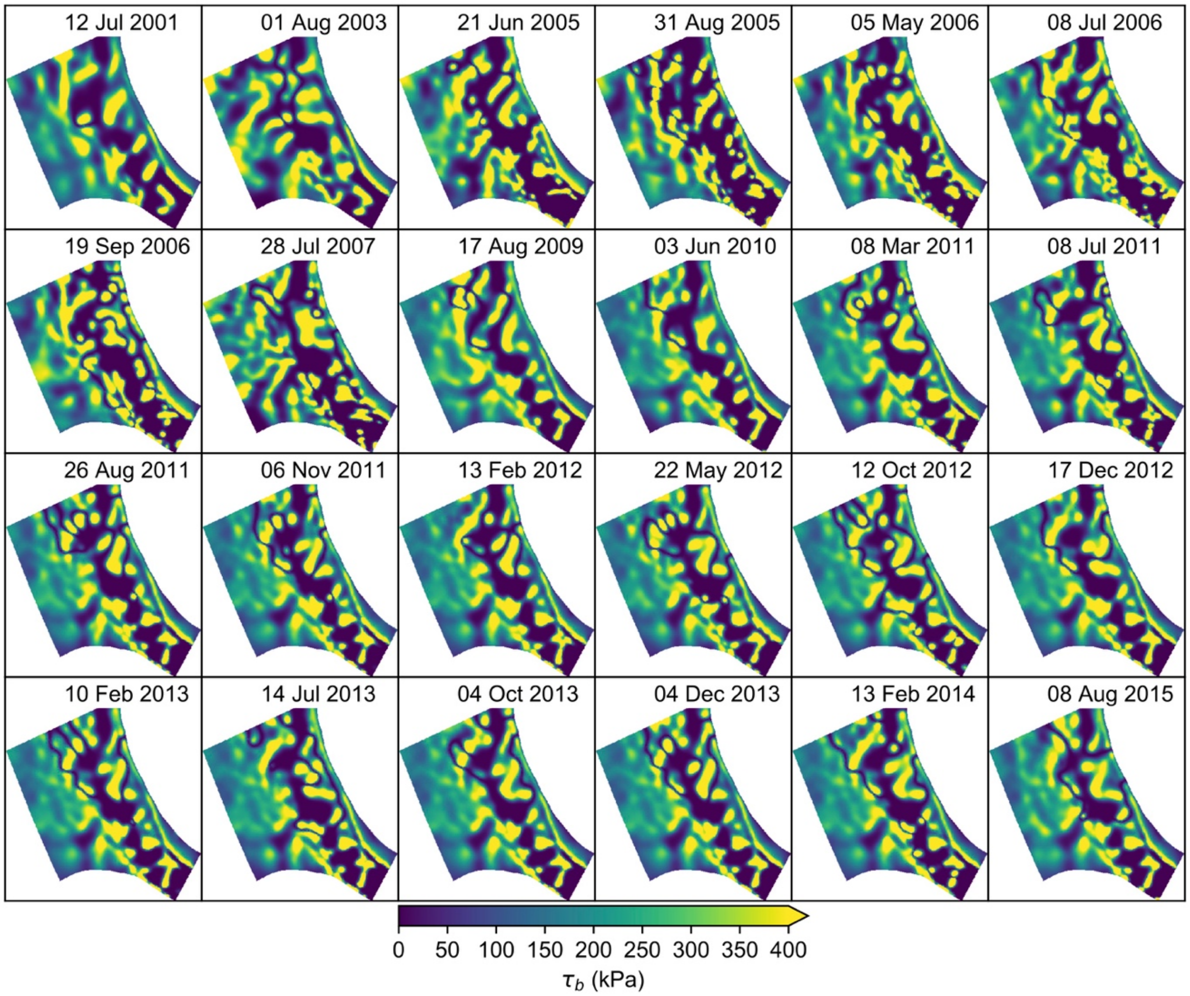

Figure B.6. Basal shear stress at KG for all snapshot inversions using SSA-CT.

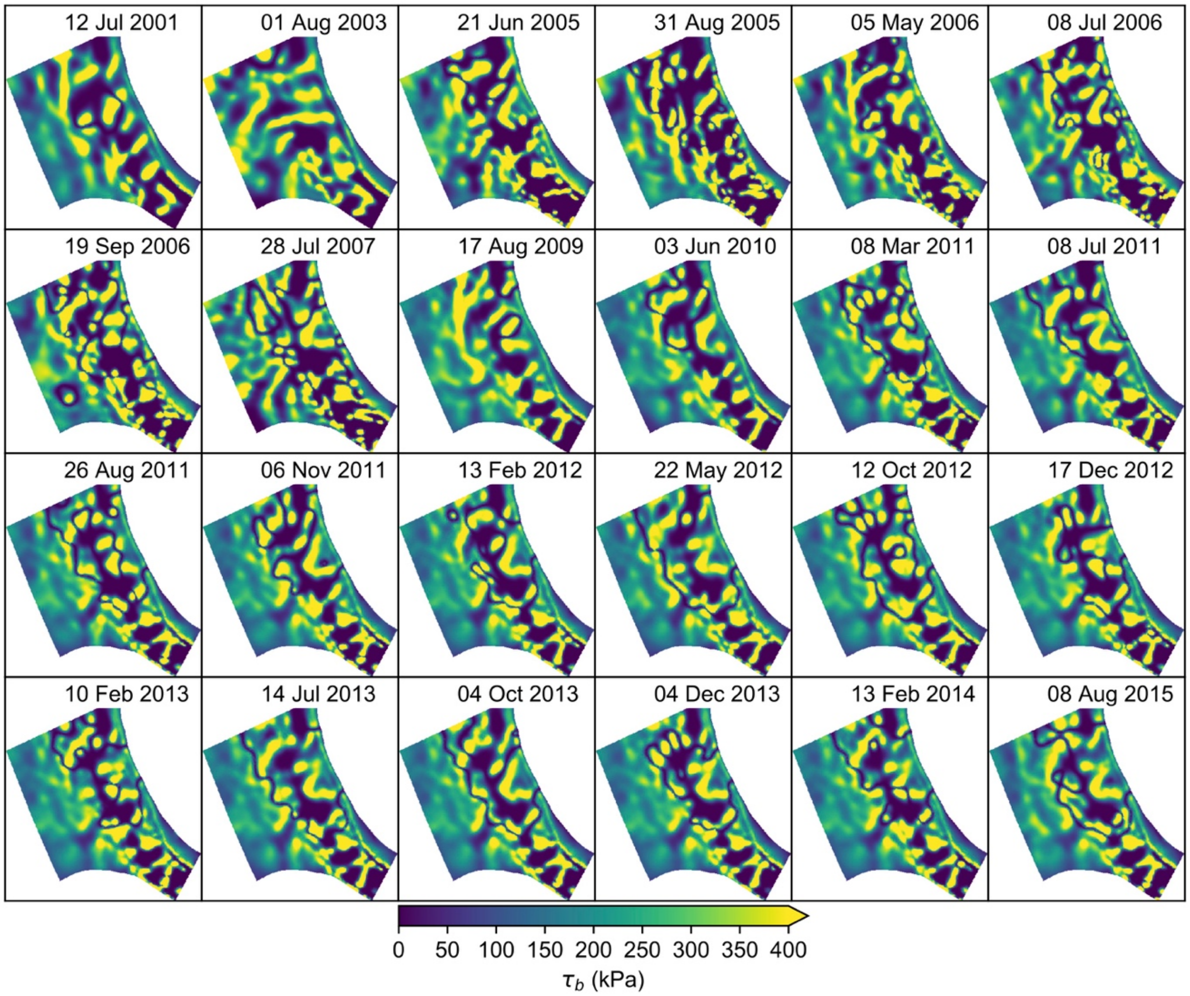

Figure B.7. Basal shear stress at KG for all snapshot inversions using SSA-MT.

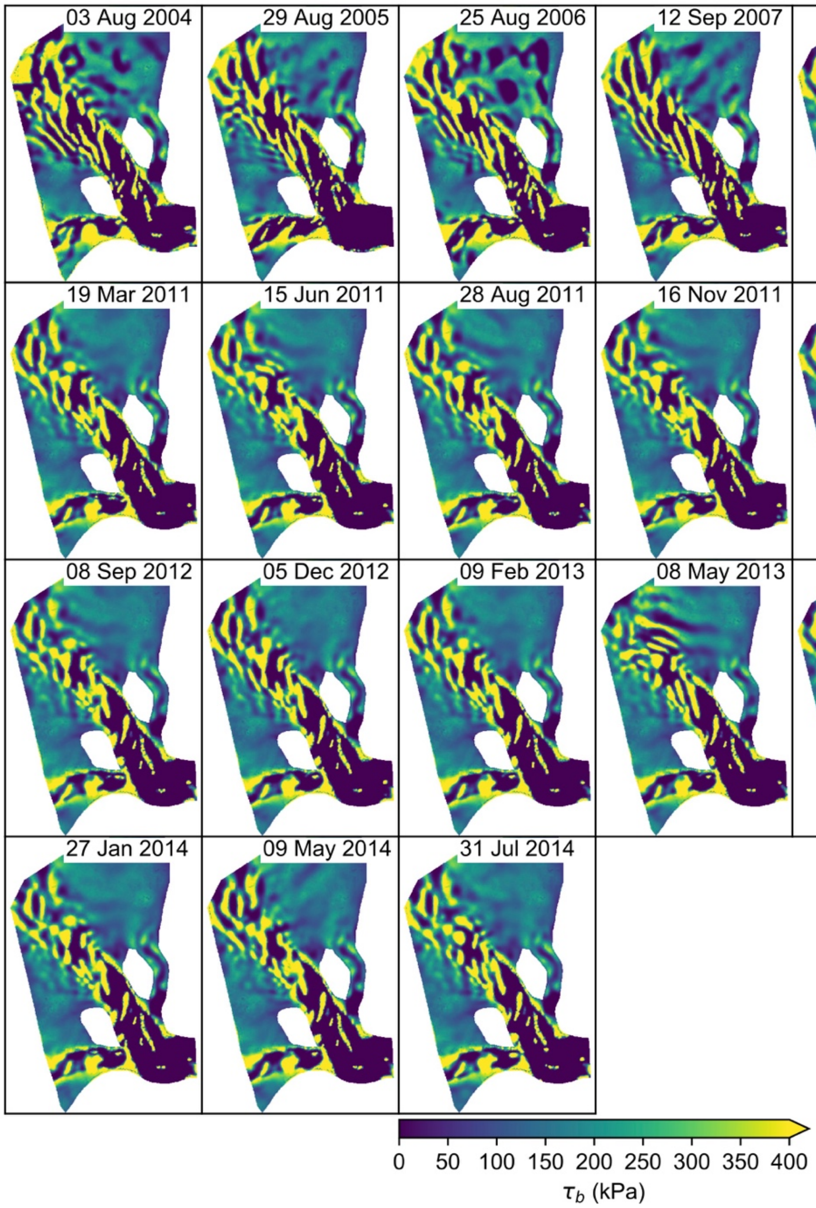

Figure B.8. Basal shear stress at HG for all snapshot inversions using FS-CT.

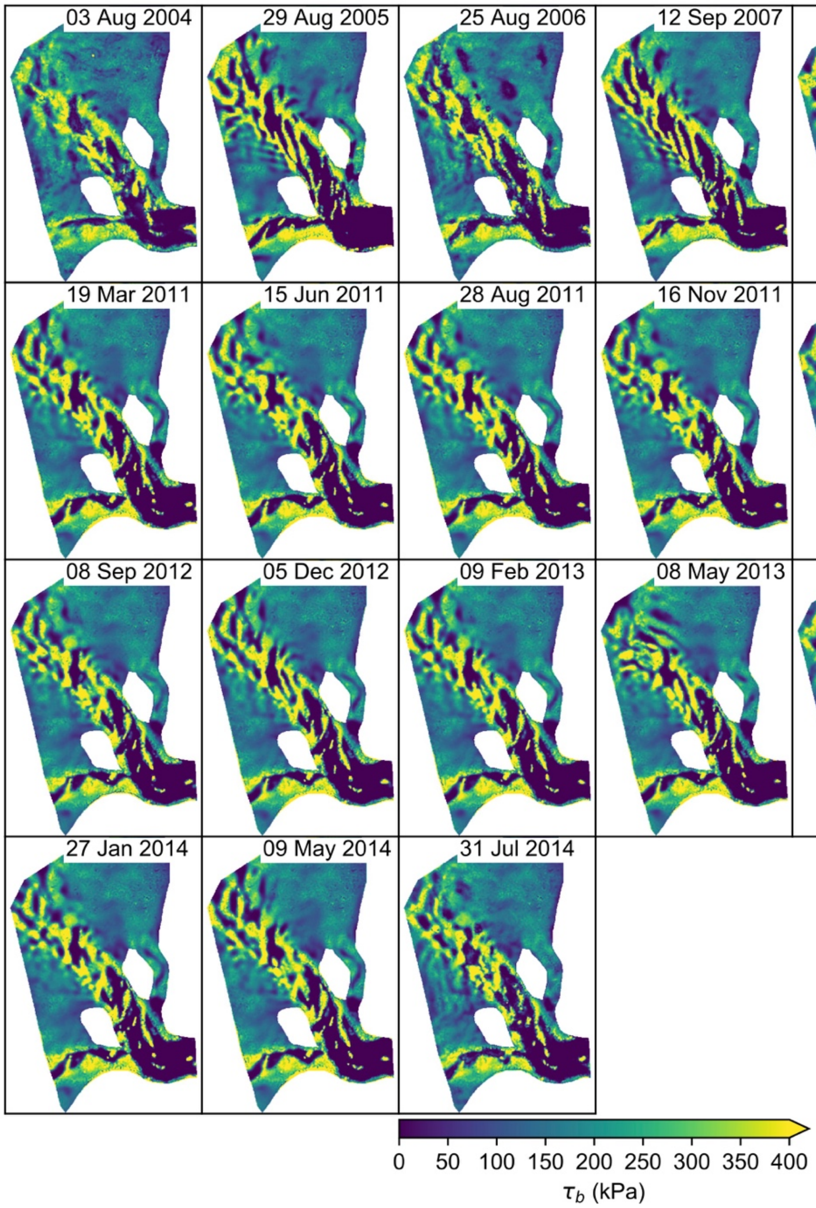

Figure B.9. Basal shear stress at HG for all snapshot inversions using FS-MT.

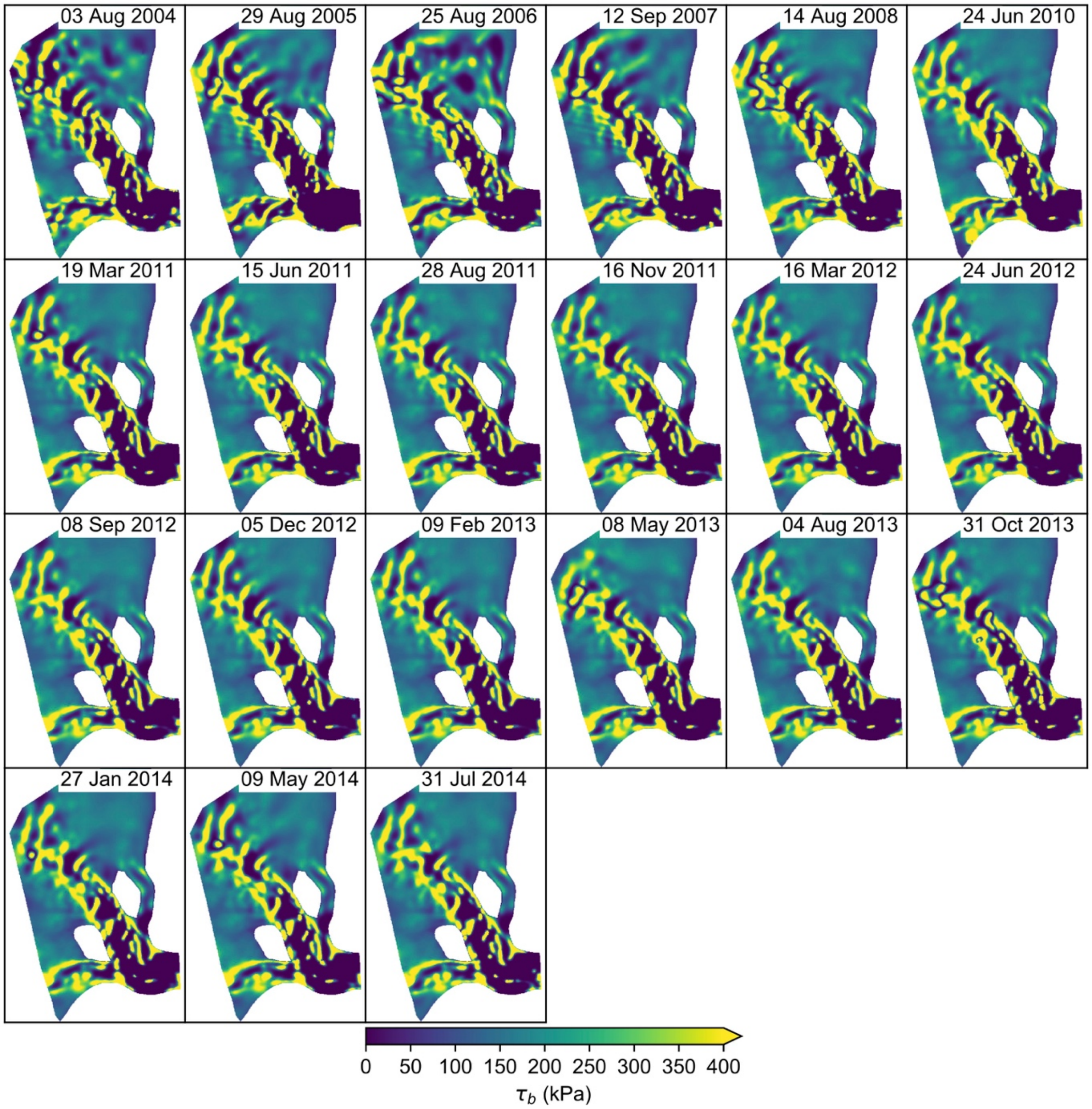

Figure B.10. Basal shear stress at HG for all snapshot inversions using SSA-CT.

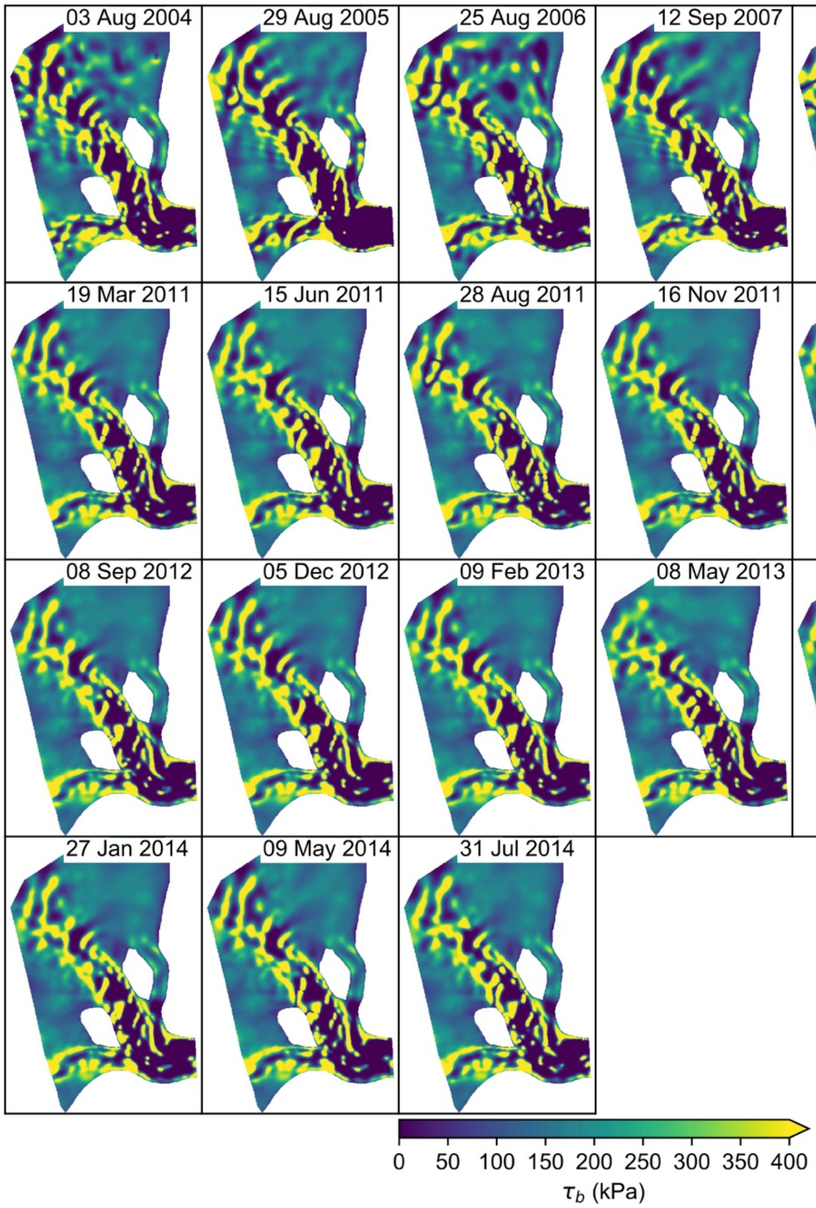

Figure B.11. Basal shear stress at HG for all snapshot inversions using SSA-MT.

Date	Surface elevation	Surface velocity
12 July 2001	ASTER20010712, ASTER20010703	HOWAT2001-07
1 Aug 2003	ASTER20030801, ASTER20030630	HOWAT2003-07, HOWAT2003-08
21 June 2005	ASTER20050621, ASTER20050616	HOWAT2005-06
31 Aug 2005	ASTER20050831, ASTER20050721	HOWAT2005-08
5 May 2006	ASTER20060505, ASTER20060428	HOWAT2006-04, HOWAT2006-05
8 July 2006	ASTER20060708, ASTER20060716	HOWAT2006-06, HOWAT2006-07
19 Sept 2006	ASTER20060919, ASTER20060903	HOWAT2006-09
28 July 2007	SPIRIT20070728	HOWAT2007-08, HOWAT2007-07
17 Aug 2009	ASTER20090817, ASTER20090815	TSX20090820, TSX20090809, TSX20090830
3 June 2010	ASTER20100603	TSX20100613
8 Mar 2011	WV20110308, WV20110311, WV 20110318	TSX20110315
8 July 2011	TDM20110708, WV20110708	TSX20110702, TSX20110719, TSX20110621
26 Aug 2011	WV20110826, WV20110824	TSX20110827, TSX20110816, TSX20110907
6 Nov 2011	TDM20111106	TSX20111111, TSX20111015
13 Feb 2012	TDM20120213	TSX20120207, TSX20120219
22 May 2012	TDM20120522	TSX20120511
12 Oct 2012	TDM20121012	TSX20121017, TSX20120925
17 Dec 2012	TDM20121217	TSX20121211, TSX20121223, TSX20121201
10 Feb 2013	TDM20130210	TSX20130204, TSX20130215, TSX20130124
14 July 2013	TDM20130714	TSX20130708, TSX20130725
4 Oct 2013	TDM20131004	TSX20131026
4 Dec 2013	TDM20131204	TSX20131128, TSX20131209, TSX20131117
13 Feb 2014	TDM20140213	TSX20140203, TSX20140225
8 Aug 2015	WV20150808, WV20150814, WV20150818	TSX20150806, TSX20150817, TSX20150726

Table B.1. Surface-elevation and -velocity data sources for KG. Surface-elevation measurements are from ASTER [*Howat et al.*, 2007], SPIRIT [*Korona et al.*, 2009], Worldview (WV), and TanDEM-X (TDM) [*Kehrl et al.*, 2017]. Surface-velocity measurements are derived from optical feature tracking of ASTER and Landsat images (HOWAT) [*Howat*, 2017] and from speckle tracking of TerraSAR-X and TanDEM-X radar images (TSX) [*Joughin et al.*, 2010a, 2016].

Date	Surface elevation	Surface velocity
8 Mar 2004	ASTER20040803, ASTER20040718, ASTER20040623	HOWAT2004-08, HOWAT2004-07
29 Aug 2005	ASTER20050829, ASTER20050712, ASTER20050619	HOWAT2005-09, HOWAT2005-07
25 Aug 2006	ASTER20060825, ASTER20060830	HOWAT2006-09, HOWAT2006-07
12 Sept 2007	SPIRIT20070912	HOWAT2007-08, HOWAT2007-09
14 Aug 2008	ASTER20080814, ASTER20080803	TSX20080901
24 June 2010	ASTER20100624, ASTER20100601	TSX20100622, TSX20100703
19 Mar 2011	WV20110319, WV20110615	TSX20110314
15 June 2011	TDM20110615	TSX20110609, TSX20110621
28 Aug 2011	WV20110828, WV20110615	TSX20110826, TSX20110905, TSX20110815
16 Nov 2011	TDM20111116	TSX20111122
16 Mar 2012	TDM20120316	TSX20120311, TSX20120327, TSX 20120228
25 June 2012	WV20120624, WV20120629, WV20120513	TSX20120624, TSX20120709
8 Sept 2012	TDM20120908	TSX20120903, TSX20120822, TSX20120924
5 Dec 2012	TDM20121205	TSX20121129, TSX20121210
9 Feb 2013	TDM20130209	TSX20130205, TSX20130215
8 May 2013	TDM20130508	TSX20130513
4 Aug 2013	TDM20130804	TSX20130730, TSX20130821
31 Oct 2013	TDM20131031	TSX20131111, TSX20131014
27 Jan 2014	TDM20140127	TSX20140202, TSX20140117
9 May 2014	WV20140509, WV20140611, WV20140418, TDM20130508	TSX20140512, TSX20140523, TSX20140419
31 July 2014	WV20140731, TDM20130804	TSX20140723, TSX20140807

Table B.2. Surface-elevation and -velocity data sources for HG. See Table B.1 for a description of abbreviations.

Region	Model	Correlation Coefficient	P-value
Lower KG	FS-CT	– 0.88	0.000
	FS-MT	– 0.81	0.000
	SSA-CT	– 0.83	0.000
	SSA-MT	– 0.80	0.000
Upper KG	FS-CT	+ 0.09	0.666
	FS-MT	– 0.16	0.452
	SSA-CT	+ 0.60	0.002
	SSA-MT	+ 0.60	0.002
Combined KG	FS-CT	– 0.35	0.093
	FS-MT	– 0.51	0.011
	SSA-CT	+ 0.36	0.083
	SSA-MT	+ 0.46	0.026

Table B.3. Pearson correlation coefficients and p-values for the relationship between the basal shear stress and basal velocity at KG for the lower glacier, upper glacier, and combined region of fast flow.

Region	Model	Correlation Coefficient	P-value
Lower HG	FS-CT	– 0.87	0.000
	FS-MT	– 0.78	0.000
	SSA-CT	– 0.27	0.245
	SSA-MT	– 0.27	0.232
Upper HG	FS-CT	– 0.06	0.804
	FS-MT	+ 0.54	0.011
	SSA-CT	+ 0.80	0.000
	SSA-MT	+ 0.82	0.000
Combined HG	FS-CT	– 0.66	0.001
	FS-MT	– 0.04	0.860
	SSA-CT	+ 0.58	0.006
	SSA-MT	+ 0.62	0.003

Table B.4. Pearson correlation coefficients and p-values for the relationship between the basal shear stress and basal velocity at HG for the lower glacier, upper glacier, and combined region of fast flow.

APPENDIX C

This section is the supplement for Chapter 4, "Evaluating the duration and continuity of potential climate records from the Allan Hills Blue Ice Area, East Antarctica" authored by L. Kehrl, H. Conway, N. Holschuh, S. Campbell, A.V. Kurbatov, and N.E. Spaulding, as it appears in *Geophysical Research Letters* 2018.

C.1 ***Uncertainty estimates for radar-detected layer ages***

Several sources of error contribute to uncertainties in the inferred layer ages. First, *Spaulding et al.* [2013] developed age scales for the S27 horizontal and vertical ice cores by comparing stable water isotope records from the cores to the EPICA Dome C record *[EPICA Community Members*, 2004]; timescales developed from stable water isotope analysis typically have uncertainties of 6 ka [*Bender et al.*, 1994; *Petit et al.*, 1999]. The S27 age scale is then linearly interpolated to assign ages to the englacial layers, which likely leads to an underestimation of layer ages [*Fudge et al.*, 2014]. To quantify errors due to the interpolation, assumed electromagnetic wave speeds, and depth resolution of the radar system (1/4 wavelength or ~6 m) [*Cavitte et al.*, 2016], we extrapolate the depth-age scale from Radar Track 4 along different across-flow tracks (Radar Tracks A-F) to determine multiple ages for each picked layer in the along-flow tracks (Radar Tracks 1-3). The average age difference for the 43 picked layers with multiple ages is 2 ka, with a maximum difference of 6 ka (Figure C.1). We calculate the total age uncertainty as the root-mean-square combination of the uncertainty from the S27 age scale and from the radar reflections, providing a cumulative error estimate of 7 ka.

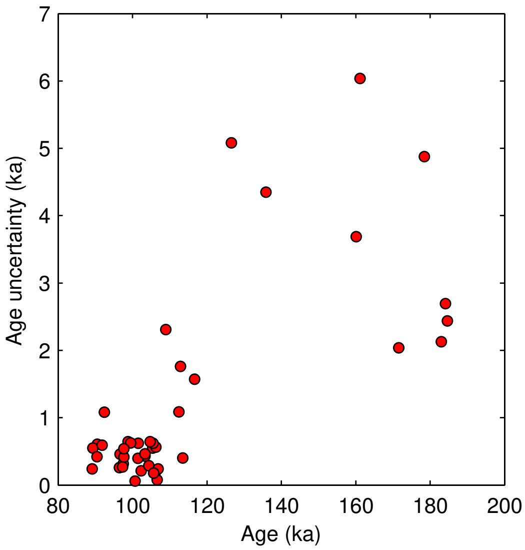

Figure C.1. Average age difference for the 43 picked layers with multiple ages. Average age difference increases with layer age.

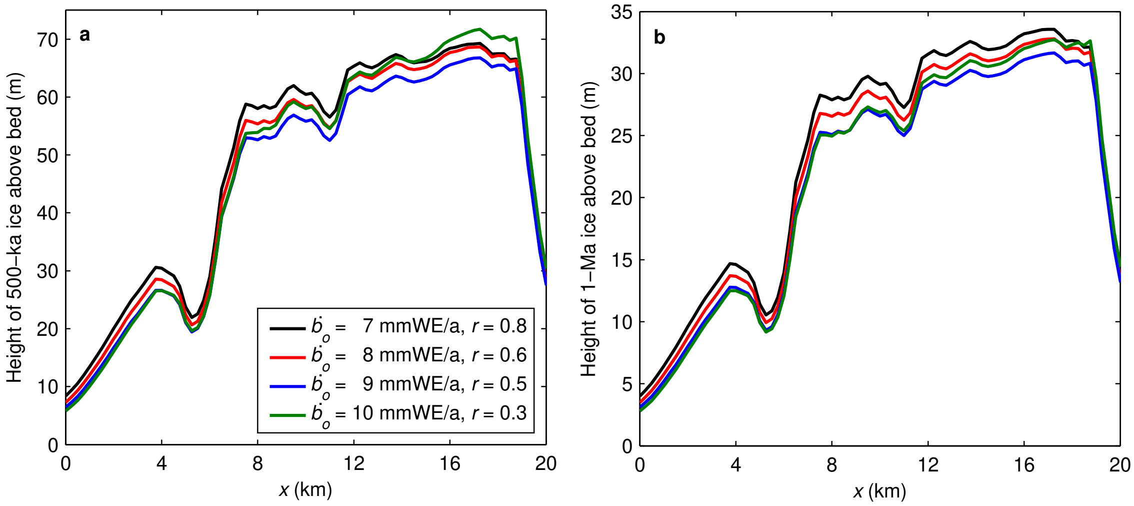

Figure C.2. Height of (a) 500-ka and (b) 1-Ma ice above the bed along the flowline. In the basin from $x = 7$ to $x = 19$ km, the best-fit models indicate that 500-ka ice should be 55-70 m above the bed and 1-Ma ice should be 25-35 m above the bed.

VITA

Laura Kehrl received her A.B. in Earth Sciences from Dartmouth College (2010) and her M.Sc. from Victoria University of Wellington (2012). While at Dartmouth, she investigated sedimentation processes at the termini of two tidewater glaciers in Svalbard. Her master's thesis investigated the response of Franz Josef Glacier, New Zealand, to rain and diurnal melt events. She worked as a research assistant at Dartmouth College from 2010-2011 and from 2012-2013. Her current research combines geophysical observations and numerical models to better understand the response of glaciers to past, present, and future climate change.